

Functionalization of Calcium Phosphate Nanoparticles with Organic Phosphates

Dissertation

zur Erlangung des akademischen Grades

Doktor der Naturwissenschaften

– Dr. rer. nat. –

vorgelegt von

Kathirvel Ganesan

aus Tamil Nadu/Indien

Institut für Anorganische Chemie
der Universität Duisburg-Essen,
Essen, Deutschland.

2008

**Dedicated to my family members,
and teachers.**

Die vorliegende Arbeit wurde im Zeitraum von Januar 2005 bis April 2008 im Arbeitskreis von Prof. Dr. Matthias Epple am Institut für Anorganische Chemie der Universität Duisburg-Essen durchgeführt.

Gutachter: Prof. Dr. M. Epple
Prof. Dr. G. Haberhauer

Vorsitzender: Prof. Dr. E. Spohr

Tag der mündlichen Prüfung: 30. May 2008

List of contents

1. Introduction	7
2. Theoretical background	9
2.1. Biomineralization	9
2.2. Calcium-based biominerals	11
2.2.1. Calcium carbonate	12
2.2.2. Calcium phosphate	13
2.2.3. Calcium sulphate	14
2.2.4. Calcium oxalate	14
2.2.5. Calcium fluoride	15
2.3. Conditions for the precipitation of calcium phosphate crystallization	16
2.3.1. Nucleation	16
2.3.2. Thermodynamic and kinetic crystal growth	20
2.3.3. pH	22
2.3.4. Solubility product	23
2.3.5. Temperature	23
2.3.6. Presence of ions or additives	23
2.4. Hollow inorganic nanoparticles	25
2.4.1. Principles and methods of the synthesis of hollow inorganic particles	25
2.5. Colloids	31
2.5.1. Functionalization of calcium phosphate nanoparticles	31
2.6. Organic phosphates as functionalizing agents	34
2.6.1. Porphyrin	34
2.6.2. Phytic acid	38
2.6.4. Amino acids with phosphate functional groups	40
2.6.1. Surfactants	44
3. Results and discussion	46
3.1. Synthesis and characterization of <i>p</i> -TPPP-functionalized calcium phosphate nanoparticles	46
3.1.1. Synthesis of 5,10,15,20-tetrakis(4-phosphonooxyphenyl)porphine (<i>p</i> -TPPP)	47
3.1.2. Preparation of stable colloids by optimizing the concentration of <i>p</i> -TPPP	49
3.1.3. Analyzing the effective functionalization of <i>p</i> -TPPP on the calcium phosphate surface	50
3.1.4. Experiments with NIH 3T3 fibroblast cell culture	58
3.1.5. Conclusions	62

3.2. Synthesis and characterization of calcium phytate nanoparticles from calcium phosphate nanoparticles-----	63
3.2.1. Optimizing the concentration of phytic acid to prepare the stable colloids of calcium phytate nanoparticles -----	64
3.2.2. Conclusion -----	73
3.3. Synthesis and characterization of hollow calcium phosphate nanoparticles-----	74
3.3.1. Synthesis of <i>O</i> -phospho-L-tyrosine (TyrP). -----	75
3.3.2. Influence of the concentration of TyrP on the morphology of the calcium phosphate nanoparticles -----	75
3.3.3. Conclusion -----	85
3.4. Functionalization of calcium phosphate nanoparticles with alkyl phosphates -----	87
3.4.1. Represented alkyl phosphates -----	87
3.4.2. Synthesis of alkyl phosphates -----	88
3.4.3. Optimizing the concentrations of alkyl phosphates to functionalize the calcium phosphate surface -----	89
3.4.4. Comparison of the sodium salt of TDP with other surfactants or alkyl phosphates in functionalizing the calcium phosphate surface ----	93
3.4.5. Conclusions -----	100
4. Materials and methods -----	102
4.1. Experimental procedures-----	102
4.1.1 Used chemicals-----	102
4.1.2. Preparation of N,N-diethylphosphoramidous dichloride -----	103
4.1.3. Preparation of di-tert-butyl-N,N-diethylphosphoramidite -----	103
4.1.4. Synthesis of 5,10,15,20-tetrakis(4-phosphonoxyphenyl)porphine (<i>p</i> -TPPP)-----	104
4.1.4.1. Phosphorylation of <i>p</i> -THPP -----	104
4.1.4.2. Deprotection -----	105
4.1.5. Preparation of <i>O</i> -phospho-L-tyrosine -----	106
4.1.6. Dodecyl phosphate (DDP)-----	107
4.1.7. Tetradecyl phosphate (TDP)-----	108
4.1.8. Octadecyl phosphate (ODP)-----	109
4.1.9. <i>p</i> -dodecyloxyphenyl phosphate (DDOPhP) -----	109
4.1.9.1. <i>p</i> -dodecyloxyphenol -----	109
4.1.9.2. <i>p</i> -dodecyloxyphenyl phosphate -----	110
4.1.10. <i>p</i> -dodecyloxybiphenyl- <i>p'</i> -phosphate (DDOBPhP) -----	111
4.1.10.1. <i>p</i> -dodecyloxy- <i>p'</i> -hydroxybiphenyl -----	111
4.1.10.2. <i>p</i> -dodecyloxybiphenyl- <i>p'</i> -phosphate -----	111

4.1.11. Preparation of organic phosphate-functionalized calcium phosphate nanoparticles: General procedure-----	113
4.1.12. Cell culture experiments-----	114
4.2. Instrumental techniques-----	116
4.2.1. Nuclear magnetic resonance (NMR) -----	116
4.2.2 Dynamic light scattering (DLS) -----	117
4.2.3 Zeta potential measurements (ZP)-----	118
4.2.4 Infrared spectroscopy (IR)-----	118
4.2.5 X-ray diffractometry (XRD) -----	120
4.2.6 Scanning electron microscopy (SEM) -----	120
4.2.7. UV-vis spectroscopy-----	121
4.2.8. Fluorescence spectroscopy-----	123
4.2.9. Electron spray ionization mass spectrometry-----	124
5. Summary-----	125
6. Reference -----	128
7. Appendix -----	136
7.1. List of Abbreviations -----	136
7.2. Publications-----	137
7.3. Presentations and posters -----	137
7.4. Curriculum vitae -----	138
7.5. Acknowledgement-----	139
7.6. Erklärung-----	140

1. Introduction

Calcium phosphate nanoparticles have gained increasing interest in the last years due to their high biocompatibility which is due to the fact that calcium phosphate constitutes the inorganic mineral of mammalian bone and teeth.^{[1-}

^{6]} They are widely used in medicine for biomaterials (e.g., bone regeneration, tooth substitutes, etc.) and drug delivery vehicles.^[2, 7, 8]

Calcium phosphate nanoparticles can be used as fluorescing probes after doping with lanthanides.^[9-13] Eu³⁺-doped fluorescing calcium phosphate nanoparticles with high internal crystallinity and with a shell of DNA were used to track the nanoparticles in cell transfection studies.^[13] However, the fluorescence efficiency of lanthanide-doped calcium phosphates is limited by the necessity for a crystalline environment of the lanthanide in order to give a good fluorescence. This is difficult to achieve for calcium phosphate nanoparticles.^[13] Biocompatible fluorescing nanoparticles have gained much interest in biomedicine.

Calcium phosphate nanoparticles can act as drug-carriers, e.g. for nucleic acids^[8] or for antitumor drugs.^[14, 15] For instance, a successful cell transfection has been accomplished with DNA- and siRNA-coated calcium phosphate nanoparticles.^[16-20] Nucleic acid-loaded calcium phosphate nanoparticles show an effective transfection where the calcium phosphate nanoparticles act as a carrier. Nucleic acids show a good interaction with a calcium phosphate surface and are able to stabilize calcium phosphate in the form of a colloid.^[8, 18, 20-22] However, the nature of the interface between DNA and calcium phosphate remains largely unknown, although it can be assumed that there is a specific interaction between the phosphate groups of DNA and the calcium phosphate surface. To understand the interaction of

calcium phosphate with biological macromolecules like DNA, an organic phosphate-functionalized calcium phosphate surface was used as a model system in the present study. It is also of interest in biological and material sciences to clarify the interaction between calcium phosphate and organic phosphates, which is important in biological mineralization and calcification. Because a variety of phospholipids and phosphoproteins are present in calcifying tissues, body fluids and cell matrix vesicles which play a crucial role in the biological mineralization (inhibiting, nucleating or enhancing the crystal growth of calcium based biominerals).^[23-26] The aim of my Ph.D work was to functionalize calcium phosphate nanoparticles with organic phosphates.

Organic phosphates have high chemical affinity to bind with calcium phosphate surface. Taking this in to consideration, the functionalization of calcium phosphate nanoparticles is mainly done using organic phosphates. Organic phosphates used in the present study are represented here.

Porphyrin : 5,10,15,20-tetrakis(4-phosphonooxyphenyl)porphine

Phytic acid : *myo*-inositol-1,2,3,4,5,6-hexakisphosphate

Phosphoamino acid : *O*-phospho-L-tyrosine

Surfactants : dodecyl phosphate, tetradecyl phosphate, octadecyl phosphate, *p*-dodecyloxyphenyl phosphate and *p*-dodecyloxybiphenyl phosphate

2. Theoretical background

2.1. Biomineralization

The controlled formation of inorganic minerals by living organisms in the form of skeleton, shells, teeth, etc. is called biomineralization. This yields amorphous and crystalline biogenic materials that often exhibit remarkable morphological and mechanical properties. The major metal ions deposited in unicellular and multicellular organisms are the alkaline earth divalent cations (Mg, Ca, Sr, Ba), the transition metal, Fe, and the semi metal, Si. These usually form solid phases with the anions carbonate, oxalate, phosphate, sulfate and hydroxide/oxide. Less common are metals such as Mn, Au, Ag, Pt, Cu, Zn, Cd, and Pb which are deposited in bacteria, often as metal sulfides.^[27]

The biomineralization processes mainly takes place in a controlled reaction environment and furthermore the biomineral phases have properties such as shape, size, crystallinity, isotopic, and trace element compositions unlike its inorganically formed mineral phases. Figure 1 illustrates the comparison of a single calcite crystal formed by an echinoderm and a synthetic single crystals of calcite.^[28] Echinoderms live in marine environment and form mineralized hard parts (skeleton, spines, spicules, ossicles and teeth) containing mostly magnesium-bearing calcite.^[6] These mineralized hard parts have the stereom structure (spongy or fenestrate) and a complex system of interconnecting cavities of mineralized calcite (Fig. 1a). The fracture surfaces of echinoderm calcite are smooth and glassy. Whereas the synthetically prepared single crystals of calcite have a rhombohedral shape (Fig. 1b). Much of the research work in biomineralization is focused at understanding the control processes that organisms have worked out.

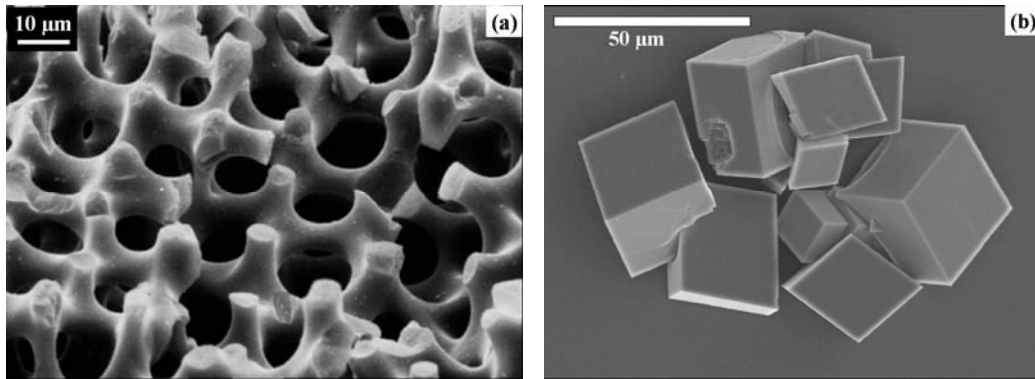


Figure 1: Comparison of SEM pictures of calcite single crystals: (a) stereomicro space and the highly curved surfaces of echinoderm and (b) synthetically prepared rhombohedral forms. The figures were adapted from reference^[28]

Biom mineralization processes are divided into two fundamentally different groups based upon their degree of biological control. The two groups are “biologically induced” and “biologically controlled” mineralization. Sometimes the undesirable metabolic end-products or ions are released by organisms through passive diffusion or active pumping or secretion. These byproducts combine with other ions in the external medium and induce mineral formation to precipitate. The type of mineral formed by this method is dependent on the environmental conditions in which the organism lives. The same organism in different environments can form different minerals. Mineral formation occurs as a result of interactions between biological activity and the aqueous environment in which organisms live is termed “biologically induced” mineralization. In “biologically controlled” mineralization, the organism uses cellular activities to direct the nucleation, growth and final location of the mineral that is deposited.^[28]

2.2. Calcium-based biominerals

Calcium is an alkaline earth metal belonging to Group II of the periodic table. It is a divalent cation with an atomic weight of 40 and shows a single oxidation state of +2. It is an essential element of all cells and organisms.

Table 1: The names and chemical compositions of calcium-based minerals produced by biologically-induced and controlled mineralization process.^[6]

Mineral	Formula
<u>Calcium carbonate:</u>	
Calcite	CaCO_3
Aragonite	CaCO_3
Vaterite	CaCO_3
Calcium carbonate monohydrate	$\text{CaCO}_3 \cdot \text{H}_2\text{O}$
Calcium carbonate hexahydrate	$\text{CaCO}_3 \cdot 6\text{H}_2\text{O}$
Amorphous calcium carbonate	$\text{CaCO}_3 \cdot n\text{H}_2\text{O}$
Protodolomite	$\text{CaMg}(\text{CO}_3)_2$
<u>Calcium phosphate:</u>	
Hydroxyapatite	$\text{Ca}_{10}(\text{PO}_4)_6(\text{OH})_2$
Fluoroapatite (francolite)	$\text{Ca}_{10}(\text{PO}_4)_6\text{F}_2$
Carbonated hydroxyapatite (dahllite)	$\text{Ca}_5(\text{PO}_4, \text{CO}_3)_3(\text{OH})$
Whitlockite	$\text{Ca}_{18}\text{H}_2(\text{Mg, Fe(II)})_2(\text{PO}_4)_{14}$
Octacalcium phosphate	$\text{Ca}_8\text{H}_2(\text{PO}_4)_6 \cdot 5\text{H}_2\text{O}$
β -Tricalcium phosphate	$\text{Ca}_3(\text{PO}_4)_2$
Brushite	$\text{CaHPO}_4 \cdot 2\text{H}_2\text{O}$
Amorphous calcium phosphate	$\text{Ca}_x(\text{PO}_4)_y \cdot n\text{H}_2\text{O}$
<u>Calcium oxalate:</u>	
Whewellite	$\text{CaC}_2\text{O}_4 \cdot \text{H}_2\text{O}$
Weddellite	$\text{CaC}_2\text{O}_4 \cdot 2\text{H}_2\text{O}$
<u>Calcium sulfate:</u>	
Gypsum	$\text{CaSO}_4 \cdot 2\text{H}_2\text{O}$
Bassanite	$\text{CaSO}_4 \cdot 0.5\text{H}_2\text{O}$
<u>Calcium fluoride:</u>	
Fluorite	CaF_2
<u>Organic crystals:</u>	
Earlandite	$\text{Ca}_3(\text{C}_6\text{H}_5\text{O}_2)_2 \cdot 4 \text{H}_2\text{O}$
Calcium tartrate	$\text{C}_4\text{H}_4\text{CaO}_6$
Calcium maleate	$\text{C}_4\text{H}_4\text{CaO}_5$

About half of all biominerals consists of poorly water-soluble calcium-rich compounds because calcium fulfills many fundamental functions in the cellular metabolism.^[6, 49-51] A wide range of calcium-based biominerals is shown in Table 1.

2.2.1. Calcium carbonate

The calcium carbonate minerals are the most abundant biogenic minerals, both in terms of the quantities produced and their widespread distribution among many different biological groups.^[6] Calcium carbonate exists in a variety of polymorphic phases shown in table 1, of which calcite, aragonite and vaterite are the anhydrous crystalline polymorphs. They have typical morphologies: calcite – rhombohedral, aragonite – needles, and vaterite – polycrystalline spheres. Calcite and aragonite are the two most common polymorphs found in biological and geological samples and thermodynamically stable phases.^[1, 29] They are the basic minerals used to build the shells. For example, the layered structure of the abalone shell is composed of alternating sheets of crystalline calcite and aragonite intertwined with organic binders.^[30] The shell gains strength and limits crack propagation because it is an organic-inorganic composite composed of two polymorphs. The grinding teeth of the sea urchin are composed of calcite but hardened with small amounts of magnesium.^[31] Calcite and aragonite are also used as gravity sensors in land and sea animals.^[1] Magnesium ions are often incorporated and many biological calcites contain up to 30% of Mg^{2+} .^[29] Vaterite is a metastable polymorph with respect to calcite and aragonite and not commonly formed by organisms.^[32-34] Calcium carbonate monohydrate and calcium carbonate hexahydrate (ikaite) are two hydrated

crystalline pseudopolymorphs. Calcium carbonate monohydrate is rarely found in biology.^[29, 35] The hexahydrate phase is found naturally only in sea water.^[29, 36] Amorphous calcium carbonate is intrinsically unstable thermodynamically and kinetically at physiological condition.^[6] It is found in biology,^[37] e.g. the cystoliths in leaves of certain plants,^[38, 39] exoskeletons of crustaceans,^[6] and ascidians.^[40]

2.2.2. Calcium phosphate

Calcium phosphates are very important inorganic minerals of biological hard tissues. The most abundantly produced phosphate mineral is carbonated hydroxyapatite, also called dahllite, closely associated with bone and teeth.^[6] Dentin and cementum in the tooth and the various forms of bone^[41] contain approximately 70 wt% apatite with 20% collagenous matrix and 10% water. Unlike the other hard tissues, the internal structure of enamel which contains no cells or pores, consists of about 95 wt% hydroxyapatite mineral.^[42] Enamel also differs in the way it is associated with the proteins enamelin and amelogenin rather than collagen. While these biomaterials have broad similarities, they differ in important details including their minor elements, water composition, and the degree of crystallinity.^[42] The biological apatite is known to be nanocrystalline and is formed biologically under mild conditions (ambient pressure, near room temperature).^[2] Pure hydroxyapatite never occurs in biological systems.^[2] However, because of the chemical similarities to bone and teeth mineral, hydroxyapatite is widely used as a coating for orthopedic (e.g. hip-joint prosthesis) and dental implants.^[43, 44] Amorphous calcium phosphate is often encountered as a transient phase during the formation of calcium phosphates in aqueous

systems. Amorphous calcium phosphate and octacalcium phosphate are believed to be precursors to hydroxyapatite.^[45-47]

2.2.3. Calcium sulphate

Calcium sulphate is a very important geological mineral. It is rarely found as a product of biomineralization^[6, 48, 49], which may be due to the high solubility of calcium sulfates compared to carbonates, and phosphates. It is found in three stable geological polymorphs defined by the content of water incorporated into their crystal structure: $\text{CaSO}_4 \cdot 2\text{H}_2\text{O}$ (gypsum), $\text{CaSO}_4 \cdot 0.5\text{H}_2\text{O}$ (bassanite) and CaSO_4 (anhydrite). Gypsum is a common mineral found either in discrete deposits or together with other minerals. Statoliths of gypsum were found in the class Scyphozoa (*Aurelia aurita* and *Chrysaora hysoscella*, Semaestomeae)^[50-52] and in the class Cubozoa (*Carybdea rastoni*, Carybdeida; *Chiropsalmus*, Chirodropida)^[50, 53, 54]. Bassanite was recently identified as the inorganic mineral of the statoliths of the scyphozoan medusa *Periphylla periphylla* (Coronatae).^[55-58]

2.2.4. Calcium oxalate

Calcium oxalate is considered to be the most commonly occurring biomineral in higher plants.^[59-61] It occurs in two hydration states in plants, as the monohydrate (Whewellite) and as the dihydrate (Weddelite).^[60, 62] Whewellite is thermodynamically most stable phase of calcium oxalate. Calcium oxalate is the principal biomineral component present in urinal stone together with calcium phosphate. In urinal stones, inorganic crystals are always mixed with organic matrices such as lipids, carbohydrates, and

proteinaceous materials, and studies have shown that, although these organic materials account for only about 2% of the total mass, they play a very important role in the stone-formation process.^[63, 64] Some microorganisms, especially bacteria or nanobacteria, accumulate preferentially in the kidney and have been reported to act as biomineralization centers to induce kidney stones and play an important role in urolithiasis.^[65-71] Instead of promoting the formation of stones, oxalate-eating bacteria such as *Oxalobacter formigenes* can degrade oxalate and prevent the occurrence of calcium oxalate urolithiasis.^[72, 73] Calcium oxalate produced by both plants and fungi^[74, 75] can be transformed into CaCO₃ by bacteria.^[76, 77]

2.2.5. Calcium fluoride

Calcium fluoride (fluorite) is often found as a mixture with other minerals. The statoliths of marine mysid crustaceans are composed of fluorite, and that this mineral is also a principal phase of the gizzard plates of some tectibranch gastropods.^[78] A small percentage of fluorite was found with calcite (CaCO₃) and brucite (Mg(OH)₂) in the fusiform spicules of Doridacean opisthobranchs.^[79]

2.3. Conditions for the precipitation of calcium phosphate crystallization

Calcium phosphates are the mineral component of bones and teeth. It is interesting to understand the physical mechanisms that underline their growth, dissolution and phase stability. Control is often achieved at the cellular level by the manipulation of solution states and the use of crystal growth modulators such as peptides or other organic molecules.

2.3.1. Nucleation

Nucleation is a significant process in biomineralization in constructing complex structures. Nucleation can be described as representing an activation energy barrier to the spontaneous formation of a solid phase from a super saturated solution.^[80] The formation of stable clusters of ions or molecules is required for nucleation as the energy needed to form a new interface (ΔG_I) in the clusters is less than the energy released by the formation of bonds in the bulk solid phase (ΔG_B). Because the surface molecules are less bound to their neighbors than are those in the bulk, their contribution to the free energy of the new phase is greater. Figure 2 shows the free energy barrier for nucleation (ΔG_N) as a function of cluster size (r). The difference between the free energy per molecule of the bulk and that of the surface is referred to as the interfacial energy (ΔG_I). The interfacial energy is always positive and dependent on the surface area. It acts to destabilize the nucleus. As a consequence, at very small nucleus size when many of the molecules reside at the surface, the nucleus is unstable. Adding even one more molecule increases the free energy of the system. As a result,

the nucleus will dissolve. But once the stable nucleus attained, the nucleus grows large enough as the drop in free energy associated with formation of the bulk phase becomes sufficiently high. The surface free energy is unimportant at this stage. Because the bulk energy (ΔG_B) is negative and is a function of volume. Every addition of a molecule to the lattice lowers the free energy of the system.

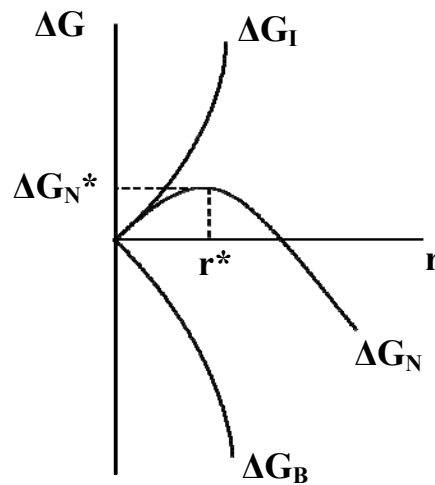


Figure 2: Free energy of nucleation (ΔG_N) as a function of cluster size (r). ΔG_N^* is the activation energy for nucleation and r^* is the critical cluster radius.

The free energy of formation of a nucleus, ΔG_N , is given by the difference between the interfacial and bulk energies:

$$\Delta G_N = \Delta G_I - \Delta G_B$$

The activation energy for nucleation (ΔG_N^*) is given by the following equations:

$$\Delta G_N^* = 16 \pi (\Delta G_I)^3 / 3 (\Delta G_B)^2$$

$$\Delta G_B = k_B T \log S_R$$

where k_B is Boltzmann's constant, T is the temperature, and S_R is the relative supersaturation of the medium.

Supersaturation is a measure of to what extent a solution is out of equilibrium and represents the thermodynamic driving force for inorganic precipitation.^[1] Supersaturation is highly regulated in biology through the process of boundary-organized biomineralization. The supersaturation, S , is a unitless number which is proportional to the difference in chemical potential ($\Delta\mu$) between the supersaturated solution and a solution at equilibrium with the solid.

$$S = \Delta\mu / k_B T$$

The supersaturation determines the mode of crystal growth and the net flow of energy across a given surface. When the solution is undersaturated, the mineral will dissolve. When the solution is supersaturated, the mineral will grow. If the supersaturation is high enough, the activation energy for nucleation (ΔG_N^*) can be decreased. As a result the rate of nucleation can be increased.

Recently, the nucleation mechanism of hydroxyapatite nanocrystallites by the control of chondroitin sulfate was examined from the viewpoints of kinetics and interfacial structure and properties.^[81] Figure 3 shows a scheme of the nucleation and growth mechanism of hydroxyapatite from aqueous solutions with chondroitin sulfate. It was found that chondroitin sulfate can change the interfacial properties of hydroxyapatite by the surface adsorption through the sulfate functional groups. This increased the stiffness of the organic molecule and also created new binding sites for calcium ions at the substrates. These binding sites could highly decrease the activation barrier for the nucleation process and acted as a template for oriented hydroxyapatite nucleation. The negatively charged ChS surface caused a

higher surface supersaturation at the substrate as a result an oriented hydroxyapatite assembly was formed by the growth and the coalescence of crystallites on the surface-modified substrate. Without this template molecule, the hydroxyapatite crystallites obtained from the solution was not ordered and the crystallites were assembled in a random manner.

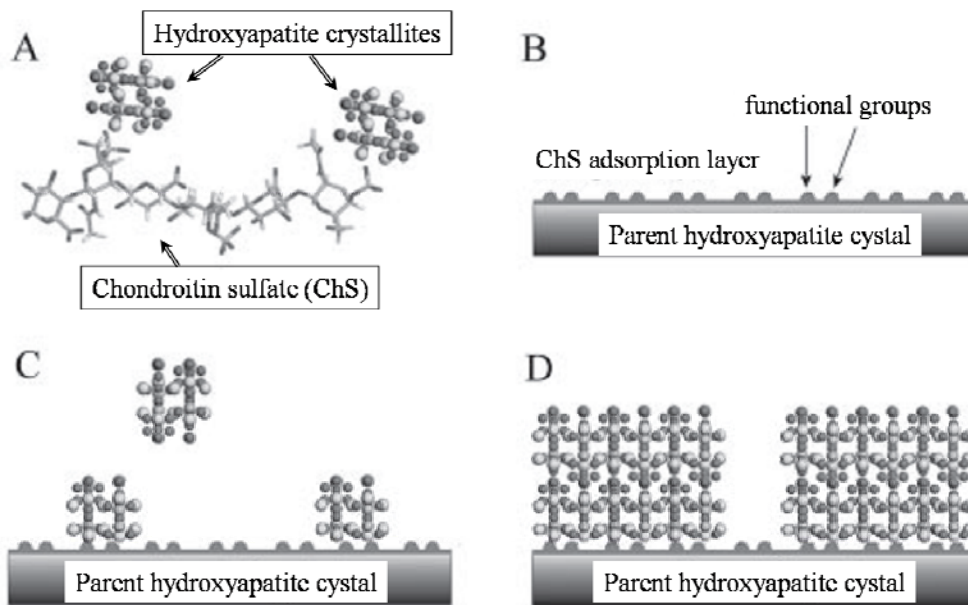


Figure 3: Schematic drawing of the nucleation and growth mechanism of hydroxyapatite from aqueous solutions with chondroitin sulfate (ChS). **A**, strong interaction between ChS and Ca^{2+} , which facilitates the nucleation of hydroxyapatite in solution by producing locally a high degree of supersaturation. **B**, adsorption of ChS on the surface of a parent crystal improving the interfacial correlation. **C**, nucleation and adsorption of growth units on a substrate of ChS. **D**, growth and coalescence of crystallites to form highly oriented hydroxyapatite crystallites on the surface. The figures were adapted from reference.^[81]

So, the interfacial structure match between hydroxyapatite crystallites and substrates was improved by the ChS template during the nucleation process. Therefore, this may be the reason why composites such as hard tissues resulting from mineralization under such conditions will become compact, ordered, and tough.

2.3.2. Thermodynamic and kinetic crystal growth

The thermodynamic driving force for nucleation of calcium phosphate is the reduction of free energy of the system through the formation of a low energy phase, in this case a crystalline phase. The simplest strategy for controlled growth in biomineralization consists of maintaining a low level of supersaturation as shown in Figure 4.

As shown in Figure, the activation energy for the formation of the most stable crystalline phase of a compound is rather high, although it is thermodynamically favoured. The fast growing faces have high surface energies and they will vanish in the final morphology and vice versa. Although this purely thermodynamic treatment cannot always predict the crystal morphology, as crystallization and the resulting morphology often also rely on kinetic effects as well as on defect structures, it is the basis for the explanation of additive-mediated crystal morphology changes in biomimetic mineralization.

Kinetic crystallization control is based predominantly on the modification of the activation energy barriers of nucleation, growth, and phase transformation.^[82] In such cases, crystallization often proceeds by a sequential process involving structural and compositional modifications of amorphous precursors and crystalline intermediates through a kinetically

effective pathway, rather than a one-step thermodynamic pathway.^[82-84] The formation of amorphous and intermediate precursors is faster because the activation energy is much lower. These phases grow and recrystallize into the crystalline phase which is thermodynamically more stable under the conditions of the performed precipitation.

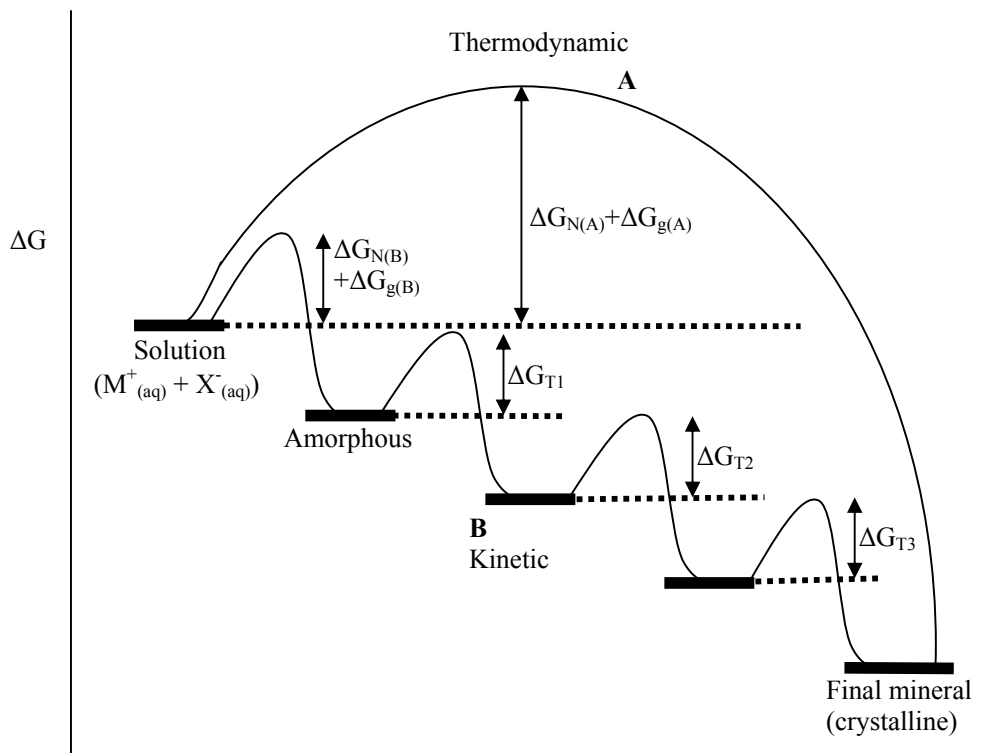
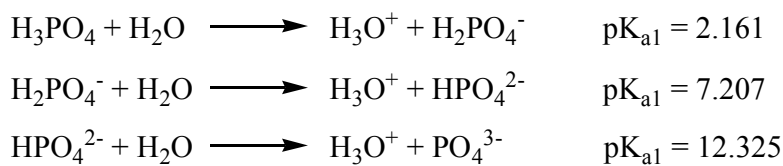


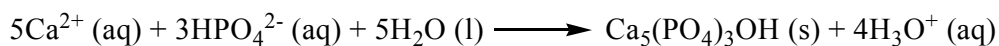
Figure 4: Crystallization pathways under thermodynamic and kinetic control. Pathway A, direct growth from solution, i.e. a system follows a one-step route to the final mineral phase; Pathway B, growth from structurally-modified precursors, i.e. a system proceeds by sequential precipitation. ΔG_N = free energy of nucleation; ΔG_g = free energy of growth; ΔG_T = free energy of phase transformation.

2.3.3. pH

The pH affects both the solution as well as the mineral surface. In the solution, a shift to lower pH will lower the saturation state by shifting the balance of phosphate species from PO_4^{3-} over HPO_4^{2-} to H_2PO_4^- . At the mineral surface, the pH can shift the surface charge by changing the distribution of proton and hydroxyl groups hydrating the interface.



The different phases of calcium phosphate minerals can be obtained by the combination of phosphate and calcium ions under basic pH values. During the precipitation of calcium phosphates from a neutral solution, the pH value generally decreases because of the release of protons that were formerly bound to hydrogen phosphate or dihydrogen phosphate. For hydroxyapatite, the point of zero charge occurs at $\text{pH} = 7.3$.^[2, 42, 108]



Generally when homogeneous precipitation occurs, i.e. spontaneous nucleation and growth, unstable amorphous solids precede the formation of crystalline hydroxyapatite. If the acidity of the solution is increased, other precursor phases such as dicalcium phosphate dihydrate may form in accordance with Oswald's rule of stages^[85] which predicts that the least stable phase having the highest solubility is formed preferentially during a sequential precipitation.

2.3.4. Solubility product

Calcium phosphates are less soluble under basic conditions. In order of increasing stability, the five principal calcium phosphate phases are amorphous calcium phosphate (nonstoichiometric), dicalcium phosphate dihydrate (brushite) ($-\log K_{sp} [37\text{ }^{\circ}\text{C}] = 6.63\text{ mol L}^{-1}$), tricalcium phosphate (whitlockite) ($-\log K_{sp} [37\text{ }^{\circ}\text{C}] = 29.55\text{ mol L}^{-1}$), octacalcium phosphate ($-\log K_{sp} [37\text{ }^{\circ}\text{C}] = 97.4\text{ mol L}^{-1}$), and hydroxyapatite ($\text{Ca}_{10}(\text{PO}_4)_6(\text{OH})_2$) ($-\log K_{sp} [37\text{ }^{\circ}\text{C}] = 117.3\text{ mol L}^{-1}$).^[2, 86] The final ratio present in each of these phases can affect the bulk and interfacial chemistry of the final calcium phosphate material.

2.3.5. Temperature

Temperature is generally an important crystal growth parameter, although it is not a variable in a regulated environment such as the body. Solubility products and association constants are affected mainly by a change in temperature because they are temperature-dependent. Temperature also affects the kinetics of adsorption, desorption, and diffusion.

2.3.6. Presence of ions or additives

The surface energy of a crystal face can be lowered by the adsorption of an additive. Therefore, the shape of crystals can be affected by various factors, i.e. inorganic ions or organic additives. The anisotropic growth of the particles can be explained by the specific adsorption of ions or organic additives to particular faces, therefore inhibiting the growth of these faces by lowering their surface energy. Only the additives that can adsorb on special

crystal faces can change the surface energies of the different crystal faces and change the crystallization process and the final morphology. For example, the substitution of the hydroxide ions in hydroxyapatite by fluoride ions results in greater structural stability. It is interesting to note that the incorporation of F^- stabilizes the lattice and reduces its solubility. Shark enamel has a 1000 times higher fluoride concentration than the human enamel.^[87] The small concentration of fluoride is beneficial in protecting the enamel of our teeth. The etching of enamel in our teeth by acidic food or beverages resulting in the dissolution of calcium hydroxyapatite can be lowered by replacing some hydroxide ions by fluoride ions. The salts of phytic acid inhibits effectively the crystallization of brushite in urine^[88]. Kakizawa et al. prepared nanoparticles consisting of calcium phosphate, DNA and block-copolymers. A small size of the particles and good colloidal stability were achieved by the steric effect of a poly(ethylene glycol) (PEG) layer surrounding the calcium phosphate core.^[89, 90]

2.4. Hollow inorganic nanoparticles

Hollow inorganic micro- or nanostructures have attracted considerable attention because of their promising applications such as nanoscale chemical reactors, catalysts, drug-delivery carriers, lightweight fillers, low-dielectric materials or photonic crystals. Hollow structures of inorganic materials have been fabricated by template-assisted synthesis or template-free synthesis.

2.4.1. Principles and methods of the synthesis of hollow inorganic particles

Template-assisted synthesis is the mostly approached method to produce hollow inorganic structures. The general approach is the use of various removable or sacrificial templates, including hard (inorganic nanoparticles,^[91] monodispersed silica^[92, 93] or polymer latex spheres,^[94-99] glass microspheres,^[100, 101] and reduced metal nanoparticles^[102, 103]) and soft templates (emulsion droplets^[104, 105]/micelles^[106-113] and gas bubbles generated from a reaction mixture^[114]).

A common template-assisted method to prepare nanostructures with a hollow interior is that the surfaces of templates are coated with thin layers of the desired material or its precursor, followed by the selective removal of the templates which involves the use of organic solvents (oil droplets and polystyrene spheres), strong acids (metal and inorganic nanoparticles) or calcination (micelles).

For example, Peng et al.^[114] used N₂ microbubbles as templates to produce hollow microspheres of ZnSe (Fig. 5). In this study, the N₂ gas bubbles were generated in situ during the reduction of SeO₃²⁻ by hydrazine. Although the

template method satisfies the structural requirements to prepare hollow nanostructures, the removal of template turns out to be a difficult process in some cases.

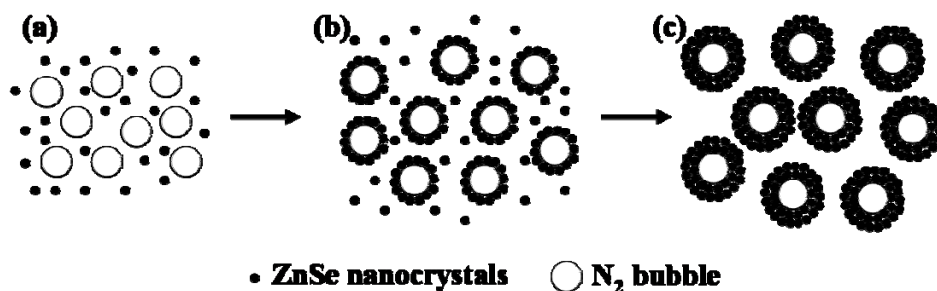


Figure 5: Schematic representation of the aggregation of ZnSe nanocrystals over N₂ gas bubbles. Step (a): Reduction of SeO₃²⁻ by hydrazine to form Se atoms and N₂ microbubbles. The Se atoms were further reduced with alkaline solution to produce Se²⁻ ions which reacted with ZnO₂²⁻ or Zn²⁺ ions to form ZnSe nanocrystals. Step (b): Aggregation of ZnSe nanocrystals around gas-liquid interface between N₂ gas bubbles and water. Step (c): Finally the formation of hollow microspheres of ZnSe. The figure was adapted from reference.^[114]

Template-free methods, involving self-assembly of nanoparticles,^[115] oriented attachment of nanoparticles,^[116, 117] Ostwald ripening^[118, 119] and the Kirkendall effect^[120-122] have been proposed recently to prepare hollow nanostructures of inorganic materials. These are the mostly preferred methods because of their easy way of one-pot synthesis and for the controlled preparation of hollow nanostructures in a wide range of sizes.

Self-assembly of nanoparticles can produce higher-order architectures in situ by mesoscale transformation processes that involve metastable inorganic-based colloidal aggregates.^[82, 115] The self-assembly process is mainly driven by the interactions of organic ligands which are adsorbed on the inorganic

minerals.^[123, 124] Recently, self-assembly of polymer-stabilized TiO₂ and SnO₂ solid nanoparticles with sizes of a few nanometer into hollow microspheres at relatively low temperatures has been reported.^[115]

Oriented attachment is known as a combination of nanocrystallites through their suitable surface planes, i.e., with the same crystallographic orientation.^[125] This process refers to the crystal growth via direct attachment of the existing crystal planes or facets. An immediate result of this process is the dimensional multiplication of original basic units which can effectively produce the larger structures. By this method, a larger interior space can not be generated although intercrystallite porosity can be attained depending on the structural shapes of the primary building units. The oriented attachment of nanocrystallites is mainly driven by the internal core of the primary nanoparticles. Contrary to self-assembly of nanoparticles, oriented attachment is only observed for ligand-free nanoparticles.^[124] The formation of hollow “Dandelions” structures by the mesoscale organization of CuO nanoribbons was reported^[116] (Fig. 6).

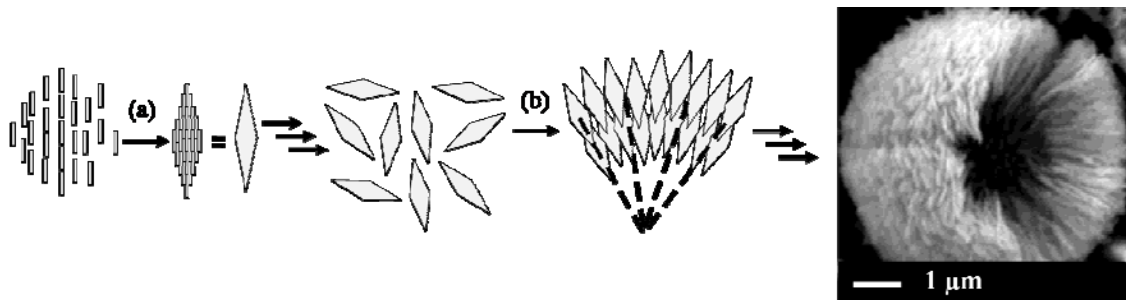


Figure 6: Schematic illustration of a two-step process of the dandelion organization of CuO: (a) oriented aggregation of CuO nanoribbons to form rhombic shaped nanostructure, and (b) geometric shape limiting assembly of the rhombic shaped nanostructures into a shell structure. The figures were adapted from reference^[116]

Ostwald ripening commonly refers to the solution process in which large crystals grow at the expense of small ones. It is a suitable technique to prepare both crystalline and amorphous particles. Here the principle is to produce the initial spherical particles for which the external surface layer is less soluble compared to the interior core of the particles. It means that the external surface layer should have higher crystallinity and should be energetically more stable compared to the interior core particles. In order to minimize the surface energy of core particles during the ripening process, large crystallites on the external layer are essentially immobile while the smaller interior core particles tend to diffuse through solution and recrystallizing. This process creates the interior hollow space within the original aggregates. Based on this technique, numerous hollow inorganic particles have been synthesized.

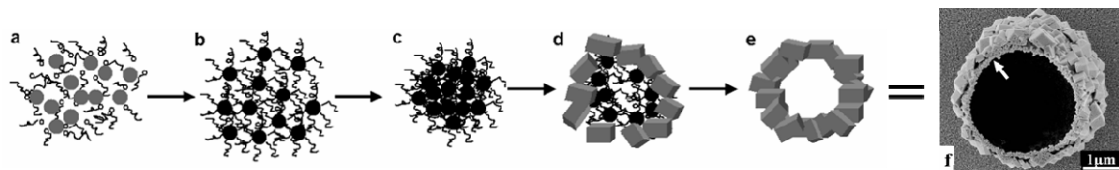


Figure 7: The proposed formation mechanism of calcite hollow spheres. (a) The polymer-stabilized amorphous nanoparticles. (b) Formation of spherical vaterite precursors. (c) Aggregation of the vaterite nanoparticles. (d) Vaterite–calcite transformation starting on the outer sphere of the particles. (e) Formation of calcite hollow spheres under consumption of the vaterite precursor. (f) SEM image of hollow CaCO_3 particle. The figures were adapted from reference.^[32]

For instance, Yu et al. reported the synthesis of hollow CaCO_3 microparticles in the presence of double-hydrophilic block copolymers^[32] (Fig. 7). The crystallization of a calcite rhombohedral structure occurred on

the initially formed vaterite (thermodynamically less stable) particles. These rhombohedral crystals then grew at the expense of the dissolving vaterite particles by Ostwald ripening, resulting in a hollow sphere. The inner part of the hollow particle consisted of tiny primary nanocrystals with a grain size of about 320 nm as indicated by the arrow.

The Kirkendall effect was found by E. O. Kirkendall^[121] as a diffusion phenomenon in metallurgy and normally refers to comparative diffusive migrations among different atomic species in metals and alloys under heating conditions. For example zinc diffuses into copper faster than copper diffuses into brass in a brass-copper interface due to their different atomic diffusivities.^[125] As a result from this diffusion process, porosity will be generated in the lower-melting component side of the diffusion couple. Based on this technique, hollow nanoparticles are formed by crystalline materials, such as ZnO, CuS, and Co₃S₄.^[126-128]

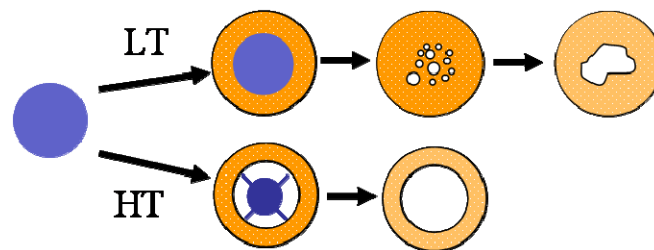


Figure 8: Schematic illustration of formation of cobalt sulfide (Co₃S₄, linaeite) hollow spheres by the Kirkendall effect. The figure shows the temperature dependence of hollow particle evolution at low (LT) and high (HT) temperatures. The figures were adapted from reference^[128]

Yin et al.^[128] synthesized linaeite (Co₃S₄) hollow particles by reacting colloidal cobalt nanoparticles with molecular sulfur in solution (Fig. 8). The

void formation process was dominated by outward diffusion of cobalt cations. At room temperature, hollow cobalt sulfide nanoparticles were observed only after 19 hours but the voids were in irregular shape. The reaction rate increased dramatically with increase of temperature. At 120°C, the well-centered circular voids were observed within 20 minutes.

2.5. Colloids

The term colloid (which means “glue” in Greek) was first introduced in 1861 by Thomas Graham to describe the “pseudosolutions” in aqueous systems of silver chloride, sulfur, and Prussian Blue which were prepared by Francesco Selmi in the mid-nineteenth century.^[129] Graham deduced that the colloidal size range is approximately 1 μm down to 1 nm (i.e. $10^{-6} - 10^{-9}$ m). The colloids are generally described as systems consisting of one substance finely dispersed in another. These substances are referred to as the dispersed phase and dispersion medium (or continuous phase) respectively. The colloid system can be a solid, a liquid, or a gas.

2.5.1. Functionalization of calcium phosphate nanoparticles

Calcium phosphate particles in the nanometer scale tend to aggregate immediately due to van der Waal's forces. The nanoparticles must be stabilized as colloids where the repulsive forces between the nanoparticles must be provided to balance this attraction. Generally two types of stabilization are used to prevent agglomeration of nanoparticles, namely, electrostatic stabilization and steric stabilization by adsorbed molecules or steric hindrance. Electrostatic stabilization involves the creation of an electrical double layer arising from ions adsorbed on the surface and associated counter ions that surround the particle. Thus, if the electric potential associated with the double layer is sufficiently high, the Coulomb repulsion between the particles will prevent their agglomeration (Fig. 9). The functionalization can stabilize the particles against fusion or agglomeration and thus assure a homogeneous distribution within the

colloidal solution. Steric stabilization can be achieved by the adsorption of large molecules such as polymers at the surface of the particles. The calcium phosphate nanoparticles functionalized with DNA provide both electrostatic and steric stabilization.

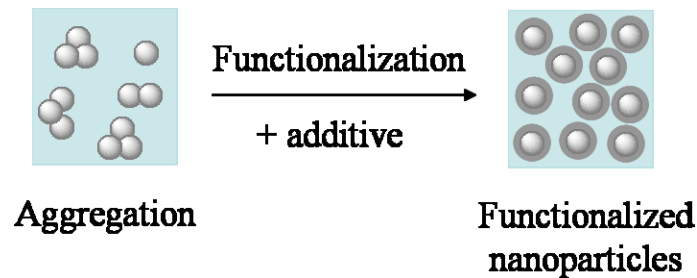


Figure 9: Schematic diagram illustrates the solid particles in colloidal solution. The unfunctionalized nanoparticles tend to collide and aggregate (left side) and functionalized nanoparticles repel each other (right side).

Surface functionalization of calcium phosphate nanoparticles can modify the physical properties of the nanoparticles (e.g. surface charge density, solubility, dispersive nature, etc). Figure 10 shows the model for the stabilization of positively charged nanoparticle by charging the surface with counter ions. The specific adsorption of additives or ions on the particles surface, even at low concentrations, can have a dramatic change in zeta potential. The zeta potential is the difference in electrical potential between the dense layer of ions surrounding the particle and the bulk of the suspended fluid. For example, the charge of the calcium phosphate nanoparticles is slightly positive above pH 7. After functionalizing the surface of calcium phosphate nanoparticles with nucleic acids, the zeta potential value was reduced to negative (-20 to -30 mV), i.e. the surface was charged negatively because of the non-covalent adsorption of negatively

charged nucleic acids on the positively charged calcium phosphate surface.^[22]

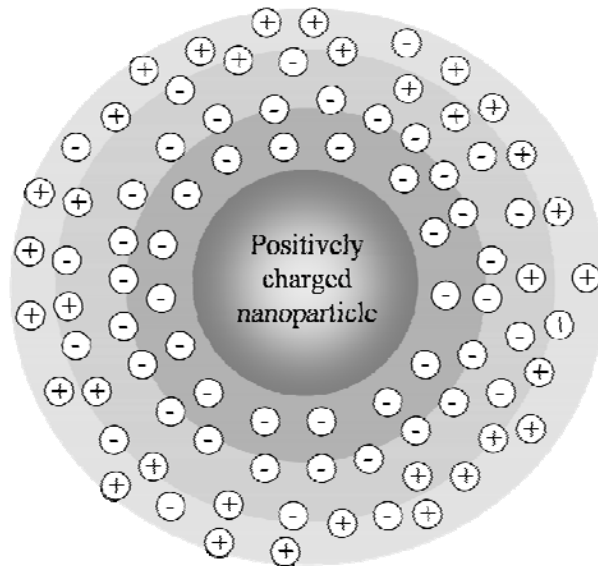


Figure 10: Schematic representation of the stabilization of a positively charged nanoparticle by charging the surface with counter ions.

Lebugle et al. functionalized the hydroxyapatite surface with (hydroxyethyl)methacrylate phosphate and dodecanol phosphate by a coprecipitation method in order to disperse the hydroxyapatite particles in polymers as a filler cement used in dental and medical therapies^[130-132].

2.6. Organic phosphates as functionalizing agents

Biological molecules possessing phosphate functional groups form a large part of the cellular matrix. Their importance is underlined by their presence in nucleic acids, proteins, carbohydrates, lipids, coenzymes, and steroids.

2.6.1. Porphyrin

Porphyrins are ubiquitous class of naturally occurring compounds with many important biological examples including hemes, chlorophylls, myoglobins, cytochromes, uroporphyrin, coproporphyrin, catalases, peroxidases, etc. They are utilized by the nature in importance of many biological processes, for instance oxygen storage and transport (myoglobin and hemoglobin), electron transport (cytochromes b and c), oxygen activation and utilization (cytochrome P450 and cytochrome oxidase), photosynthesis in plants and bacteria (chlorophyll and pheophytins) and several others.

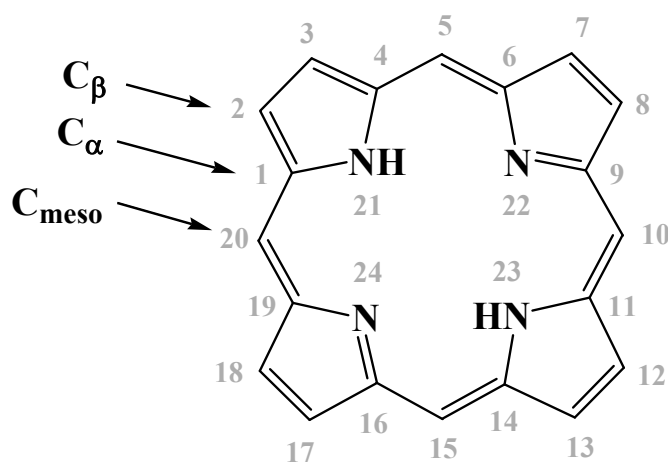


Figure 11: Chemical structure of the porphyrin skeleton.

The parent macrocyclic structure shown in Figure 11 is called porphyrin, a name originally used (in hematoporphyrin) by Hoppe-Seyler in 1877^[133]. The porphyrin contains a fundamental skeleton of four pyrrole nuclei united through the α -positions by four methine groups to form a conjugated macrocyclic structure (porphyrin is designated porphine in the Chemical Abstracts index). The numbering of ring positions including nitrogen is also shown in Figure 11. The Greek letters are sometimes used to distinguish the types of carbon positions. This macrocyclic structure has 22 π electrons; among them only 18 π electrons are involved in aromaticity according to Hueckel's rule.

Porphyrin compounds are known as analytical reagents with highly sensitive spectrometric and/or spectrofluorimetric properties. A very intense absorption band is known as the Soret band^[134], named after the biochemist who first observed it in hemoglobin. The Soret band normally occurs around 400 nm in the near ultraviolet ($\epsilon > 10^5 \text{ dm}^3 \text{ cm}^{-1} \text{ mol}^{-1}$) followed by four weaker absorptions (Q bands) at higher wavelengths from 450 to 700 nm. The protonation of the inner nitrogen ring or insertion/change of metal atoms into the macrocycle strongly affects the electronic conditions and causes major changes in the absorption spectra of porphyrin. A disrupted porphyrin macrocycle results in the disappearance of the Soret band^[135]. Upon the formation of a metalloporphyrin complex, the absorption spectrum of the Soret band shows a slight red shift, whereas the four weaker Q bands merge into two bands at the higher wavelength between 500 to 650 nm^[136].

The porphyrin macrocycle and its derivatives are amphoteric, behaving both as acid and as base. The nitrogen atoms at the centre of the porphyrin core are responsible for this interesting property. The N-H groups can be deprotonated with strong bases, while the two-imine nitrogens can be

protonated with acids. However, metalloporphyrin lacks this amphoteric quality because the nitrogen atoms are chelated to the metal with both covalent and dative bonds. The NMR spectrum of the aromatic tetrapyrrole shows anisotropic effects.^[137-140] The ring current generated by the applied field induces a local magnetic field similar to that in benzene. The N-H protons inside the porphyrin ring system are therefore shifted upfield to as high as -5 ppm in porphyrins whereas the deshielded *meso*-protons appear at very low field ($\delta \approx 10$ ppm).^[141] The pyrrolic protons are also deshielded and tend to resonate at $\delta = 8$ to 9, versus $\delta \approx 6$ ppm in pyrrole. Although the aromaticity of these porphyrin systems makes their NMR spectra a challenge to assign, the tendency towards aggregation in some cases causes even more complicated spectra^[142]. Another fundamental aspect of the chemistry of porphyrins is the tautomerism of the “inner” hydrogen. The tautomerism of N-H was shown by low-temperature ¹H- and ¹³C-NMR spectroscopy.^[143-145] Porphyrins are well known fluorescing molecules. They are extensively used as photosensitizers in photodynamic therapy for the treatment of cancer. Photodynamic therapy, the name arises from the term *photodynamische Wirkung* (photodynamic effect) coined by German physiologists to describe the damage of a living tissue by a combination of photosensitizer, visible light and oxygen.^[146, 147] Bonnett described schematically the important steps involved in medical treatment of cancer cells using photodynamic therapy,^[146] which is shown in Figure 12. The porphyrins can be administered both in dissolved form as well as adsorbed on nanoparticles.^[148-152] The distribution of porphyrin in the body is still under examination. Since the porphyrins are solids, a liquid medium is needed for injection purposes. It is known that 70 % of the human body weight is composed of water. The porphyrin skeleton (see Fig. 11) is adequately

hydrophobic. Sufficient solubility of the sensitizer in aqueous media is important for direct intravenous application and transport to the intended target location. Hydrophobic, insoluble sensitizers can be transported by water-soluble carriers ^[153-155]. The possible carriers are micellar suspensions or liposomes, biopolymers (nucleic acids), serum proteins (albumin, high-density lipoproteins and low-density lipoproteins), antibodies (natural carriers), and container molecules (cyclodextrins, calix[n]arenes) ^[156].

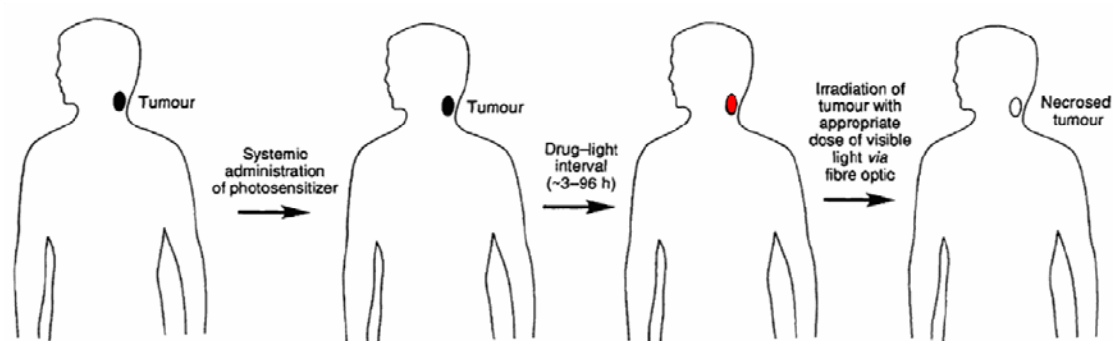


Figure 12: Schematic diagram of photodynamic therapy using a photosensitizing agent. Figure was adapted from reference. ^[146]

After administration of porphyrin in tumor tissue, visible light of a specific wavelength is used to irradiate the tumor which causes excitation of porphyrin. This energized porphyrin will react with molecular oxygen and other substrates generating highly reactive cytotoxic species e.g. singlet oxygen, peroxides, superoxide anion, hydroxyl radical which will destroy the tumor cell preferentially.

Hematoporphyrin, is named by Hoppe-Seyler ^[157], was the first porphyrin administered in PDT, which is available from blood. In 1841 Sherer isolated hematoporphyrin from blood, during experiments investigating the nature of blood ^[158]. In 1913 Meyer-Betz injected himself with 200 milligrams of hematoporphyrin, in order to determine its photosensitivity in human. He

registered no ill effects until he exposed himself to sunlight, whereupon he suffered extreme swelling, this photosensitivity remained for several months [159]. Lipson et al described that hematoporphyrin derivative is a diagnostic tool for PDT [160].

2.6.2. Phytic acid

Phytic acid, *myo*-inositol-1,2,3,4,5,6-hexakisphosphate is present in large amounts in plants, seeds and grains. It is called phytate when it exists in the salt form. It is commonly found in nature and exists in plants in the form of its mixed calcium and magnesium salts (called phytin). About 60~90% of the entire amount of phosphorus occurring as organic phosphate in plants are in the form of phytin.

Phytic acid is also found in animal blood. It has a beneficial role as hemoglobin cofactor^[161] in the regulation of oxygen transport in human blood.^[162-164] The presence of phytate in normal urine^[165] exerts a potent action as crystallization inhibitor of oxalate and phosphate salts of calcium in urine.^[166-168] The primary enzymes responsible for the degradation of phytic acid are phytases. Phytases are a special class of phosphatases that catalyze the sequential hydrolysis of phytic acid to inositol phosphates and, in some cases, to inositol.

The conformation of phytic acid has been a topic of much interest. In the solid state, the hydrated dodecasodium salt of phytic acid adopts the conformation that contains five phosphates in axial (ax) positions and one phosphate in equatorial (eq) position (5ax/1eq)^[169, 170] (Fig. 13). The driving force for adopting the sterically hindered 5ax/1eq form is the minimization of electrostatic repulsion between the five contiguous dianionic phosphates

in the equatorial positions and stabilization of the axial phosphates by coordination with sodium ions and hydrogen-bonding interactions with water.^[170] In aqueous solution, the 1ax/5eq form exists below pH 9.5. Above this pH, the stable conformation is the 5ax/1eq form.^[170-173]

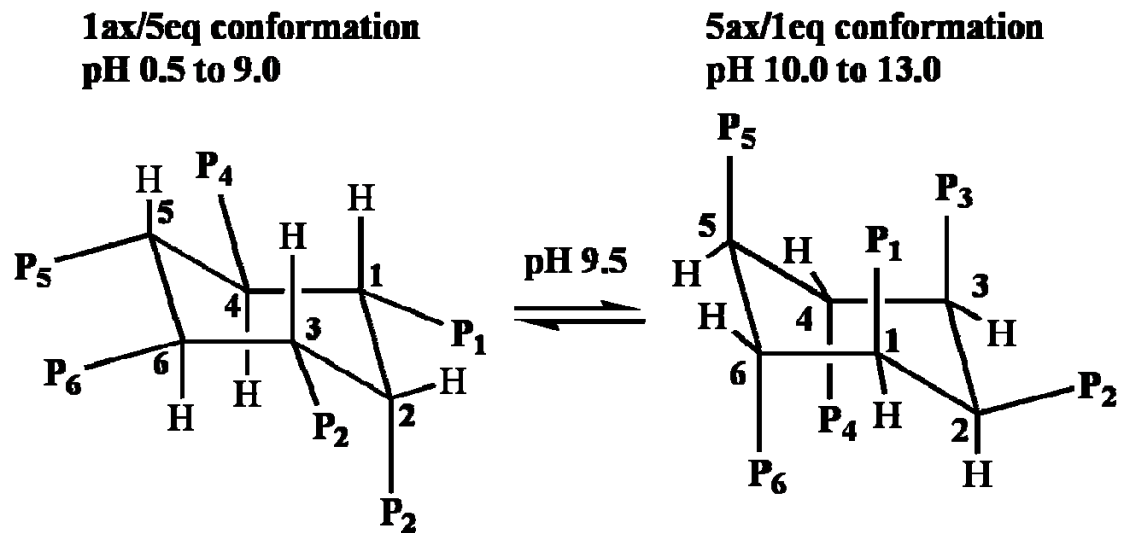


Figure 13: 5ax/1eq and 1ax/5eq conformations of phytic acid. P = $-\text{OPO}_3\text{H}_2$, $-\text{OPO}_3\text{H}^-$ or $-\text{OPO}_3^{2-}$, depending on the pH. The numbering corresponds to cyclohexyl carbons carrying the phosphate groups. Each phosphorus atom is labeled with the same number as the carbon to which it is linked.

Phytic acid has the ability to bind minerals^[174-176] and results in lower absorption of these elements in the body. However, recent work has shown that phytic acid has many health benefits. Phytic acid and its derivatives play an important role in RNA export, DNA repair, and DNA recombination in endocytosis and vesicular trafficking.^[177] Phytic acid acts as an anticancer agent, and its action can be explained by its mineral-chelating potential.^[178] Like other organic phosphates, it has a cariostatic effect that was ascribed to

its ability to inhibit the dissolution of tooth enamel by strong adsorption of phytate to the calcium phosphate surface of enamel.^[179] Thereby, it is able to prevent the formation of cavities.^[180-183]

2.6.4. Amino acids with phosphate functional groups

The term “protein” is derived from the Greek word *proteuein* which means “to be first”. Naturally occurring proteins consist of polymers of twenty two different amino acids.

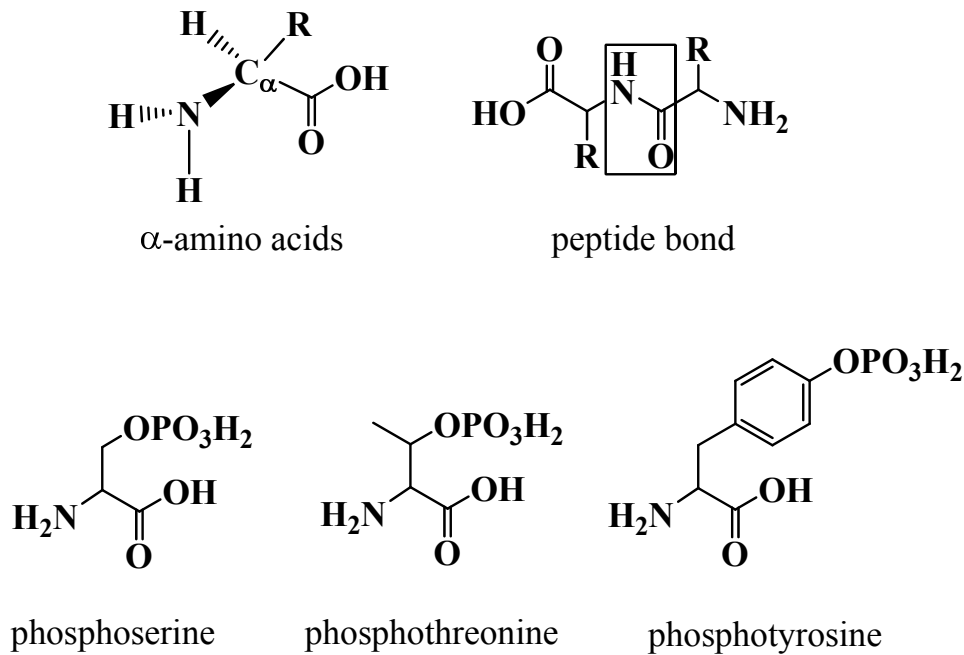


Figure 14: The generalized structure of α -amino acids (top left) and the peptide bond, a linkage between two amino acids (top right). The chemical structures of phosphoserine, phosphothreonine and phosphotyrosine are illustrated in the bottom line (from left to right).

Amino acids consist of an alpha carbon atom (C_{α}) which is bound to an amino group ($-NH_2$), a carboxyl group ($-COOH$), a hydrogen atom ($-H$) and a side chain R (Fig. 14). Amino acids are distinguished from one another by differences in their side chains. When amino acids are combined, an amide linkage called a peptide bond is formed and a molecule of water is released. Two amino acids form a dipeptide, three amino acids form a tripeptide, and many amino acids form a polypeptide.

Phosphoserine, Phosphothreonine and phosphotyrosine are examples for phosphoamino acids (Fig. 14). In living cells, protein-phosphorylation occurs on serine, threonine and tyrosine residues. Generally, enzymes called kinases are involved in the process of phosphorylation and phosphatases are responsible for the dephosphorylation of proteins. The reversible phosphorylation of proteins is an important regulatory mechanism which occurs in both prokaryotic and eukaryotic organisms.^[184-187]

Tyrosine-phosphorylation is of great significance in cancer research because it inhibits the growth of human renal and breast carcinoma cells *in vitro*^[188], although phosphotyrosine is less abundant than phosphoserine and phosphothreonine.^[189] The enzymes called protein tyrosine kinases are involved in the phosphorylation of tyrosine and the activation of this enzyme results in an increase in overall cellular phosphotyrosine levels and induction of cell proliferation. The protein tyrosine phosphatases are enzymes that are found at cytosolic as well as at transmembrane sites. They are involved in the dephosphorylation of phosphotyrosyl residues of cellular proteins.^[190, 191] *O*-phospho-L-tyrosine can activate cellular protein tyrosine phosphatases which inhibits the cell cycle by dephosphorylating the cellular phosphotyrosine and decreasing the activity of EGFR (epidermal growth factor receptor) kinase.^[188, 190, 192] Mishra et al. reported that the incubation of

cells with *O*-phospho-L-tyrosine can lead to an arrest of cell growth, but this does not work with phosphothreonine or phosphoserine.^[190]

Phosphoproteins are proteins containing phosphate (PO₄) groups. The addition of a phosphate molecule to a polar -R group of an amino acid residue can turn a hydrophobic portion of a protein into an extremely hydrophilic portion of molecule. Casein, vitellin, osteopontin, statherin, phosphophoryn are the best known phosphoproteins and they comprise the clusters of phosphoseryl residues.

Phosphoproteins play a key role in promoting or inhibiting the growth of minerals like hydroxyapatite. The proline-rich acidic proteins such as statherin found in human salivary fluids function as an inhibitor of primary and secondary crystallization of the biomineral hydroxyapatite.^[193-196]

Recently, it has been predicted from NMR studies that phosphoserines of statherin protein play a vital role in binding affinity with hydroxyapatite through strong electrostatic interaction.^[205, 207, 209] Makrodimitris et al. proposed a model for the interaction of statherin with the hydroxyapatite surface^[197] (Fig. 15).

Casein phosphopeptides bind to forming nanoclusters of amorphous calcium phosphate in metastable solution through their multiple phosphoseryl residues, thereby preventing their growth to the critical size required for nucleation and phase transformation. Conformational and binding studies have shown that all the phosphoseryl residues are important in interaction with amorphous calcium phosphate. The composite of casein phosphopeptide-amorphous calcium phosphate can be added to sugar-containing foods as well as oral care products for the control of dental caries.^[198]

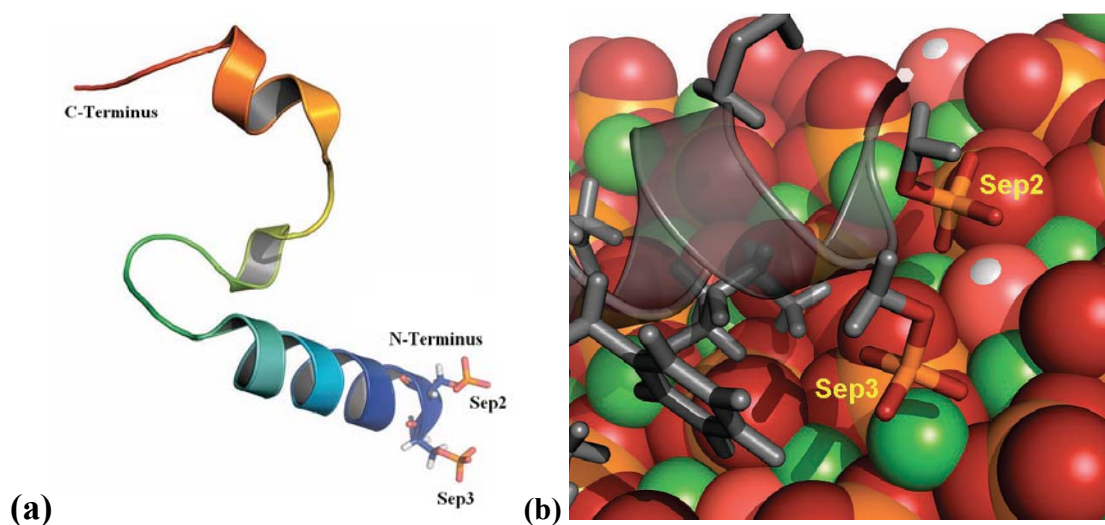


Figure 15: The model structure of statherin and its adsorption onto the hydroxyapatite surface. (a) Statherin structure adapted from reference^[197]. Sticks depict the two phosphoserine (Sep) side chains Sep2 and Sep3. (b) The interaction of statherin with the hydroxyapatite surface through anionic phosphate groups of phosphoserine. Sep3 chelates a Ca^{2+} ion (green) and Sep2 forms hydrogen bonds.

Osteopontin is an acidic phosphoglycoprotein that is active in the prevention of soft tissue calcification. *In vitro* studies have shown that osteopontin can inhibit the formation of hydroxyapatite and other biologically relevant crystalline phases, and that this inhibitory activity requires the phosphorylation of the protein.^[199] Osteopontin can be phosphorylated by casein kinase II, cAMP-dependent protein kinase, Golgi casein kinase and protein kinase C.^[200-202] Threonine and serine are the amino acids that are phosphorylated in osteopontin.^[203]

Phosphoryn which is found in the dentin matrix is highly phosphorylated, and the phosphate groups are important for its function as a mediator of dentin mineralization.^[204, 205]

2.6.1. Surfactants

Surfactants or surface-active agents are amphiphilic organic molecules which upon dissolution in a solvent at low concentration have the ability to adsorb at interfaces, thereby altering significantly the physical properties of those interfaces. Amphiphiles are described with regard to their “hydrophilic” and “hydrophobic” moieties, or “head” and “tail” respectively. Surfactants are soft templates and they have been found to play key roles in bio-inspired synthesis for mimicking the biomineralization process.

Surfactants can form a wide variety of aggregate morphologies (Fig. 16). The morphology of the aggregate is determined by the molecular structure of the individual surfactant molecule and is the result of the interplay between the attractive hydrophobic interactions between the tails and the repulsive electrostatic and hydration shell overlap interactions between the head groups.^[206]

A micelle is a highly dynamic aggregate of surfactant molecules. The average residence time of a surfactant molecule in a micelle is around 10^{-5} to 10^{-6} seconds, the lifetime of a micelle is 10^{-2} to 10^{-3} seconds.^[207] The shape and size of the micelle is also subjected to variations.^[208] A typical micelle consists of 40 to 100 amphiphile molecules^[209]. The diameter of a micelle is about 5 nm. In 1925, a bilayered structure was proposed for cell membranes.^[210] Later it was found that phospholipids extracted from cell membranes can form closed bilayer aggregates.^[211] These structures are

called liposomes and have been frequently used as membrane models.^[212] Vesicles consist of an aqueous compartment enclosed by a bilayer composed of amphiphiles. The hydrophobic part of the amphiphiles forms the inner core of the bilayer, whereas the hydrophilic head groups are located at the bilayer–water interface.

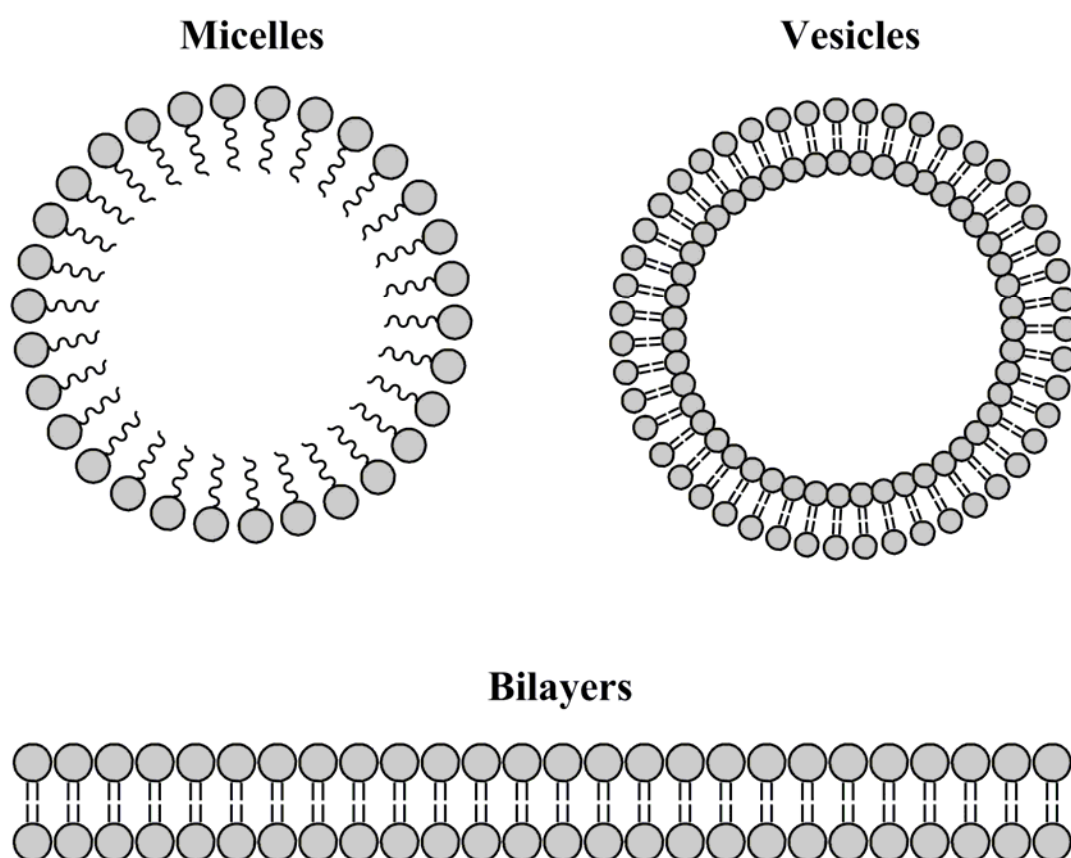


Figure 16: Representation of micelles, vesicles and bilayers.

Disodium monoalkyl phosphates are found to form both vesicles and micelles, depending of the pH conditions of the aqueous solutions.^[213-216] Vesicles are normally formed at low pH^[214], whereas micelles are formed at high pH.^[215]

3. Results and discussion

3.1. Synthesis and characterization of *p*-TPPP-functionalized calcium phosphate nanoparticles

Calcium phosphate nanoparticles can be used as gene/drug carrier for nucleic acids^[8] or for antitumour drugs.^[14, 15] Recently, Han et. al. showed the influence of nanoapatite on cancer cells.^[217] The experimental results indicated that the apatite nanoparticles got into the cancer cells, inhibited the growth of cancer cells and showed appearance of cell death. He also proposed the possible mechanism that the uptake of apatite nanoparticles result in the DNA damage on tumour cells and increase the cytosolic Ca²⁺ concentration which lead to apoptosis of tumor cells. Therefore, calcium phosphate nanoparticles can be used as antitumour drug and also possibly as antitumour drug carriers.

Porphyrin and metal porphyrin complexes are well known fluorescing molecules with high stability and high fluorescence efficiency. They are also extensively used as dyes in photodynamic therapy for the treatment of cancer after uptake in tissue and irradiation with light, both in dissolved form as well as adsorbed on nanoparticles.^[148-152]

In the current study, calcium phosphate nanoparticles stabilized with a water-soluble porphyrin having four phosphate functional groups, namely 5,10,15,20-tetrakis(4-phosphonooxyphenyl)porphine (*p*-TPPP), to improve the interaction with the calcium phosphate surface. Porphyrin-functionalized calcium phosphate nanoparticles may be used as biocompatible fluorescing nanoparticles.

3.1.1. Synthesis of 5,10,15,20-tetrakis(4-phosphonooxyphenyl)porphine (*p*-TPPP)

5,10,15,20-tetrakis(4-phosphonooxyphenyl)porphine (*p*-TPPP) belongs to a class of meso-substituted synthetic porphyrins. It can be directly synthesized from 5,10,15,20-tetrakis(4-hydroxyphenyl)porphine (*p*-THPP) by phosphorylation of the hydroxyl groups. Kawakami et al.^[218] prepared this compound using a mixture of pyrophosphate and phosphorus pentoxide as phosphorylating agents. By this method of preparation, it was difficult to purify the final product and the yield was also very poor. A two step procedure was followed to prepare *p*-TPPP from *p*-THPP. In the first step, *p*-THPP was phosphorylated. Di-tert-butyl-N,N-diethyl-phosphoramidite was used as phosphitylating agents. MCPBA (*meta*-chloro perbenzoic acid) was used as oxidizing agent. The deprotection was achieved in the second step by acid treatment (HCl/1,4-dioxane) of the first step product. The phosphorylation (step a) and the deprotection (step b) are shown in Figure 17. The procedure is easy and the product is obtained in high yield. Di-tert-butyl-N,N-diethylphosphoramidite was prepared in high yield and also with high purity (90-95%), according to reference.^[219] This reagent is a highly reactive phosphitylating agent, which after activation with 1H-tetrazole reacts rapidly with an aryl alcohol. The nitrogen group of phosphoramidite can be protonated by 1H-tetrazole, thus converting the amine into a good leaving group.^[220] The phosphorus atom is then attacked by alcohol. At this point the phosphorus atom is in the +III oxidation state. After treating the alcohols with phosphoramidites, an oxidizing step is necessary to convert the phosphorus from the +III oxidation state to the +V oxidation state. The subsequent oxidation of the resultant alkyl or aryl phosphate triesters with MCPBA proceeds rapidly and gives phosphate triesters.

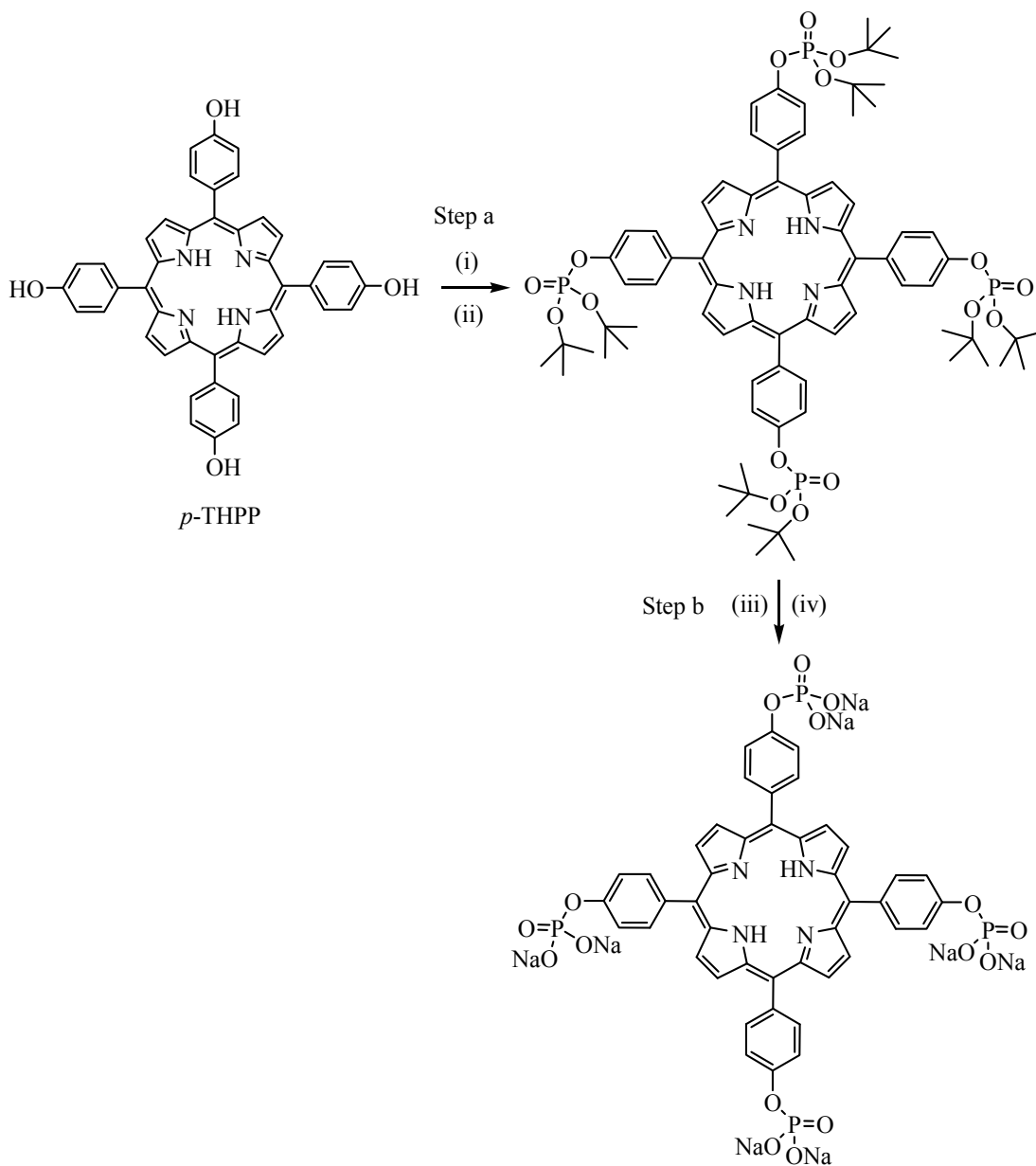


Figure 17: Schematic diagram illustrating the synthesis of the sodium salt of *p*-TPPP. Reagents and conditions: step a: phosphorylation (i) $[(\text{CH}_3)_3\text{CO}]_2\text{P-NEt}_2$ /DMF/1H-tetrazole; (ii) MCPBA/ CH_2Cl_2 ; step b: deprotection (iii) HCl/1,4-dioxane; (iv) NaOEt/EtOH.

3.1.2. Preparation of stable colloids by optimizing the concentration of *p*-TPPP

The calcium phosphate nanoparticles were prepared by pumping aqueous solutions of $\text{Ca}(\text{NO}_3)_2 \cdot 4 \text{H}_2\text{O}$ (3 mM, pH 9.5) and $(\text{NH}_4)_2\text{HPO}_4$ (1.8 mM, pH 10) into a stirred vessel.^[221] A few seconds after mixing, the nanoparticle dispersion was taken with a syringe. The colloids were prepared by rapidly mixing an aqueous solution of the sodium salt of *p*-TPPP and the dispersed calcium phosphate nanoparticles in a 5 ml:10 ml ratio. A stable colloid was prepared by the addition of the sodium salt of *p*-TPPP (30 μM) solution to the dispersed calcium phosphate nanoparticles. The size distribution data from dynamic light scattering (DLS) showed an average particle size of about 250 nm with a polydispersity index (PDI) ≤ 0.1 . The stability of the colloidal nanoparticles was followed by DLS. The colloid stored at room temperature was stable for about a week, while the colloid stored at 4 to 8 °C in refrigerator was stable for about two weeks. Increasing the concentration of the sodium salt of *p*-TPPP to more than 30 μM resulted in a flocculation of a green precipitate after 3 hours.

The unfunctionalized calcium phosphate particles have a slightly positive zeta potential of about +1.2 mV at a pH of 8.0.^[22] The adsorption of *p*-TPPP (30 μM) reduced the zeta potential to -31.5 mV, which indicates the good adsorption of *p*-TPPP phosphate groups on the calcium phosphate surface.

Scanning electron microscopy was performed to obtain a direct view on the nanoparticles. In the case of the colloid with the addition of 30 μM of *p*-TPPP, the SEM picture shows spherical particles with a size of 250 nm (Fig. 18a), confirming the results from DLS measurements. When increasing the concentration of *p*-TPPP to 60 μM , we found a mixture of spherical particles

and long rods (Fig. 18b). A further increase in concentration of *p*-TPPP gave only long rods.

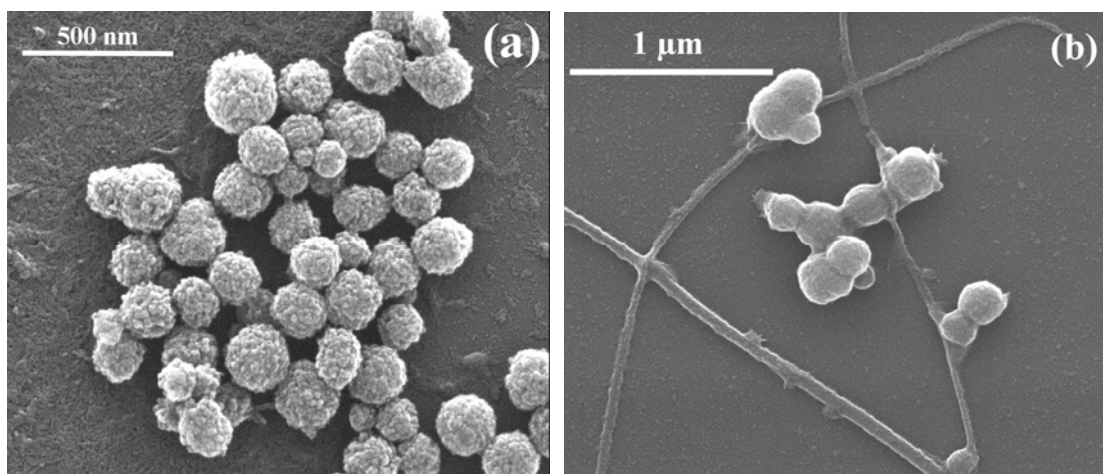


Figure 18: SEM picture of functionalized calcium phosphate nanoparticles after the addition of (a) 30 μM of *p*-TPPP, and (b) 60 μM of *p*-TPPP.

3.1.3. Analyzing the effective functionalization of *p*-TPPP on the calcium phosphate surface

The stable colloid with 30 μM of *p*-TPPP was analyzed to determine the effective adsorption of *p*-TPPP on the calcium phosphate surface. The functionalized calcium phosphate nanoparticles were separated by ultracentrifugation from the dissolved *p*-TPPP and the counter-ions from the calcium phosphate preparation. The amount of dissolved *p*-TPPP in the supernatant was about 30 % as determined by UV spectroscopy, i.e. about 70 % of the total amount of the added *p*-TPPP was adsorbed on the calcium phosphate surface. The content of *p*-TPPP in the nanoparticles was estimated as follows: If we assume that all calcium and phosphate precipitated as hydroxyapatite, $\text{Ca}_5(\text{PO}_4)_3\text{OH}$, the content of *p*-TPPP in the solid phase is 5.52 wt%. If only 70 % of those are adsorbed, the content of *p*-TPPP

decreases to 3.9 wt%. Elemental analysis of the *p*-TPPP-doped spherical nanoparticles by combustion elemental analysis gave 2.32 wt% C and 2.73 wt% H. As hydrogen can also come from hydroxide groups and from adsorbed water, only the carbon content was used. This gave 5.2 wt% of *p*-TPPP in the solid. It was concluded that the loading of *p*-TPPP in the solid was around 4-5 wt%. We ascribe the difference between the two methods to experimental uncertainties.

Elemental analysis of the flocculated rod-like particles which were obtained at the higher concentration of *p*-TPPP (0.6 mM) gave 38.12 wt% C and 3.85 wt% H. Computed from the carbon value, about 85 % of *p*-TPPP was present in the solid. The calcium salt of *p*-TPPP can be formed.

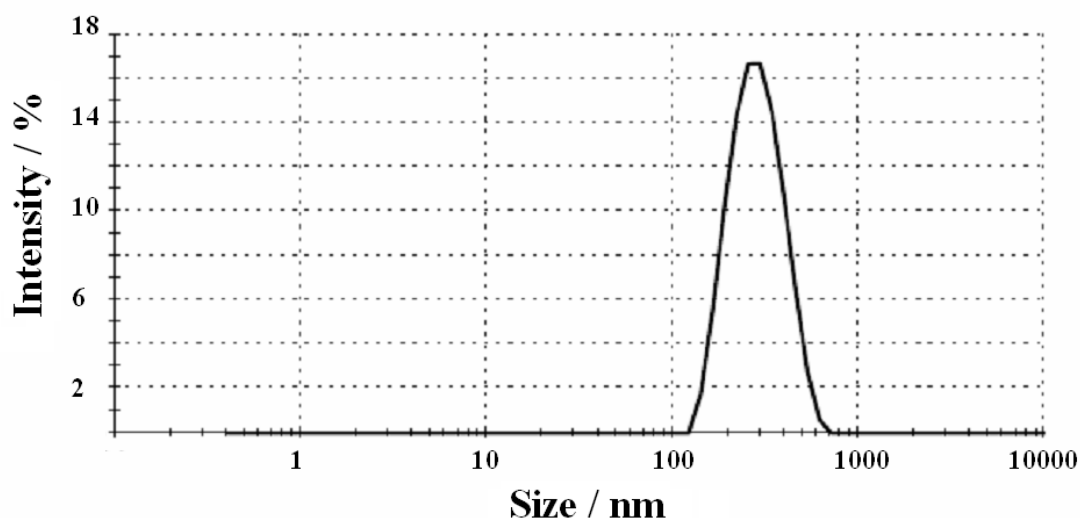


Figure 19: Size distribution data of the redispersed colloid at pH 7.4 from dynamic light scattering.

The isolated spherical nanoparticles were easily redispersable in water by ultrasonication. The redispersed nanoparticles showed a particle size of

about 250 nm with a PDI value 0.023 (Fig. 19), consistent with the dynamic light scattering data of the initial colloid, the particles did not change during the centrifugation and redispersion. The adsorption of *p*-TPPP reduced the zeta potential to -18.7 mV at a pH of 7.4, which indicates the good adsorption of the negatively charged phosphate groups of *p*-TPPP on the calcium phosphate surface.

Scanning electron microscopy of the redispersed colloid showed spherical particles with a size of 250 nm, confirming the results from DLS measurements (Fig. 20).

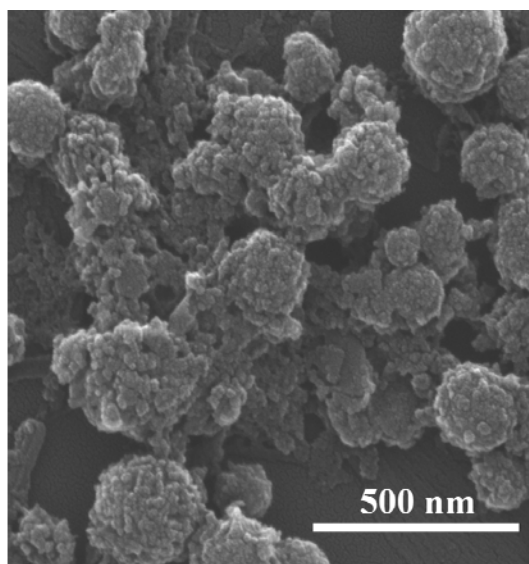


Figure 20: SEM picture of the redispersed colloidal nanoparticles.

IR data of the sodium salt of *p*-TPPP and *p*-TPPP-functionalized calcium phosphate nanoparticles are compared in Figure 21. The spectrum of *p*-TPPP-functionalized calcium phosphate nanoparticles shows two major broad bands at 1057 cm^{-1} and 577 cm^{-1} which are assigned to the PO_4^{3-} group in calcium phosphate. The vibrational bands of the sodium salt of *p*-

TPPP were also observed in the functionalized nanoparticles, confirming that the calcium phosphate surface is functionalized by *p*-TPPP.

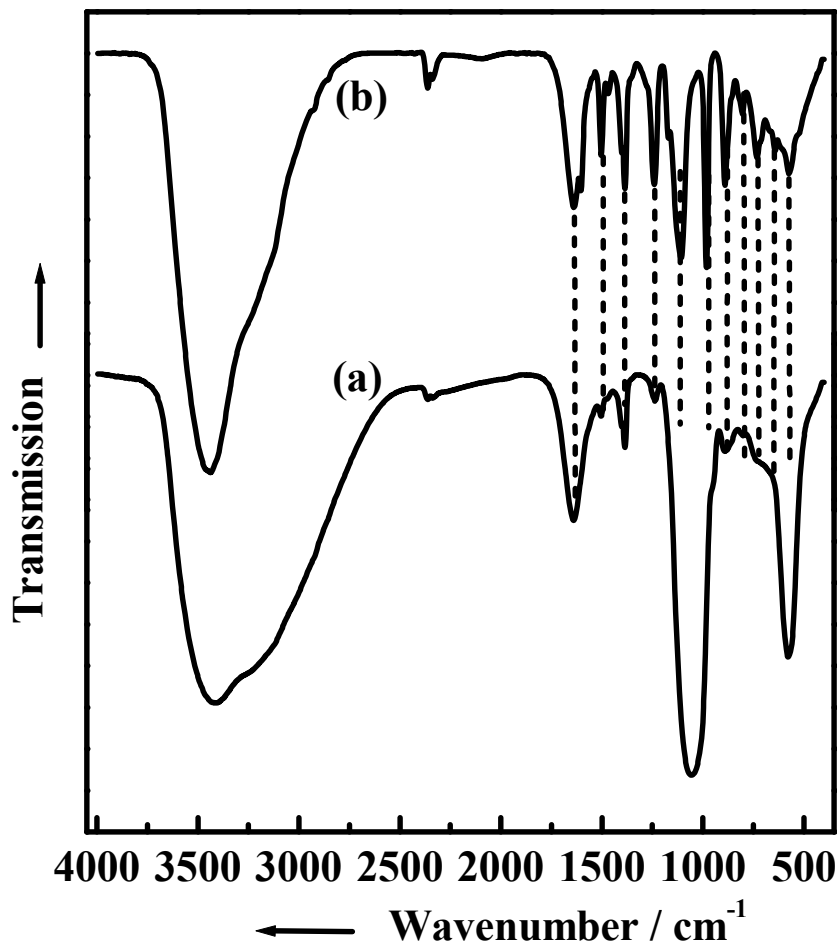


Figure 21: Comparison of IR data of *p*-TPPP-functionalized calcium phosphate nanoparticles (a) and of the sodium salt of *p*-TPPP (b). The vertical dotted lines correspond to the bands of the sodium salt of *p*-TPPP.

X-ray powder diffraction data of *p*-TPPP-functionalized calcium phosphate nanoparticles are shown in Figure 22, indicating their almost amorphous internal structure.

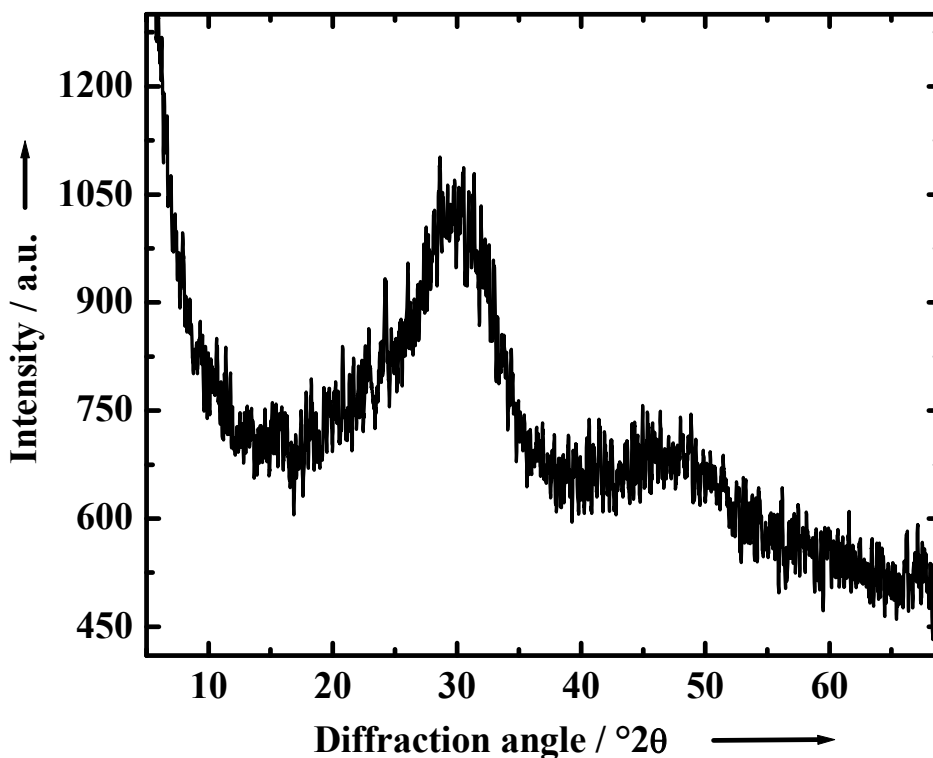


Figure 22: XRD data of *p*-TPPP-functionalized calcium phosphate nanoparticles. The broad peaks indicate a very low crystalline order (note that the peak maxima correspond to those of hydroxyapatite).

The absorption spectrum of an aqueous solution of *p*-TPPP is shown in Figure 23. Above pH 8, *p*-TPPP shows a soret band at 416 nm.^[218, 222] The protonation of the pyrrole ring (to H_4P^{2+}) starts below pH 8 and a red shift of the soret band from 416 nm to 438 nm is observed at pH 5 (Fig. 23). The change in absorbance in the pH range of 5 to 8 is due to the protonation of the pyrrole base. A pronounced decrease in absorbance is observed below pH 1 and above pH 12 which is due to the precipitation of the corresponding

salt of *p*-TPPP.^[218] Taking this effect into account, a pH between 5 and 10 was chosen for all UV experiments.

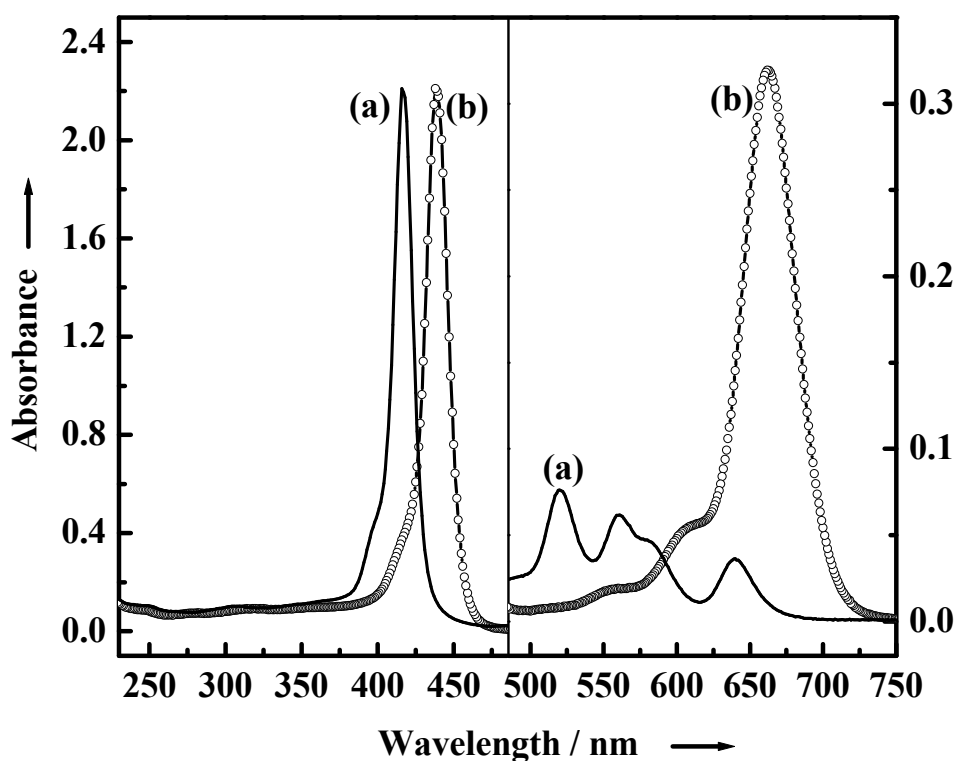


Figure 23: UV-vis spectra of 6 μM of *p*-TPPP in water at pH 9 (a) and at pH 5 (b).

Figure 24a shows the absorption spectrum of the redispersed colloid at pH 7.4. It has a soret band at 417 nm with a shoulder at 440 nm. In the Q band region, a new broad band occurs at 663 nm. Figure 24b shows the aqueous solution of *p*-TPPP at pH 7.4 where it exists as a partially protonated form with the soret bands at 417 nm and 442 nm, and the Q bands at 520 nm, 560 nm, 584 nm, 641 nm and 672 nm. Comparing the spectrum of the redispersed colloid with the free *p*-TPPP at pH 7.4, the shift of the soret

bands and Q bands to the base form of *p*-TPPP (H_2P) and the slight increase of the baseline towards the lower wavelength of the spectrum indicate the adsorption of *p*-TPPP on the calcium phosphate surface.

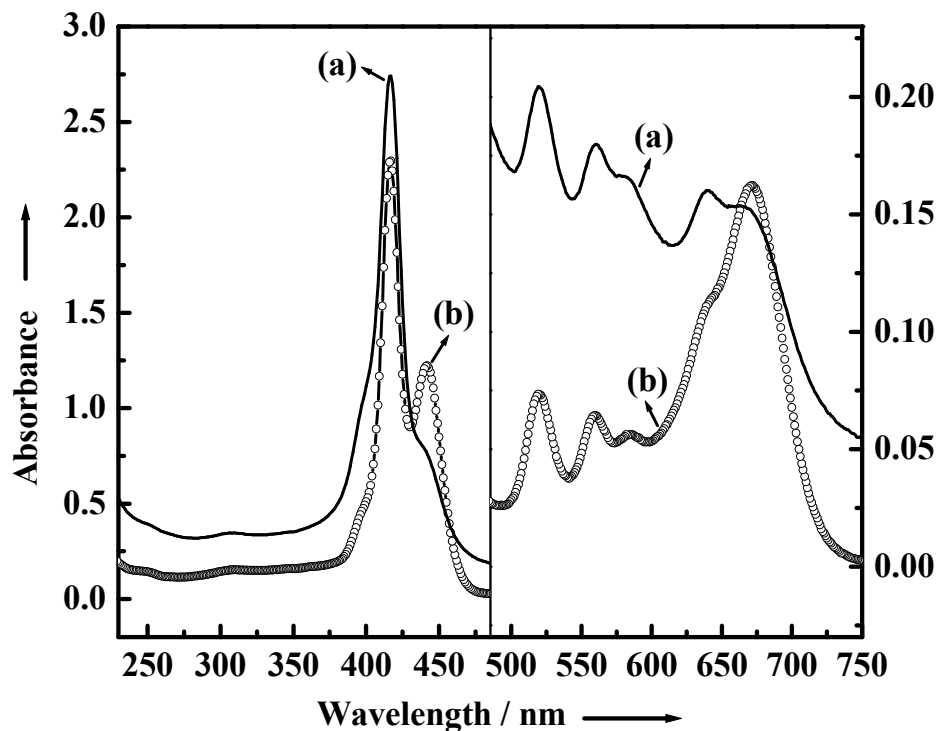


Figure 24: UV-vis spectra of the redispersed colloid (effective concentration of *p*-TPPP: $10 \pm 2 \mu\text{M}$) (a) and of an aqueous solution of *p*-TPPP ($10 \mu\text{M}$) (b), both at pH 7.4.

At an excitation wavelength of 410 nm, the emission spectrum of the redispersed colloid consists of a strong band at 653 nm with a shoulder at 705 nm (Fig. 25). At pH 7.4, the partially protonated form of *p*-TPPP shows two strong bands at 650 nm and 712 nm in the emission spectrum (Fig. 25). This spectrum was compared with the emission spectrum of the redispersed

colloid. In the case of the redispersed colloid, a broad shoulder was observed at 705 nm, instead of a strong peak at 712 nm. The observed spectral changes in the absorption and emission spectra of the redispersed colloid are probably caused by the electrostatic interaction of *p*-TPPP with the calcium phosphate surface.

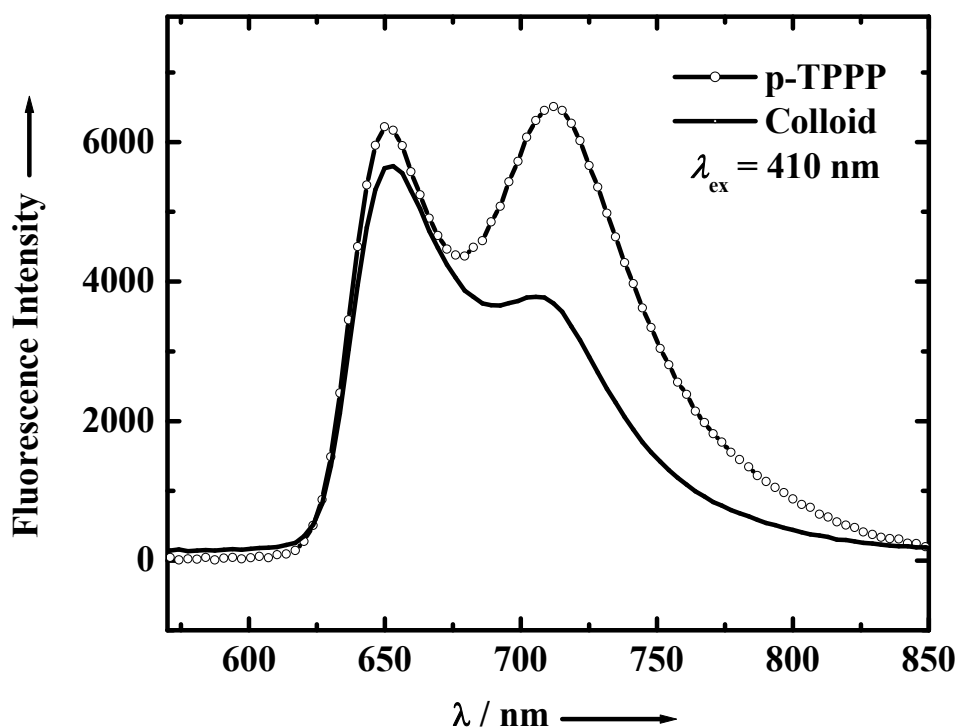


Figure 25: Comparison of fluorescence emission spectra of the redispersed colloid (effective concentration of *p*-TPPP: 10 ± 2 μM) and of an aqueous solution of *p*-TPPP (10 μM) at pH 7.4.

The emission spectrum of the solid *p*-TPPP-functionalized calcium phosphate nanoparticles was also measured. The particles were excited in

the near UV region at 306 nm (Fig. 26). The emission spectrum showed two strong peaks at 472 nm and 597 nm.

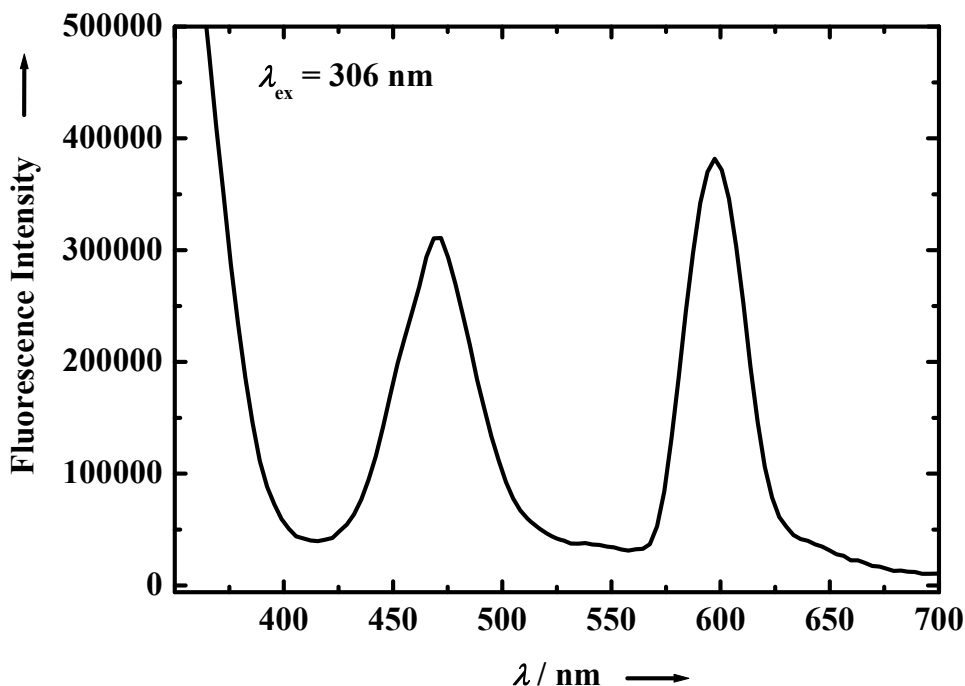


Figure 26: Fluorescence emission spectrum of solid *p*-TPPP-functionalized calcium phosphate nanoparticles.

3.1.4. Experiments with NIH 3T3 fibroblast cell culture

In the cooperation with the Chair of Molecular Neurochemistry, University of Bochum and Ms. Anna Kovtun, cell culture studies were carried out. The biocompatibility of the functionalized nanoparticles was studied with an NIH 3T3 fibroblast cell culture. An MTT test confirmed the absence of toxicity (Fig. 27). Similar results were obtained for longer incubation times (24 and 48 h).

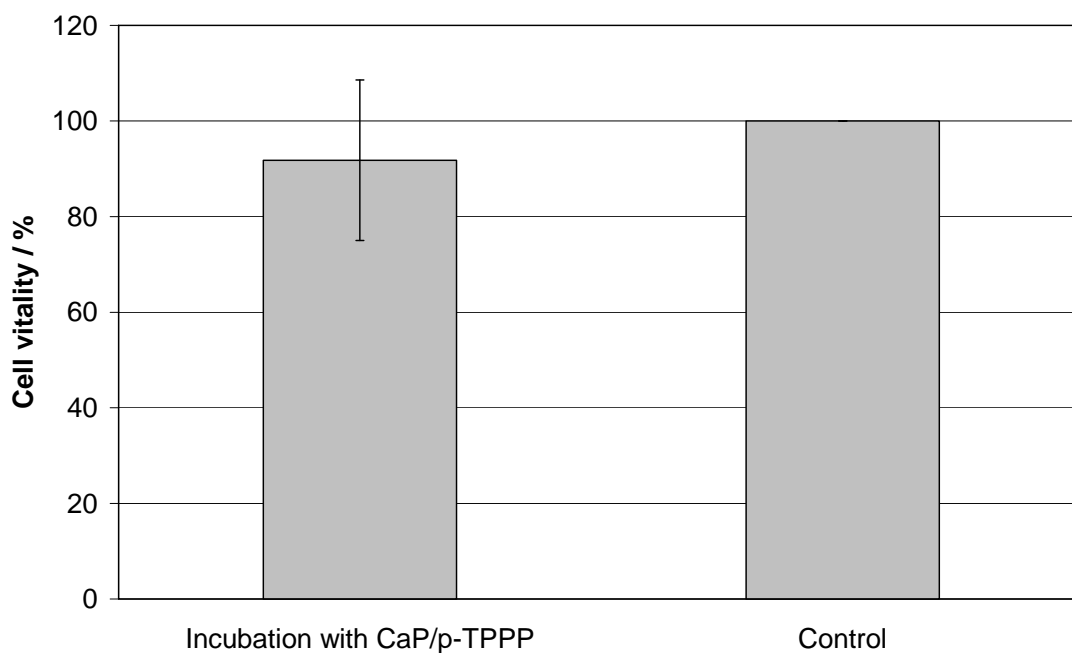


Figure 27: Results of the MTT test after 7 h incubation with *p*-TPPP-functionalized calcium phosphate nanoparticles. The decrease in the cell vitality is not statistically significant.

The functionalized nanoparticles were readily taken up by cells. This could be shown by transmission fluorescence microscopy (Fig. 28). *p*-TPPP shows a strong red fluorescence which is both widely distributed inside the cells, indicating a partial dissolution of the nanoparticles under release of the dye. This gives a red fluorescing background which also shows the cell contours. This confirms that the nanoparticles were taken up by the cells and had partially dissolved. Because the cells were washed twice with PBS before fluorescence microscopy, the medium which also contained dissolved dye and dispersed nanoparticles was removed, i.e. we see only the dye within the cells (and possibly a small amount adsorbed on the cell surface). By

changing the contrast, it is possible to highlight the individual nanoparticles inside the cells as dark-red dots. The extended cell morphology confirms their healthy state in the presence of the nanoparticles.

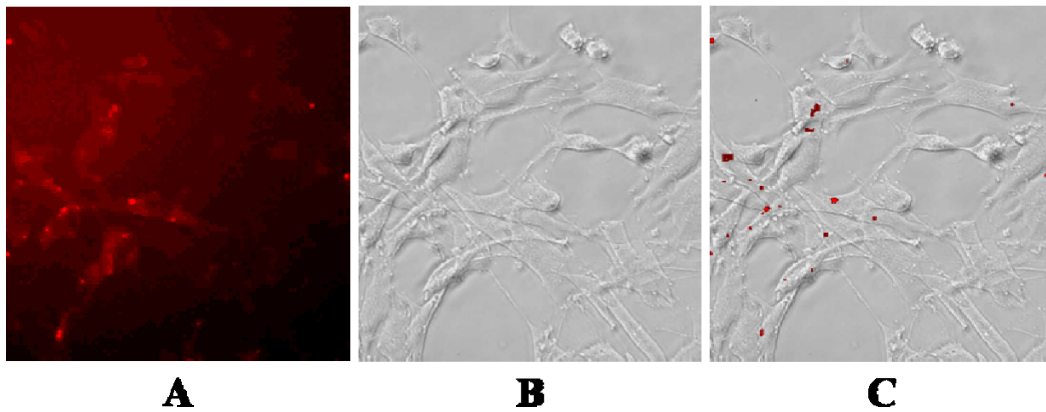


Figure 28: Fluorescence (**A**) and transmission light (**B**) microscopy of NIH 3T3 fibroblast cells after 7 h incubation with *p*-TPPP-functionalized calcium phosphate nanoparticles. **C** shows an overlay of **A** and **B** after removal of the background. In this case, only the nanoparticles are visible (see text).

By confocal laser scanning microscopy, it was shown that the red fluorescing nanoparticles are in fact present inside the cells and not just adsorbed on their surface. A series of horizontal cuts through one cell is shown in Figure 29.

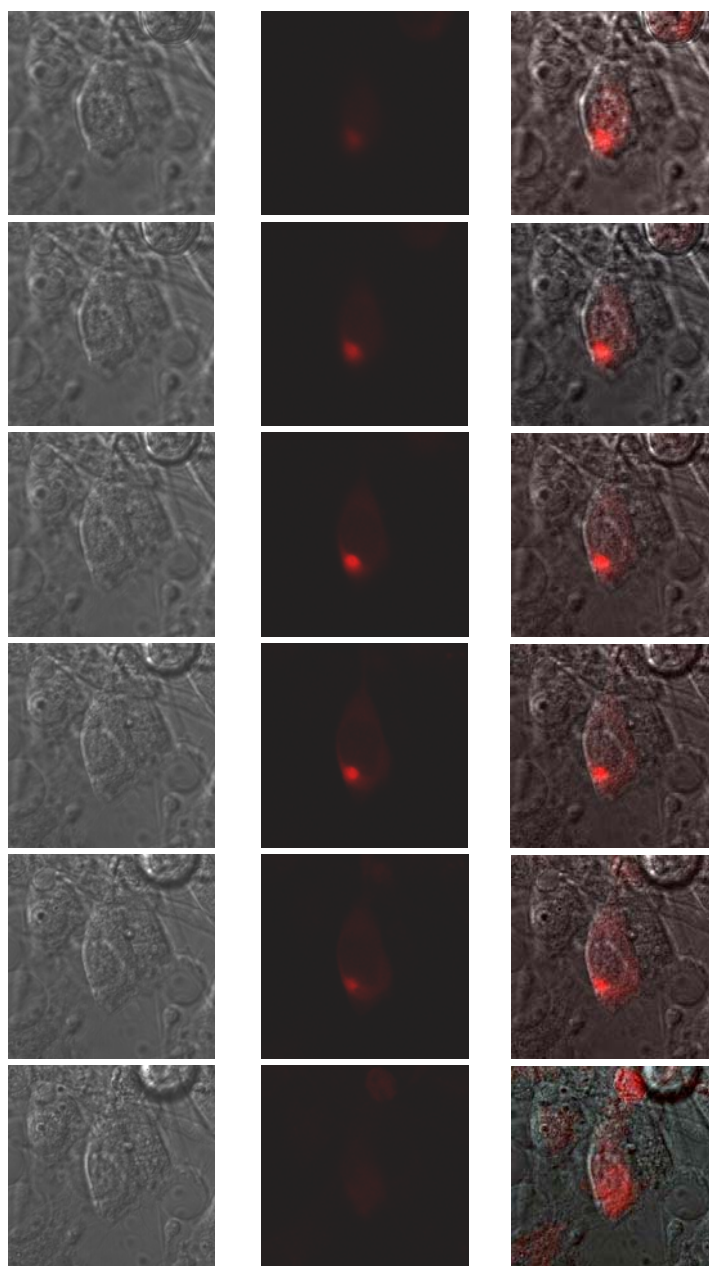


Figure 29: A series of horizontal cuts through a cell, recorded with a confocal laser scanning microscope, 48 h after incubation with *p*-TPPP-functionalized calcium phosphate nanoparticles. It clearly shows that the red fluorescing nanoparticle is present inside the cell. **Left:** Transmission light microscopy; **Centre:** Confocal fluorescence microscopy. **Right:** Overlay of light microscopy and confocal fluorescence microscopy.

3.1.5. Conclusions

We have prepared stable colloids of calcium phosphate nanoparticles by coating their surface with a phosphate-functionalized porphyrin (*p*-TPPP). The dye is the only agent needed for colloidal stabilization, and no other compounds are present. The spherical particles have a diameter of about 250 nm and consist of poorly crystalline calcium phosphate with a loading of 4-5 wt% of porphyrin. The photophysical properties of the redispersed colloid confirm the electrostatic interaction of *p*-TPPP with the calcium phosphate surface and demonstrate its good fluorescence in the visible region of the spectrum. The uptake of the nanoparticles into NIH 3T3 fibroblast cells occurs after a few hours, and the dye is released into the cytoplasm by dissolution of the nanoparticle. No adverse effects on the cells were observed. The nanoparticles may therefore be used as fluorescing agents and (even more interesting) for the delivery of the fluorescing dye into the cell. As a carrier into the cell, the porphyrin-loaded nanoparticle has the advantages that it can be easily taken up by cells. They transport a considerable amount of dye into the cell and dissolve into the harmless byproducts calcium and phosphate. A size of nanoparticles of about 100-300 nm was shown to be efficient in photodynamic therapy.^[223-225] Therefore, a good performance in photodynamic therapy is expected.

3.2. Synthesis and characterization of calcium phytate nanoparticles from calcium phosphate nanoparticles

Phytic acid, *myo*-inositol-1,2,3,4,5,6-hexakis phosphate is a member of the isomer family of 1,2,3,4,5,6-hexakis(phosphate) cyclohexane with a six-fold substitution of phosphate. Therefore, it is characterized by a high density of phosphate groups which are able to interact with a calcium phosphate surface. It is also an abundant biomolecule in humans, animals and plants and therefore of high biocompatibility.^[177, 179] By its six phosphate groups, it has a strong chelating effect to bind multivalent cations which can lead to an undesired depletion of metals like Zn^{2+} , $Fe^{2+/3+}$, Ca^{2+} , Mg^{2+} , Mn^{2+} , and Cu^{2+} in the body.^[179, 226] With calcium ions, it immediately forms an insoluble salt, i.e. calcium phytate.

Calcium phytate is also an effective absorbent for heavy metals like lead.^[227, 228] An in-situ precipitation of calcium phytate is used together with radioactive markers as dispersion for scintigraphy in the liver and spleen^[229-232] and also commercially available as kit.^[231] However, the particle size is about 100-300 nm and the stability of the dispersion is only about 6 h at room temperature.^[231] Calcium phytate particles are unstable in solution. They tend to agglomerate and precipitate immediately.

A method of preparation of colloids of calcium phytate nanoparticles is described in the present study. Synthetically prepared calcium phosphate nanoparticles are reacted with sodium phytate, leading to an anion exchange in the surface and thereby to stable calcium phytate nanoparticles which may be used, e.g., for scintigraphy, as food additive or as additive to dental-care formulations. In this method, the calcium phosphate nanoparticles were used as nuclei.

3.2.1. Optimizing the concentration of phytic acid to prepare the stable colloids of calcium phytate nanoparticles

Calcium phosphate nanoparticles were prepared by rapidly pumping aqueous solutions of $\text{Ca}(\text{NO}_3)_2 \cdot 4 \text{H}_2\text{O}$ (3 mM and 18 mM, pH 9) and $(\text{NH}_4)_2\text{HPO}_4$ (1.8 and 10.8 mM, pH 9) with an equal volume rate into a stirred vessel.^[233] The ratio of calcium to phosphate (5:3) always corresponded to that in hydroxyapatite, $\text{Ca}_5(\text{PO}_4)_3\text{OH}$, i.e. the calcium phosphate which is formed under these conditions.^[2] A few seconds after mixing, the dispersed calcium phosphate nanoparticles were taken with a syringe. The colloids were then prepared by rapidly mixing an aqueous solution of dodecasodium phytate (Na_{12}PA) and the dispersed calcium phosphate nanoparticles in a 10 ml:10 ml ratio. The concentration of the sodium phytate solution was varied from 0.06 mM to 10.8 mM. Due to this mixing and dilution process, the effective concentrations of Ca^{2+} were 0.75 and 4.5 mM, of PO_4^{3-} 0.45 and 2.7 mM, and of sodium phytate 0.03 to 5.4 mM. The final pH of the colloid was between 8 and 9. The particles were studied either as dispersion or after collection on a membrane filter (supra[®]-100 by PALL Life sciences). The filtered nanoparticles were washed with 100 ml of absolute ethanol and dried in air. Ultrapure water (Purelab ultra instrument from ELGA) was used for all preparations.

Hexacalcium phytate (Ca_6PA) was prepared by pumping aqueous solutions of $\text{Ca}(\text{NO}_3)_2 \cdot 4 \text{H}_2\text{O}$ (18 mM, pH = 9.5) and sodium phytate (3 mM, pH = 10.5) into a stirred vessel which led to immediate precipitation. After 30 minutes stirring the precipitate was collected by filtration. The powder was washed with ethanol and dried in air at 37 °C.

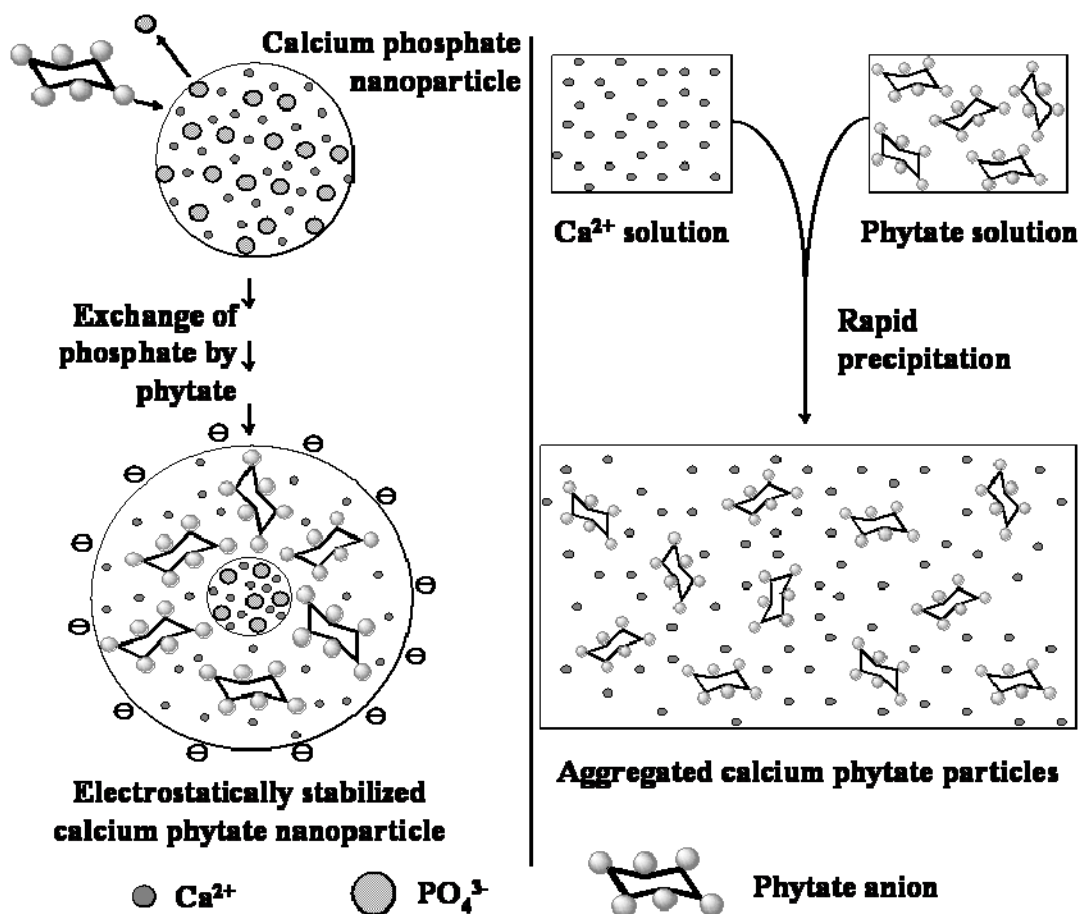


Figure 30: Schematic view of the exchange of phosphate by phytate on the surface of nanoparticles (left hand scheme), preventing the immediate precipitation of calcium phytate (right hand scheme). The colloidal stabilization of the calcium phytate nanoparticles is due to their strongly negative charge.

Calcium phosphate nanoparticles were prepared by rapid precipitation from aqueous solution and rapidly mixed with a solution of sodium phytate. By this procedure, the immediate precipitation of calcium phytate as insoluble salt was prevented, probably by adsorption of negatively charged phytate

anions on the calcium phosphate surface. This led to a strongly negative charge which prevented further agglomeration. The calcium phosphate particles thereby served as template for the precipitation of calcium phytate. The phosphate anions are then exchanged by phytate anions as it will be shown below. The tentative mechanism is depicted in Figure 30.

Stable particles were only obtained in a narrow concentration range of calcium phosphate to sodium phytate (Table 2).

Table 2: Properties of calcium phytate colloids from dynamic light scattering (DLS) and scanning electron microscopy (SEM). In all cases, the effective concentrations in the solution after mixing and dilution are given. Polydispersity index (PDI) value was obtained from DLS measurement.

[Ca ²⁺] / mM	[PO ₄ ³⁻] / mM	[phytate] / mM	[Ca ²⁺] : [phytate]	Particle size from DLS / nm	PDI	Zeta potential / mV	Particle size by SEM / nm
4.5	2.7	0.03	150 : 1	>1000	-	-6 (4)	only agglomerates were found
4.5	2.7	0.3	15 : 1	>1000	-	-22 (4)	
4.5	2.7	0.9	5 : 1	>1000	-	-43 (5)	
4.5	2.7	1.8	2.5 : 1	297	0.193	-52 (6)	ca. 250
0.75	0.45	0.3	2.5 : 1	60	0.209	-56 (6)	ca. 30-40
4.5	2.7	3	1.5 : 1	148	0.144	-52 (10)	ca. 100
4.5	2.7	3.6	1.25 : 1	184	0.120	-50 (10)	very few particles were found
4.5	2.7	4.5	1 : 1	> 500	-	-37 (13)	
4.5	2.7	5.4	0.83 : 1	> 500	-	-43 (5)	

A molar ratio of Ca²⁺ to phytate between 2.5:1 and 1.25:1 gave the best results. If the ratio of calcium to phytate was higher, only agglomerated

nanoparticles which gave a precipitate were found, probably due to insufficient electrostatic stabilization. If it was smaller, only a very small amount of particles was found, probably due to the formation of soluble calcium-phytate complexes. In the optimal range, the particles had the highest negative charge; therefore it was concluded that the nanoparticles were stabilized by electrostatic repulsion. The colloids were stable for about two weeks at room temperature before first signs of sedimentation occurred.

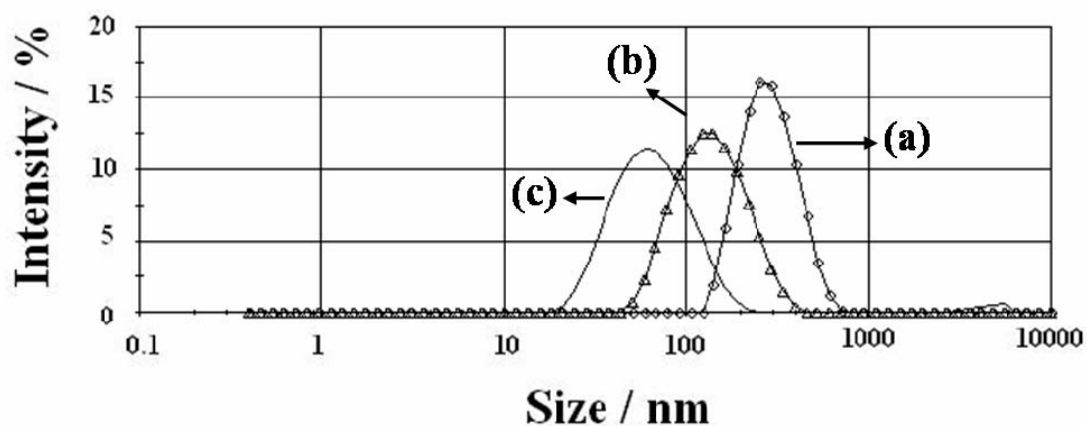


Figure 31: Size distribution data from dynamic light scattering (DLS) of calcium phytate nanoparticles prepared with **(a)** $[\text{Ca}^{2+}] = 4.5 \text{ mM}$ and $[\text{phytate}] = 1.8 \text{ mM}$, **(b)** $[\text{Ca}^{2+}] = 4.5 \text{ mM}$ and $[\text{phytate}] = 3 \text{ mM}$ and **(c)** $[\text{Ca}^{2+}] = 0.75 \text{ mM}$ and $[\text{phytate}] = 0.3 \text{ mM}$.

Figure 31 shows the dynamic light scattering data for the stable colloidal dispersions. Scanning electron microscopy showed the morphology and size of the functionalized calcium phosphate particles (Fig. 32), confirming the data from dynamic light scattering. All particles are approximately spherical and their size is very uniform under a given set of conditions.

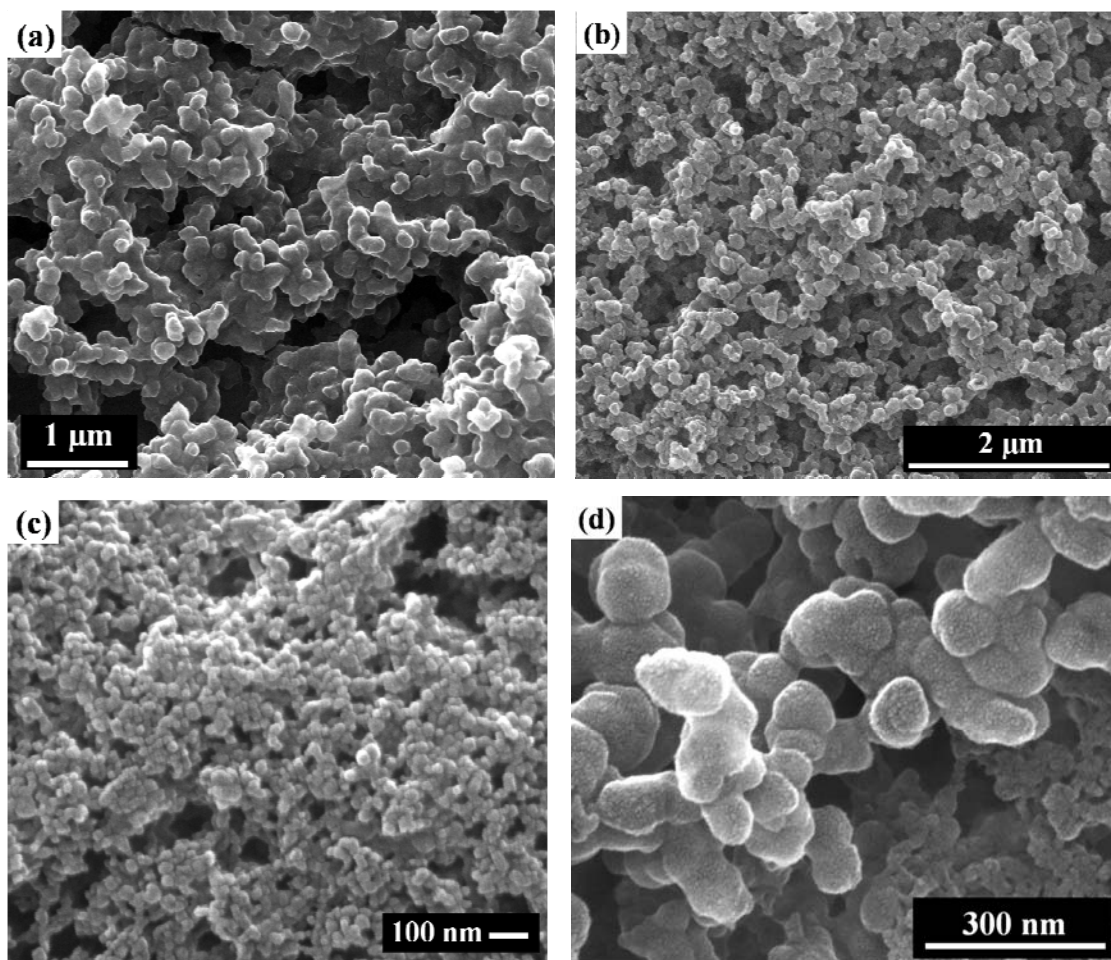


Figure 32: SEM pictures of calcium phytate nanoparticles prepared with (a) $[\text{Ca}^{2+}] = 4.5 \text{ mM}$ and $[\text{phytate}] = 1.8 \text{ mM}$, (b) $[\text{Ca}^{2+}] = 4.5 \text{ mM}$ and $[\text{phytate}] = 3 \text{ mM}$, (c) $[\text{Ca}^{2+}] = 0.75 \text{ mM}$ and $[\text{phytate}] = 0.3 \text{ mM}$, and (d) $[\text{Ca}^{2+}] = 4.5 \text{ mM}$ and $[\text{phytate}] = 0.9 \text{ mM}$ (agglomerated sample).

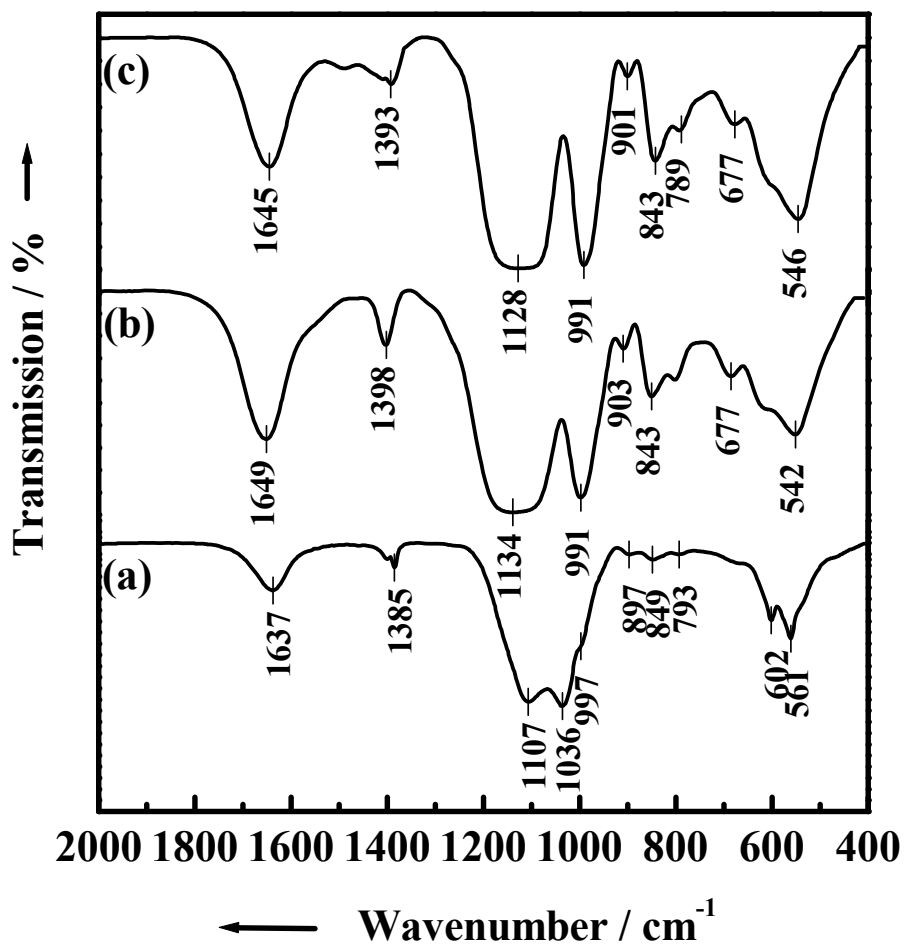


Figure 33: IR spectra of aggregated calcium phosphate particles prepared with $[Ca^{2+}] = 4.5$ mM and $[phytate] = 0.5$ mM (a), of calcium phytate nanoparticles prepared with $[Ca^{2+}] = 4.5$ mM and $[phytate] = 3$ mM, obtained by filtration (b), and of precipitated calcium phytate (c).

Figure 33 shows the IR spectra of functionalized calcium phosphate nanoparticles, isolated calcium phytate nanoparticles and precipitated calcium phytate particles. The characteristic vibrational bands of

hydroxyapatite (1105, 1036, 602, and 563 cm^{-1}) were detected only at a high ratio of Ca^{2+} to phytate ($> 5:1$), i.e. when agglomerates were formed (Table 2). The characteristic vibrational bands of the phytic acid were also observed (997, 897, 849, and 793 cm^{-1}), indicating the presence of adsorbed phytic acid in the agglomerated particles (Fig. 33a).

The IR spectrum of the calcium phytate nanoparticles is shown in Figure 33b which consists of characteristic vibrational bands of calcium phytate (Fig. 33c). The adsorbed water molecules give a weak absorption band around 1645 cm^{-1} (bending) and a broad absorption band around 3400 cm^{-1} (stretching vibration). Two broad bands around 1130 and 542 cm^{-1} are assigned to the PO_4^{2-} group. The bands at 991, 903, 843 and 795 cm^{-1} are assigned to the C-O-P vibrations from the 5ax/1eq conformation of phytate^[234]. The C-O stretching vibration is observed at 1398 cm^{-1} . Compared to precipitated calcium phytate, the small shifts in the vibrational bands of functionalized particles are probably due to different calcium concentrations in the samples.

X-ray powder diffraction showed that the calcium phytate nanoparticles were X-ray amorphous like the precipitated calcium phytate (Fig. 34a and 34b). Only for agglomerated samples with a high Ca^{2+} to phytate ratio ($>5:1$) we observed broad diffraction peaks of hydroxyapatite (Fig. 34c), which indicates the lower crystallinity of the calcium phosphate nanoparticles.

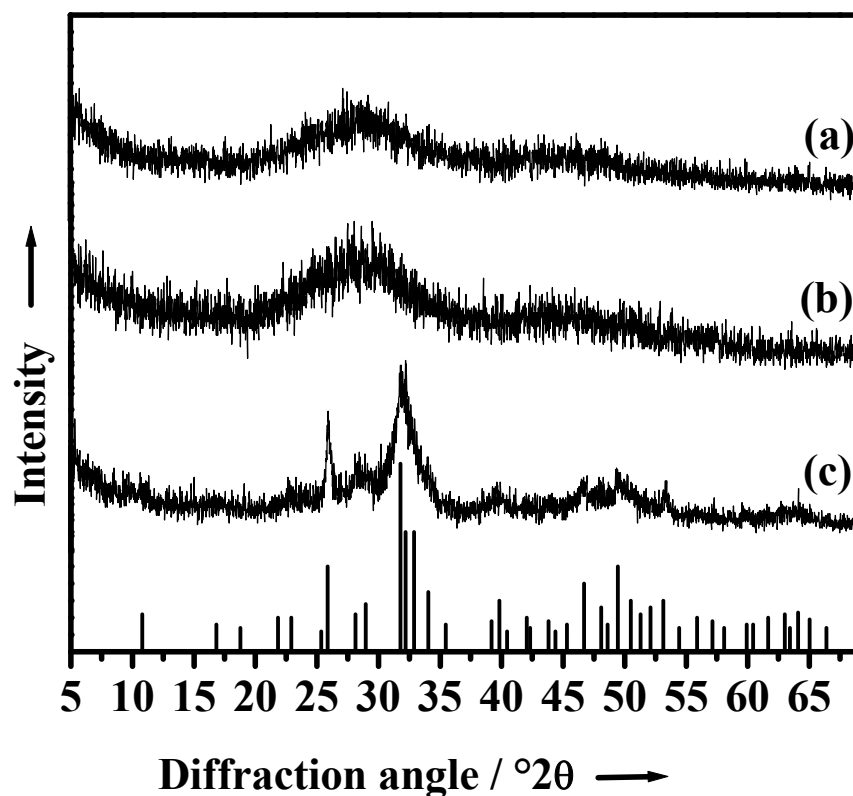


Figure 34: XRD data of calcium phytate nanoparticles prepared with $[Ca^{2+}] = 4.5$ mM and $[phytate] = 3$ mM, obtained by filtration (a), and of precipitated calcium phytate (b). The samples were almost fully amorphous. The XRD spectrum of agglomerated particles obtained with $[Ca^{2+}] = 4.5$ and $[phytate] = 0.5$ mM (c). The broad diffraction peaks indicate the poorly crystalline nature of hydroxyapatite phase. The expected diffraction pattern for hydroxyapatite is shown at the bottom for reference (black line).

Table 3: Elemental analysis data of calcium phosphate/calcium phytate colloids, obtained by filtration and drying in air at 37 °C. CaP = calcium phosphate.

[Ca ²⁺] / mM	[PO ₄ ³⁻] / mM	[phytate] / mM	C / %	H / %	Ca / %	Composition
4.5	2.7	0.05	0.84	1.16	33.55	CaP+Ca ₆ PA+H ₂ O
4.5	2.7	0.5	2.55	1.93	29.38	CaP+Ca ₆ PA+H ₂ O
4.5	2.7	1.5	6.10	2.81	19.75	Ca ₆ PA+H ₂ O
4.5	2.7	3.0	7.13	2.89	21.08	Ca ₆ PA+H ₂ O
0.75	0.45	0.3	6.74	2.65	21.39	Ca ₆ PA+H ₂ O
Precipitated calcium phytate			6.43	3.45	21.26	Ca ₆ PA+H ₂ O
Computed for Ca ₆ PA·13.1 H ₂ O			6.41	2.89	21.39	
Computed for calcium phytate (Ca ₆ PA)			8.11	0.68	27.07	

By elemental analysis, it was confirmed that the particles consist of hexacalcium phytate plus some adhering water (about 21 wt%), except for high ratios of calcium to phytate where calcium phosphate was still present. In these cases, the exchange of phosphate by phytate was not quantitative. Attempts to determine the content of phosphate as molybdate complex gave no satisfactory results, probably because the organic phosphate in the phytate was only partly susceptible to this reaction. The data from elemental analysis were qualitatively confirmed by energy-dispersive X-ray spectrometry in the SEM.

3.2.2. Conclusion

The direct synthesis of calcium phytate by mixing a calcium salt and a phytate salt does not lead to a stable colloid, probably due to aggregation and crystal growth. If calcium phosphate nanoparticles are used as nuclei, the phosphate anion is exchanged by phytate and a stable colloid of calcium phytate can be obtained. However, the ratio of calcium to phytate must be in a narrow range around 1.5:1. If calcium phosphate is present in excess, the particles still contain calcium phosphate and precipitation occurs. If phytate is present in excess, dissolution of the particles occurs, probably by complexation of calcium by phytate ions. These colloids have the major advantage of being fully biocompatible with no stabilizers being necessary.

3.3. Synthesis and characterization of hollow calcium phosphate nanoparticles

Hollow calcium phosphate shells have attracted considerable interest within the last ten years due to their good biodegradability and biocompatibility, their wide application as bioceramics, as an adsorbent for biomaterials and as chemical sensor, catalyst supports, bone-repairing agent, biomedical implants and drug delivery vehicles.^[91, 94, 95, 235] Template-assisted or template-free methods were used to prepare hollow calcium phosphate micro- and nanoparticles. Mostly the hollow calcium phosphate particles are prepared by template-assisted methods, including hard templates (polymeric capsules^[95, 236], polymeric nanotemplates^[94], lithium-calcium-borate glass^[100, 101], plasma-spraying on metallic substrate^[237] and spray pyrolyzing^[238]) and soft templates (aerosol-mediated approach^[105], surfactants and emulsions^[104, 106, 107, 112, 113, 239]).

Bigi et al. reported the template-free self-assembly method to prepare hollow octacalcium phosphate microstructures (spherulite-like structure consist of blade-shaped octacalcium phosphate crystals) using polyaspartate or polyacrylate as additive.^[240, 241]

An easy and convenient template-free method to prepare hollow calcium phosphate nanoparticles is demonstrated in the current study by functionalizing dispersed calcium phosphate nanoparticles with *O*-phospho-L-tyrosine (TyrP).

TyrP has three different functional groups (-NH₂, -COOH, and -OPO₃H₂) which are all unprotected. TyrP is known to increase the activity of protein tyrosine phosphatases and inhibit the epidermal growth factor receptor activity which results in the inhibition of growth of cancer cells.^[188, 190-192]

3.3.1. Synthesis of *O*-phospho-L-tyrosine (TyrP).

Optically pure *O*-phospho-L-tyrosine (TyrP) was prepared according to the reported procedure (Fig. 35).^[242] The isolated compound was characterized by ³¹P-, ¹³C-, ¹H-NMR, IR, elemental analysis, and ESI-MS data.

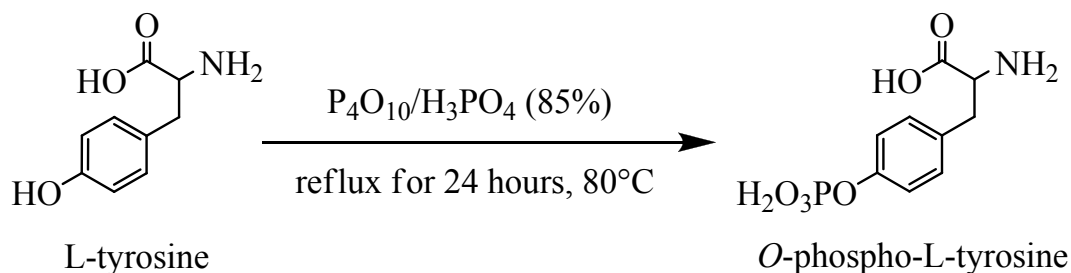


Figure 35: Schematic diagram illustrating the synthesis of *O*-phospho-L-tyrosine (TyrP).

3.3.2. Influence of the concentration of TyrP on the morphology of the calcium phosphate nanoparticles

The calcium phosphate nanoparticles were prepared by simultaneously pumping aqueous solutions of $\text{Ca}(\text{NO}_3)_2 \cdot 4\text{H}_2\text{O}$ (3 mM, pH 9) and $(\text{NH}_4)_2\text{HPO}_4$ (1.8 mM, pH 9) into a stirred vessel. A few seconds after mixing, the nanoparticle dispersion was taken with a syringe. The colloids were prepared by rapidly mixing an aqueous solution of TyrP (pH 9) and the dispersed calcium phosphate nanoparticles in a 5 ml:10 ml ratio. Before preparing the colloids, the solutions of TyrP were filtered through a syringe filter to remove dust particles. The colloid was gently swirled for few seconds. The concentration of TyrP solution was varied from 0.3 to 6 mM. Due to this mixing and dilution process, the effective concentrations were

[Ca²⁺] = 1 mM, [PO₄³⁻] = 0.6 mM, and [TyrP] = 0.1 to 2 mM. The final pH of the colloid was between 7.5 to 8.5. The particles were studied either as dispersion or after collection on a membrane filter (supra[®]-100 by PALL Life sciences). The filtered nanoparticles were washed with 100 ml of absolute ethanol and dried in air. Ultrapure water (Purelab ultra instrument from ELGA) was used for all preparations. The fresh colloids were immediately studied by dynamic light scattering.

Table 4: Properties of calcium phosphate colloids from dynamic light scattering (DLS) and scanning electron microscopy (SEM). In all cases, the effective concentrations in the solution after mixing and dilution are given. The polydispersity index (PDI) was obtained from DLS measurement.

[Ca ²⁺] / mM	[PO ₄ ³⁻] / mM	[TyrP] / mM	[Ca ²⁺] / [TyrP]	Particle size from DLS / nm	PDI	Zeta potential / mV	Morphology; particle size by SEM / nm
1	0.6	0.1	10:1	359	0.176	-9 (4)	Flower-like particles; > 1000
1	0.6	0.3	3:1	255	0.110	-14 (5)	A mixture of spherical and needle-like particles; <i>ca.</i> 250
1	0.6	0.5	2:1	241	0.083	-20 (5)	Hollow spherical particles; <i>ca.</i> 250
1	0.6	0.7	1.43:1	219	0.090	-18 (6)	
1	0.6	1	1:1	237	0.055	-21 (5)	
1	0.6	2	0.5:1	232	0.105	-27 (6)	

All properties of the colloids from dynamic light scattering measurements are shown in Table 4. A stable colloid could be prepared at a low Ca²⁺ to

TyrP ratio ($\leq 1:1$). The zeta potential value was about -20 to -30 mV, indicating the adsorption of negatively charged TyrP on the calcium phosphate surface.

With a high Ca^{2+} to TyrP ratio ($\geq 10:1$), the aggregation of particles occurred within few minutes, probably due to less electrostatic stabilization of the calcium phosphate particles. Figure 36 shows the dynamic light scattering data of TyrP-functionalized calcium phosphate nanoparticles ($\text{Ca}^{2+}:\text{TyrP} = 1:1$). The colloids were stable for three to four hours. When the Ca^{2+} to TyrP ratio was decreased to less than 1, the colloids were stable for about 24 hours at room temperature before first signs of sedimentation occurred.

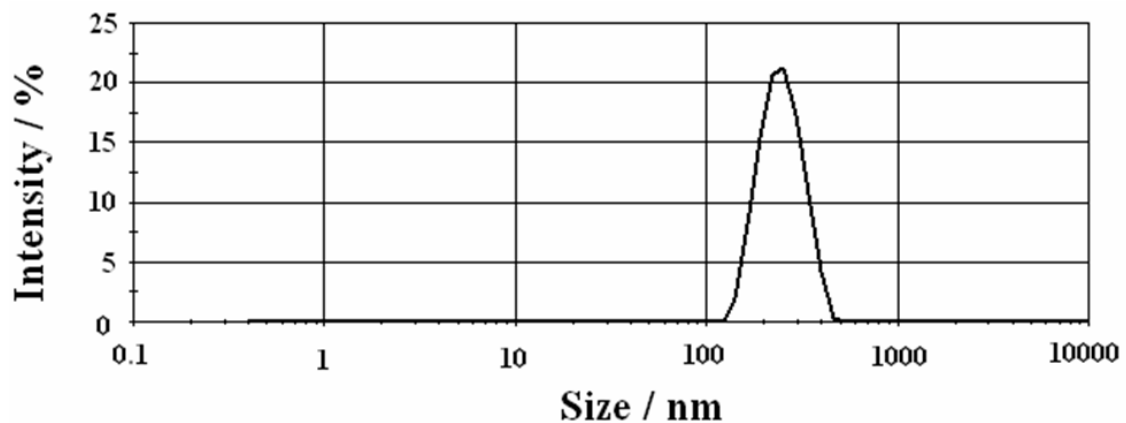


Figure 36: Size distribution data of the TyrP-functionalized calcium phosphate nanoparticles ($\text{Ca}^{2+}:\text{TyrP} = 1:1$) from dynamic light scattering without sonication at pH 8.3.

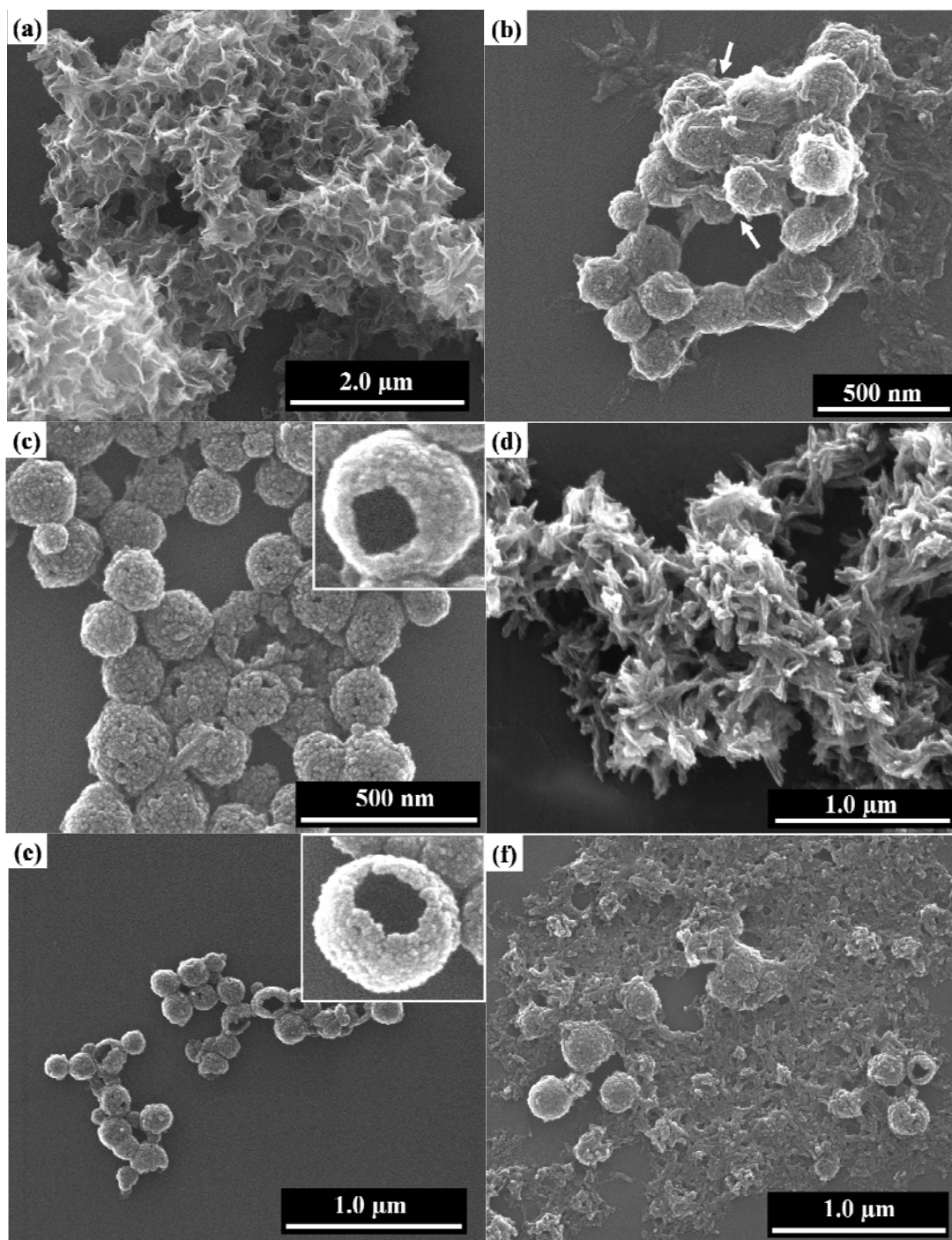


Figure 37: SEM pictures of TyrP-functionalized calcium phosphate nanoparticles prepared with a Ca^{2+} to TyrP ratio of (a) 10:1, (b) 3:1 (the arrows indicate the aggregation of needle-like particles), (c) 2:1, (d) 2:1 after 60 minutes sonication, (e) 1:1 and (f) 1:1 after 60 minutes sonication.

Scanning electron microscopy shows the morphology and size of the TyrP-functionalized calcium phosphate particles (Fig. 37). With high Ca^{2+} to TyrP ratio ($\geq 10:1$), the aggregated flower-like microparticles were observed (Fig. 37a). At the Ca^{2+} to TyrP ratio of 3:1, a mixture of spherical and needle-like particles was observed. From the detailed analysis of the SEM picture (Fig. 37b), the spherical particles could be formed by the aggregation of needle-like particles. By lowering the Ca^{2+} to TyrP ratio ($\leq 2:1$), only the hollow spherical nanoparticles were observed, in which the monolayer of the calcium phosphate shell consisted of 20 to 30 nm primary nanoparticles (Fig. 37c and 37e). The SEM results were in good agreement with the dynamic light scattering data.

The stability of hollow nanoparticles was checked by continuous ultrasonication (35 Hz, 160 W, Bandelin Sonorex[®] RK510). The fresh colloids were sonicated for 60 minutes. The final temperature of the water in the ultrasonic bath was between 45 to 55°C. When the Ca^{2+} to TyrP ratio was 2:1, the hollow spherical particles were transformed to aggregated needle-like particles (Fig. 37d). In the case of lower Ca^{2+} to TyrP ratio (1:1), most of the hollow spherical particles were broken and primary calcium phosphate nanoparticles (20-30 nm) were formed (Fig. 37f). Some hollow spherical particles were still found. This shows that the hollow particles are stable at room temperature (without any mechanical agitation), when the Ca^{2+} to TyrP ratio is ≤ 2 . It also displays that the formation of hollow nanoparticles is highly influenced by the amount of TyrP used to functionalize the calcium phosphate nanoparticles.

The isolated hollow particles were calcined at 600°C in air for 10 minutes and cooled to room temperature. The calcined particles were analyzed

through SEM which showed that the hollow spherical particles were stable during calcination (see Fig. 38).

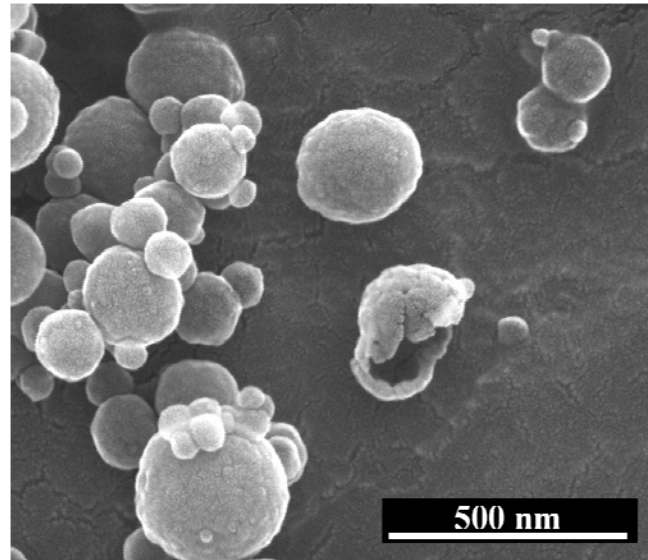


Figure 38: SEM picture of hollow spherical particles after calcination ($\text{Ca}^{2+}:\text{TyrP} = 1:1$).

X-ray powder diffraction data of TyrP-functionalized calcium phosphate nanoparticles are shown in Figure 39. Figures 39a, 39c and 39d show two broad diffraction peaks, indicating the amorphous internal structure of the samples. The diffraction peaks of hydroxyapatite were observed only at higher Ca^{2+} to TyrP ratio (2:1), when the nanoparticles were collected after 60 minutes sonication. The width of the diffraction peaks indicates the poorly or moderately crystalline phase of hydroxyapatite (Fig. 39b). Comparing these XRD data with SEM pictures (Fig. 37c, 37d, 37e and 37f), the hollow spherical particles are X-ray amorphous and the aggregated needle-like particles are poorly crystalline hydroxyapatite.

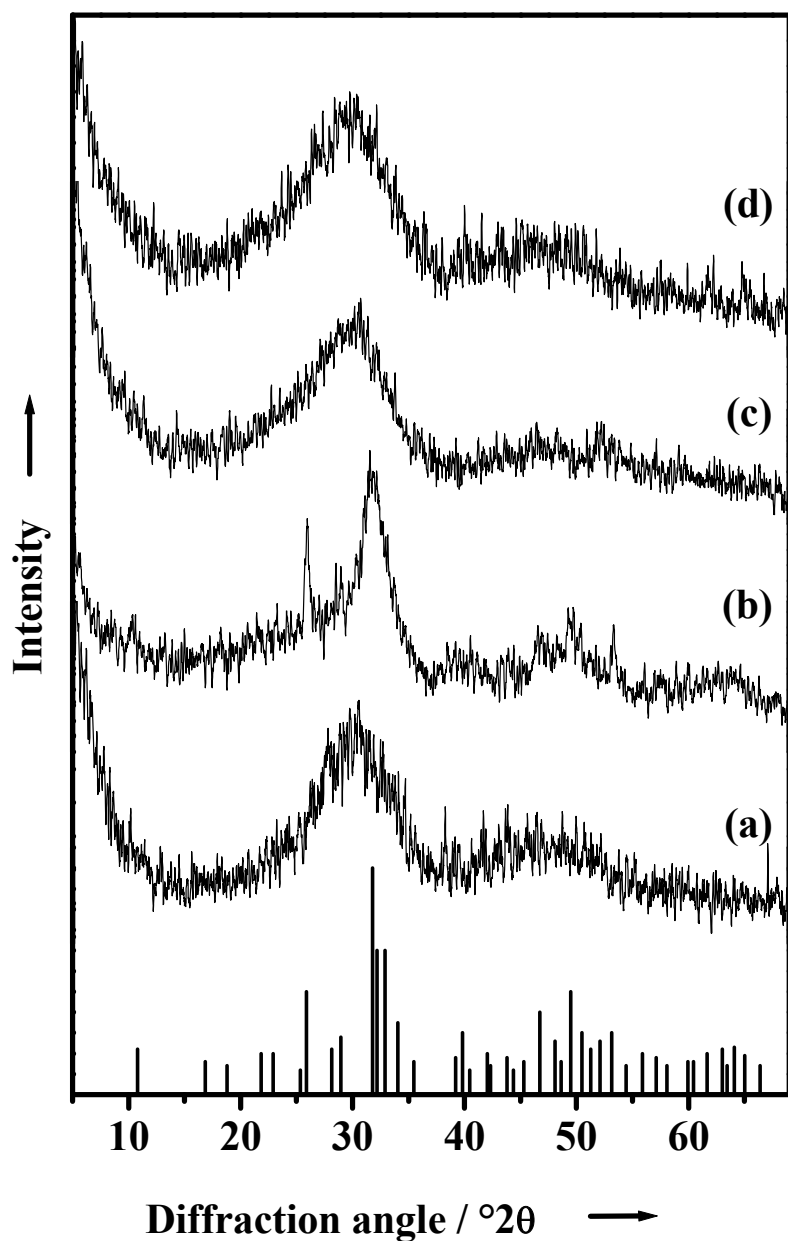


Figure 39: XRD data of the hollow calcium phosphate nanoparticles prepared with a Ca²⁺ to TyrP ratio of (a) 2:1, (b) 2:1 after 60 min sonication, (c) 1:1 and (d) 1:1 after 60 minutes sonication. The expected diffraction pattern for hydroxyapatite is shown at the bottom for reference (black line).

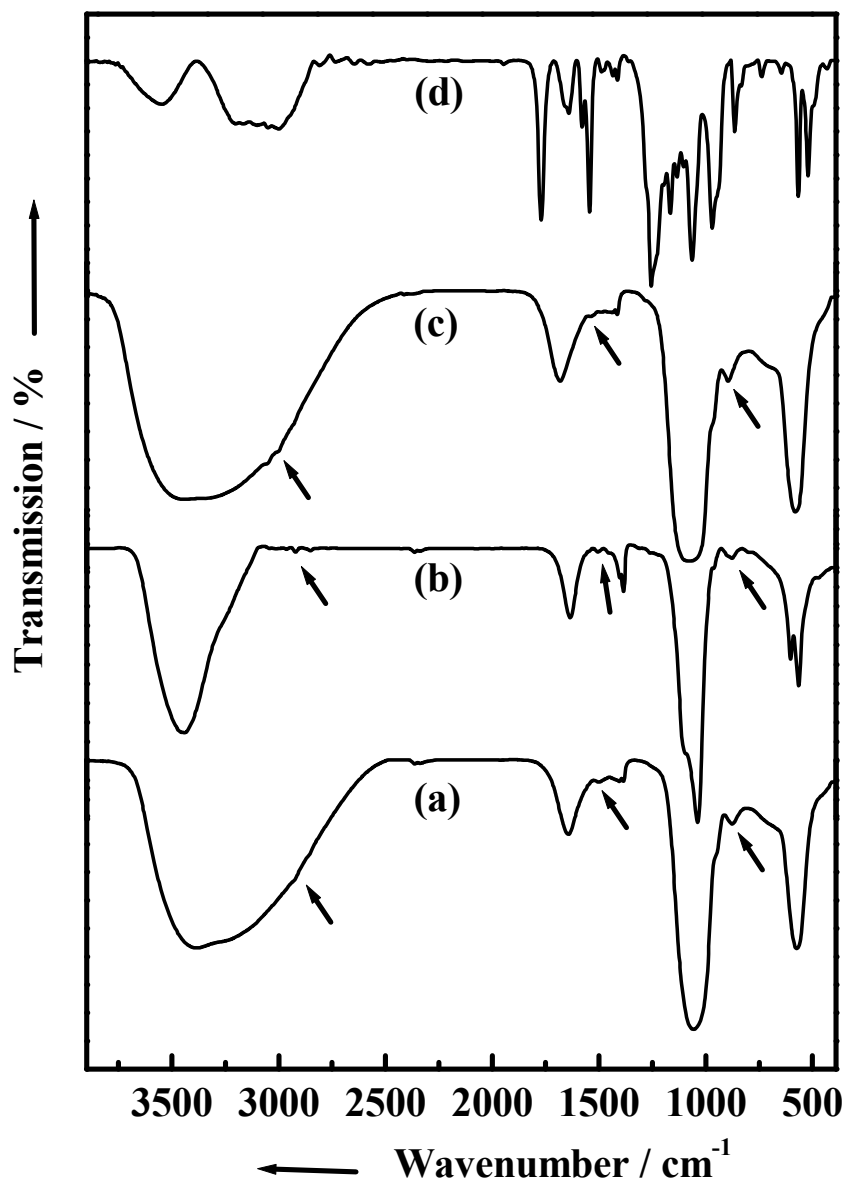


Figure 40: IR data of the functionalized calcium phosphate nanoparticles prepared with $[\text{Ca}^{2+}]/[\text{TyrP}]$ of (a) 2:1 (hollow spherical particles), (b) 2:1 after 60 min sonication (needle-like particles) and (c) 1:1 (hollow spherical

particles). The arrows indicate the weak absorption bands of TyrP. (d) IR spectrum of TyrP for reference.

In Figure 40, IR data of TyrP-functionalized calcium phosphate nanoparticles and TyrP are compared. The adsorbed water molecules gave a weak absorption band around 1645 cm^{-1} (bending) and a broad absorption band around 3400 cm^{-1} (stretching vibration). The weak C-O bending vibration of carbonate group was observed at 1385 cm^{-1} . Figure 40a and 40c show two broad vibrational bands at 1057 cm^{-1} and 577 cm^{-1} which are assigned to the PO_4^{3-} group in calcium phosphate. The characteristic vibrational bands of hydroxyapatite (1038 , 604 , and 565 cm^{-1}) were observed only for the sample collected after 60 minutes sonication ($\text{Ca}^{2+}/\text{TyrP} = 2:1$) (Fig. 40b). The very weak vibrational bands of TyrP were also observed at 2982 cm^{-1} , 2853 cm^{-1} , 1504 cm^{-1} and 876 cm^{-1} , confirming that the calcium phosphate surface is functionalized by TyrP.

Table 5 shows the elemental analysis data of TyrP-functionalized calcium phosphate nanoparticles. The content of TyrP in the nanoparticles was estimated as follows: The hollow nanoparticles consist of about 74-83% of calcium phosphate. About 18 % of water molecules could be adhered in the amorphous sample. It is concluded that the effective loading of TyrP in the solid is around 3-6 wt%, if we assume that all calcium and phosphate did precipitate as hydroxyapatite, $\text{Ca}_5(\text{PO}_4)_3\text{OH}$. Therefore, an excess amount of TyrP is present in solution which influences the formation of hollow calcium phosphate nanoparticles.

The porosity of the hollow particles was about 0.4 to 0.5, which was computed from the ratio of the volume of void space in the material and the volume of the total or bulk material.

Table 5: Elemental analysis data of TyrP-functionalized calcium phosphate nanoparticles, obtained by filtration and drying in air at 37 °C.

[Ca ²⁺] / mM	[PO ₄ ³⁻] / mM	[TyrP] / mM	Sonication (min)	C / %	H / %	Ca / %	¹ Percentage of TyrP	² Percentage of calcium phosphate	³ Percentage of water
1	0.6	0.5	-	1.32	1.99	-	3.19	-	16.5
1	0.6	0.5	60	2.48	1.27	33.1	5.99	83.1	8.8
1	0.6	1	-	0.92	2.16	29.54	2.22	74.2	18.4

¹Computed from the amount of carbon by the ratio of the molar masses of carbon and TyrP.

²Computed from the amount of calcium by the ratio of the molar masses of calcium and hydroxyapatite.

³Computed from the amount of hydrogen by the ratio of the molar masses of hydrogen and water.

3.3.3. Conclusion

A template-free method of preparation of hollow calcium phosphate nanoparticles was described. The method is simple and efficient and the hollow particles are easily prepared by mixing the dispersed calcium phosphate nanoparticles with TyrP. The zeta potential values indicate the adsorption of TyrP on the calcium phosphate surface. SEM measurements showed hollow spherical nanoparticles with a size of *ca.* 250 nm which was supported by dynamic light scattering data. The size and hollow spherical structure of the particles were unaffected by increasing the concentration of calcium to TyrP ratio to more than 2:1. The hollow spherical particles are composed of a thin shell of primary calcium phosphate nanoparticles. The thickness of the shell is about *ca.* 20-30 nm. The presence of hollow spherical particles was confirmed by calcining the isolated hollow particles at 600°C. By comparing the SEM and XRD data, it was concluded that the hollow spherical structures consist of amorphous particles. Although a higher concentration of TyrP ($[Ca^{2+}]/[TyrP] = 1$) was used to functionalize the calcium phosphate particles, only very weak vibrational bands were observed in IR spectroscopy of the TyrP-functionalized calcium phosphate particles. The effective concentration of TyrP in the solid calcium phosphate particles was around 3-6%.

Therefore, the amount of free TyrP present in solution plays a critical role in the formation of hollow structures. The surface adsorbed TyrP molecules may have free functional groups, most probably $-NH_2$ or $-COOH$ groups. The presence of an excess amount of TyrP in solution could have weak interactions (like hydrogen bonding) with surface adsorbed TyrP molecules which results in the self-assembly of primary calcium phosphate particles

(*ca.* 20-30 nm) into hollow spherical particles (*ca.* 250 nm). By sonication of the colloids, the weak hydrogen bonding can be broken and the hollow spherical nanoparticles can be transformed into needle-like particles. These biocompatible TyrP-functionalized calcium phosphate nanoparticles may be useful in drug delivery systems.

3.4. Functionalization of calcium phosphate nanoparticles with alkyl phosphates

In the current study, calcium phosphate nanoparticles were functionalized with alkyl phosphates (surfactants) which have phosphate as head group and alkyl chains as tail groups. Alkyl phosphates were varied in their length of the alkyl chain or the spacer groups attached with them. In two surfactants, namely dodecyloxyphenyl phosphate and dodecyloxybiphenyl phosphate, aryl groups were used as spacer groups between head and tail groups.

3.4.1. Represented alkyl phosphates

The alkyl phosphates shown in Figure 41 were synthesized, characterized and used to functionalize the calcium phosphate surface.

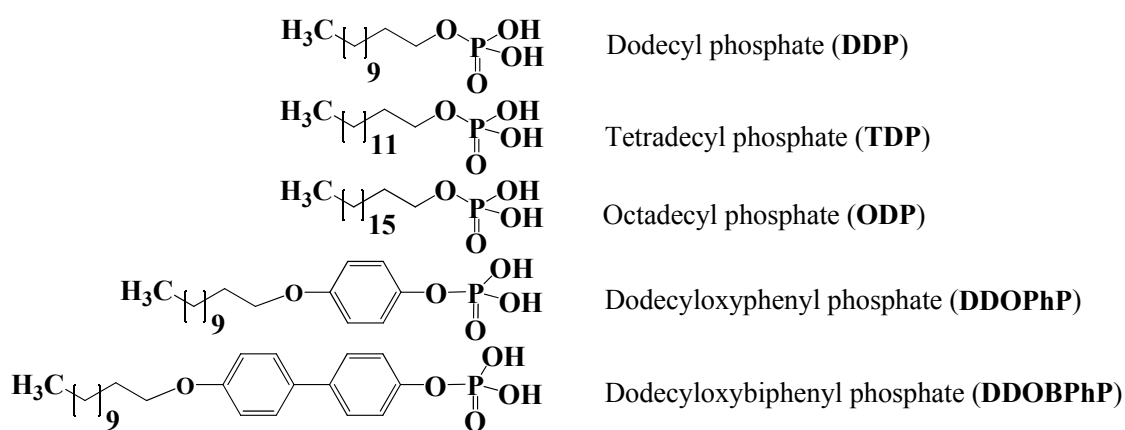


Figure 41: Chemical structure, name and abbreviation of alkyl phosphates which were used to functionalize the calcium phosphate particles.

3.4.2. Synthesis of alkyl phosphates

Okamoto et al. reported an easy and convenient method to prepare monoalkyl dihydrogen phosphates by treating the alcohols with trimethylsilyl polyphosphate (Fig. 42).^[243] In the present study, DDP, TDP and ODP were prepared according to this procedure. Trimethylsilyl polyphosphate is prepared by refluxing a benzene solution of diphosphorus pentoxide and hexamethyldisiloxane. The reaction proceeds smoothly with a high yield of monoalkyl dihydrogen phosphate and only trace amounts of dialkyl hydrogen phosphate.

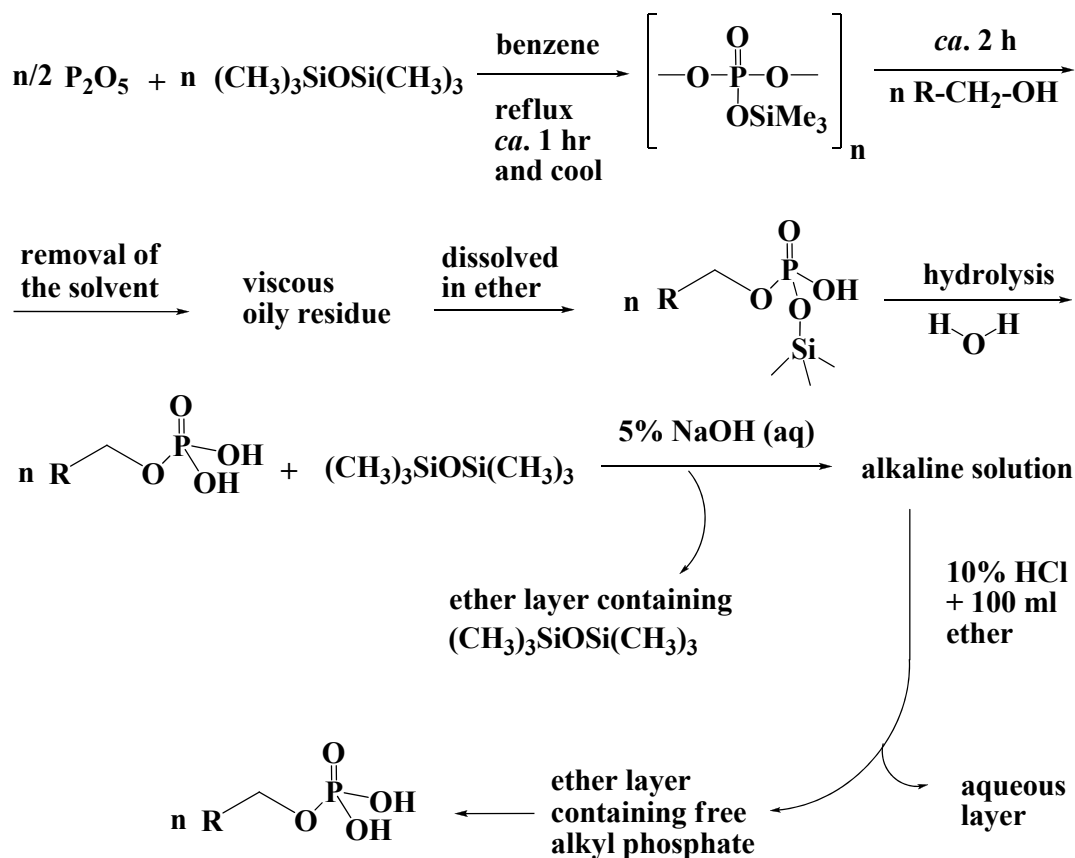


Figure 42: Schematic diagram illustrating the preparation of DDP, TDP and ODP.

The above procedure was tried to prepare DDOPhP and DDOBPhP but the reactions were not successful. Therefore the corresponding alcohol groups were directly treated with POCl₃ in the presence of triethylamine or pyridine as base (Fig. 43). The products were recrystallized in hot n-hexane. The yield was very poor for DDOPhP and DDOBPhP compared to DDP, TDP and ODP.

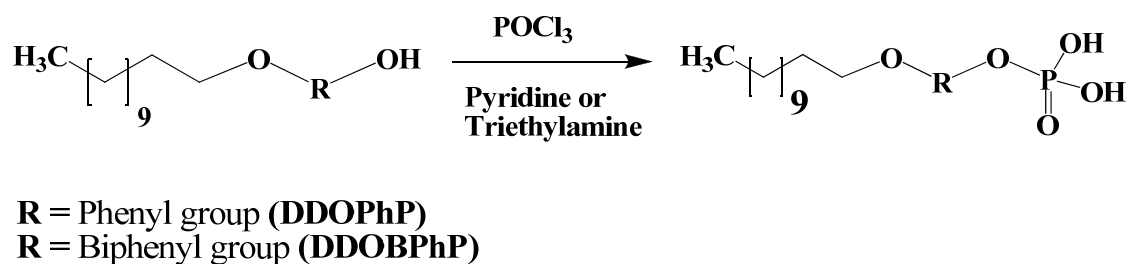


Figure 43: Schematic diagram illustrating the preparation of DDOPhP and DDOBPhP.

3.4.3. Optimizing the concentrations of alkyl phosphates to functionalize the calcium phosphate surface

The calcium phosphate nanoparticles were prepared by pumping aqueous solutions of Ca(NO₃)₂·4 H₂O (3 mM, pH 9.5) and (NH₄)₂HPO₄ (1.8 mM, pH 10) into a stirred vessel. A few seconds after mixing, the nanoparticles dispersion was taken with a syringe. The colloids were prepared by rapidly mixing an aqueous solution of the sodium salt of alkyl phosphates and the dispersed calcium phosphate nanoparticles in a 10 ml:10 ml ratio. The concentration of the sodium salt of the alkyl phosphate solution was varied from 25 μM to 100 μM. After mixing of the alkyl phosphate with the calcium phosphate nanoparticle dispersion, the colloid was immediately

studied by the dynamic light scattering (DLS) measurement. The polydispersity index (PDI) value (<0.3) was used to confirm the monodisperse behaviour of colloidal systems.

In the case of the sodium salt of TDP ($25 \mu\text{M}$), the size distribution data from DLS showed an average particle size of about 650 nm with a PDI value of 0.124 (Fig. 44). The adsorption of the sodium salt of TDP reduced the zeta potential to -33 mV (Table 2), which indicates the good adsorption of TDP phosphate head groups on the calcium phosphate surface.

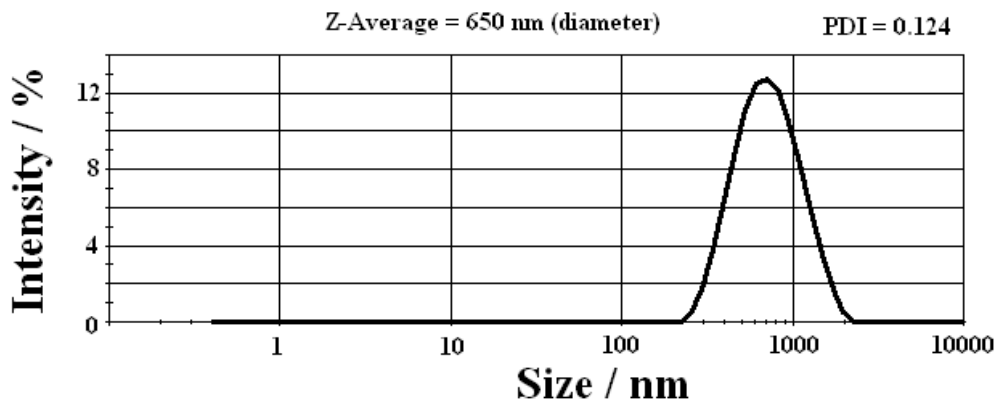


Figure 44: Size distribution data of calcium phosphate nanoparticles functionalized with $25 \mu\text{M}$ of the sodium salt of TDP at pH 8 from dynamic light scattering.

The aggregation behavior of the colloidal particles was studied by DLS measurement (Fig. 45). The particles aggregated slowly with time. The size of the particle grew from 650 nm to more than $1 \mu\text{m}$, and the PDI value was almost 0.3. The colloid was stable only for three hours at room temperature before first signs of sedimentation occurred.

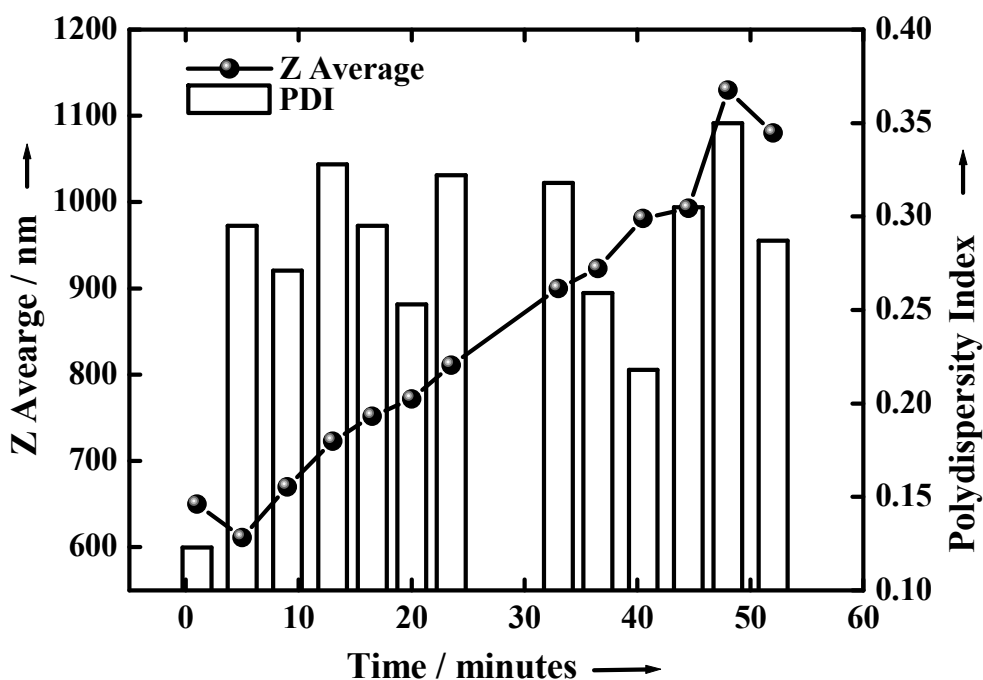


Figure 45: Aggregation behavior of the colloidal particles in the case of TDP at pH 8.

By increasing the TDP concentration to 50 μM , the average size of the particles was reduced to 531 nm but the PDI value was greater than 0.3. This indicated that the particles were not monodisperse. A further increase in the concentration of TDP to more than 50 μM resulted in immediate flocculation.

Scanning electron microscopy (SEM) was performed to obtain a direct view on the nanoparticles (Fig. 46). In the case of the colloid with the addition of 25 μM and 50 μM of TDP, the SEM picture showed flower-like aggregated micro particles. By increasing the concentration to more than 50 μM , rod-

like particles were observed. The length of the rod-like particles was about 1 to 2 μm and the diameter was about 100 to 200 nm.

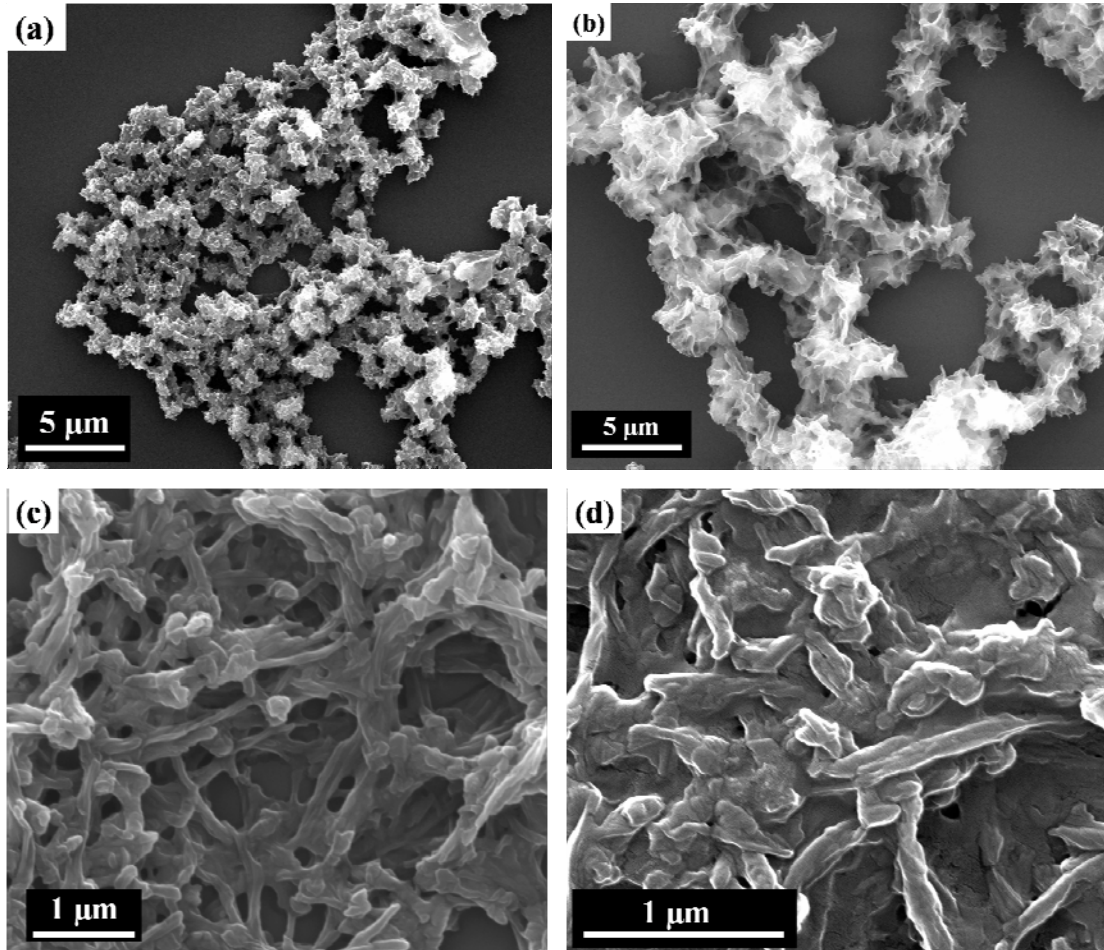


Figure 46: SEM picture of calcium phosphate particles functionalized by the addition of (a) 25 μM , (b) 50 μM , (c) 75 μM and (d) 100 μM of the sodium salt of TDP.

3.4.4. Comparison of the sodium salt of TDP with other surfactants or alkyl phosphates in functionalizing the calcium phosphate surface

The dynamic light scattering data and SEM results of TDP-functionalized calcium phosphate particles were compared with the data of other alkyl phosphate-functionalized calcium phosphate particles (Table 6).

Table 6: Properties of calcium phosphate colloids from dynamic light scattering (DLS) and scanning electron microscopy (SEM). In all the cases, the concentrations of alkyl phosphates were 25 μ M.

Alkyl phosphates (25 μ M)	Particle size from DLS / nm	PDI	Zeta potential (standard deviation) / mV	Morphology; particle size by SEM / nm
TDP	650	0.124	-33 (5)	Flower-like particles; <i>ca.</i> 1000
DDP	639	0.293	-22 (9)	Needle-like particles; Length <i>ca.</i> 200-250 and width <i>ca.</i> 10-15
ODP	993	0.378	-14 (4)	Flower-like particles; <i>ca.</i> 1000
DDOPhP	695	0.394	-22 (5)	
DDOBPhP	1570	0.555	-6 (4)	

In the case of DDP and DDOPhP, the colloids initially showed a particle size of about 600 to 700 nm in DLS, and then the particles aggregated slowly with time to microparticles. The colloids were stable for only three hours after that the particles were flocculated. In the cases of ODP and DDOBPhP, only the microparticles were observed in DLS and the colloids were flocculated from the solution after few minutes.

The unfunctionalized calcium phosphate particles had a slightly positive zeta potential of about +1.2 mV at a pH of 8.0.^[18] In all cases, the adsorption of alkyl phosphates reduced the zeta potential to negative values, which indicates the adsorption of negatively charged alkyl phosphates on the calcium phosphate surface. The particles functionalized with the alkyl phosphates TDP, DDP and DDOPhP which are less hydrophobic show highly negative zeta potential values (-22...-33 mV). But the alkyl phosphates, ODP and DDOBPhP, which have either a long alkyl chain or a bulkier spacer group, show slightly negative zeta potential (-6...-14mV). The DLS data show that the alkyl phosphates which are less hydrophobic have a higher solubility in aqueous medium and have a higher affinity to bind with calcium ions. This stabilizes the particles for a few minutes.

SEM pictures of the functionalized calcium phosphate particles with the addition of 25 μ M of different types of alkyl phosphates (DDP, TDP, ODP, DDOPhP, and DDOBPhP) are shown in Figure 47. In the case of DDP, the SEM picture shows needle-like aggregated particles. The individual needle-like particle has a length of 200 to 250 nm and a width of 10 to 15 nm. Unlike DDP, the SEM pictures of other alkyl phosphates-functionalized calcium phosphate particles show only flower-like particles with a size of about 1000 nm.

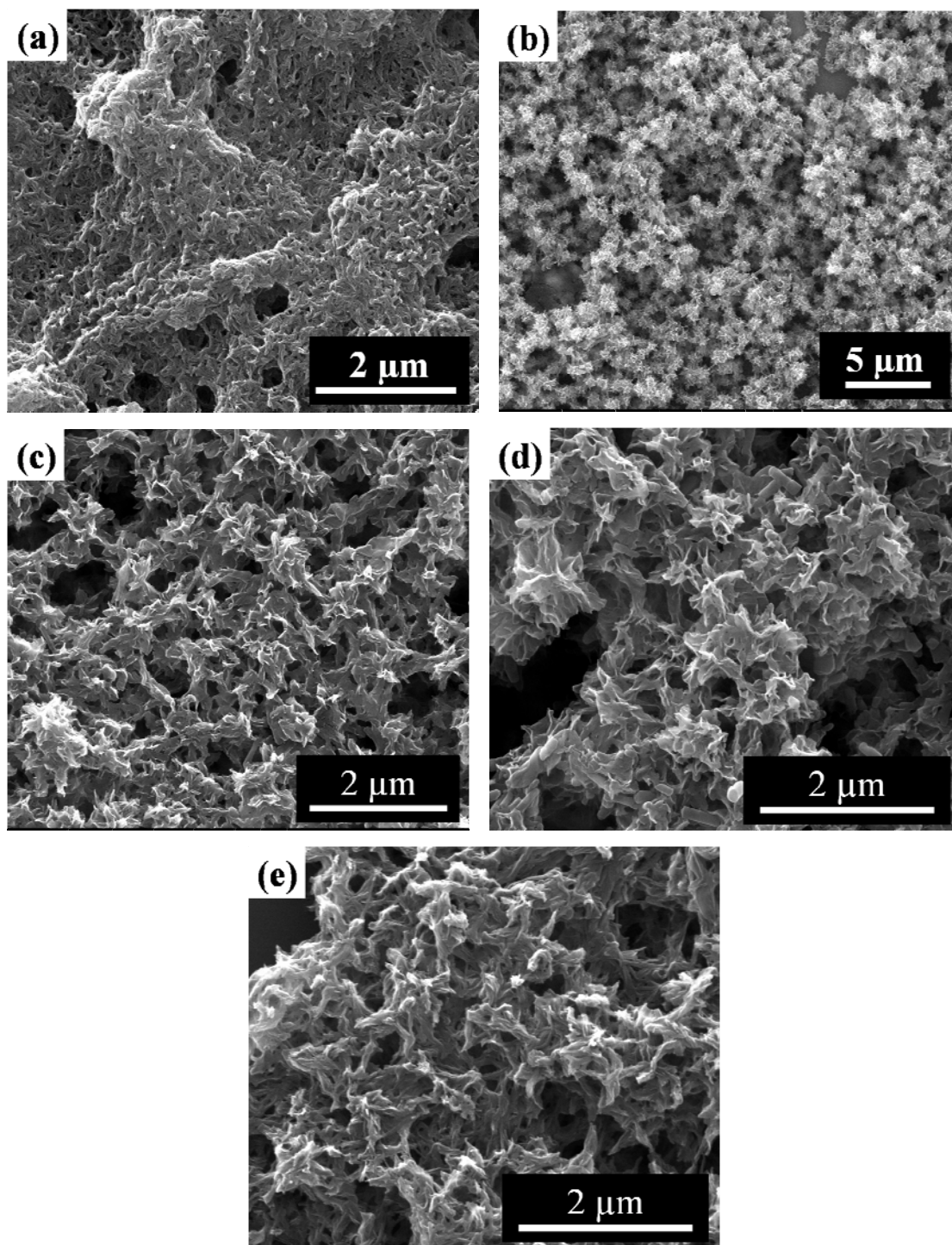


Figure 47: SEM picture of functionalized calcium phosphate particles with the addition of 25 μM of (a) DDP, (b) TDP, (c) ODP, (d) DDOPhP, and (e) DDOBPhP.

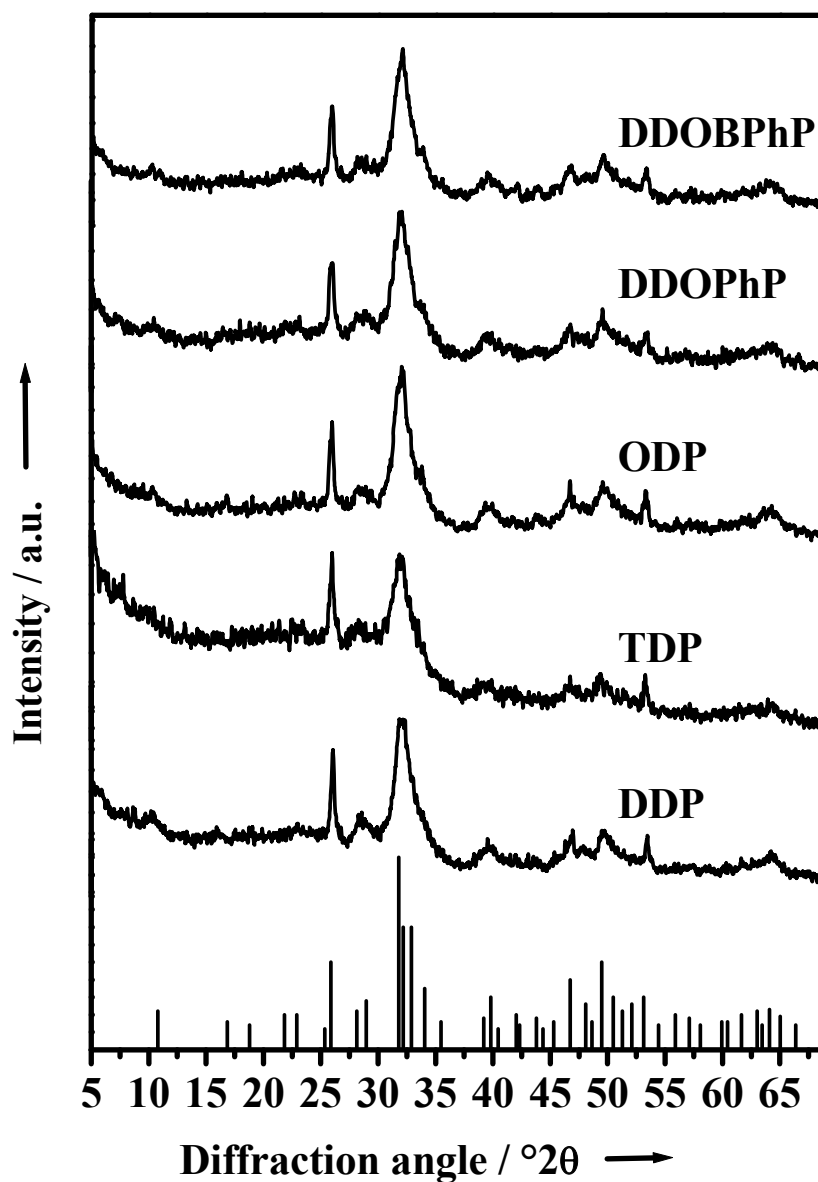


Figure 48: XRD data of alkyl phosphate-functionalized calcium phosphate particles. The width of the diffraction peaks of the functionalized calcium phosphate particles indicates a low crystallinity of the hydroxyapatite phase. The expected diffraction pattern for hydroxyapatite is shown at the bottom for comparison (black line).

The X-ray powder diffraction patterns of the five precipitates are shown in Figure 48. These X-ray data reveal that the precipitates produced by functionalization of the calcium phosphate nanoparticles with each of the five compounds, DDP, TDP, ODP, DDOPhP, and DDOBPhP, consist of poorly or moderately crystalline hydroxyapatite.

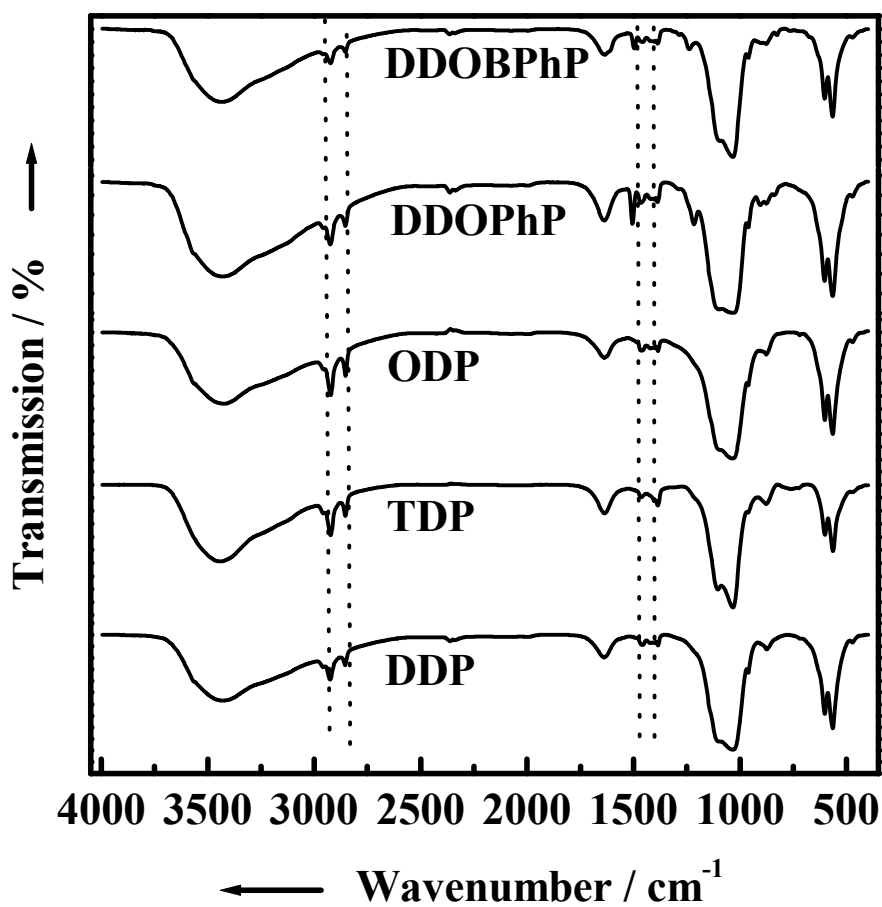


Figure 49: IR spectra of alkyl phosphate-functionalized calcium phosphate particles. The vertical dotted lines correspond to the bands of the alkyl phosphates.

Figure 49 shows the IR spectra of calcium phosphate particles functionalized with different types of alkyl phosphates (DDP, TDP, ODP, DDOPhP, and DDOBPhP). The ν_4 PO_4^{3-} bending mode at 550 cm^{-1} and the ν_1, ν_3 PO_4^{3-} stretching mode at about 1000 cm^{-1} appeared in the IR spectra for all samples. The anisotropic local electrical field of the crystalline phase causes an absorption in the form of an apparent doublet (602 and 565 cm^{-1}). The C-H, C-C, and C=C-H stretching vibrations from alkyl phosphates were also observed at $2922, 2853, 1506, 1464$ and 1385 cm^{-1} in the functionalized nanoparticles. Thus, the IR results confirmed the presence of alkyl phosphates and calcium phosphate.

Table 7 shows the elemental analysis data of alkyl phosphate-functionalized calcium phosphate nanoparticles. The content of alkyl phosphate in the isolated particles was estimated as follows: The amount of alkyl phosphate used to functionalize the calcium phosphate particles was about 1-2 wt%. In the case of DDP, it was 1.1 wt%. If we assume that all the calcium and phosphate are present as hydroxyapatite, $\text{Ca}_5(\text{PO}_4)_3\text{OH}$, elemental analysis of the DDP-functionalized particles by combustion elemental analysis gave about 10 wt% of DDP in the solid. About 9 wt% of excess amount of DDP was observed in the solid sample.

In the same way, the excess amounts of alkyl phosphates were observed for all alkyl phosphate-functionalized the calcium phosphate particles.

Table 7: Elemental analysis data of alkyl phosphate-functionalized calcium phosphate particles, obtained by filtration and drying in air at 37 °C. CaP = calcium phosphate [Ca₅(PO₄)₃OH].

25 μM of Alkyl phosphate ¹	[Ca ²⁺]/mM	[PO ₄ ³⁻]/mM	C / %	H / %	Ca / %	Inorganic phosphate, PO ₄ ³⁻ / %	² Percentage of alkyl phosphate	Composition
TDP / 1.21 wt%	3	1.8	10.18	2.89	31.33	49.10	17.8	CaP + CaTDP + H ₂ O
DDP / 1.10 wt%	3	1.8	5.39	1.80	34.98	43.55	10.0	CaP + CaDDP + H ₂ O
ODP / 1.43 wt%	3	1.8	19.96	6.37	23.82	29.90	32.4	CaP + CaODP + H ₂ O
DDOPhP / 1.46 wt%	3	1.8	6.80	1.82	32.32	46.60	11.3	CaP + CaDDOPhP + H ₂ O
DDOBPhP / 1.77 wt%	3	1.8	6.94	1.68	33.21	42.23	10.5	CaP + CaDDOBPhP + H ₂ O

¹Computed with respect to the amount of hydroxyapatite. It was assumed that all the calcium and phosphate precipitated as hydroxyapatite, Ca₅(PO₄)₃OH.

²Computed from the amount of carbon by the ratio of the molar masses of carbon and alkyl phosphate.

3.4.5. Conclusions

We have prepared alkyl phosphate-functionalized calcium phosphate particles and characterized. About 1-2 wt% of alkyl phosphates were used to functionalize the calcium phosphate nanoparticles with respect to the amount of hydroxyapatite expected to be formed in colloids. The experimental results show that the alkyl phosphates have a very good attachment to the calcium phosphate surface.

Although the surface charge of particles was negative, the presence of hydrophobic alkyl chains destabilized the dispersion of nanoparticles in the aqueous medium. The alkyl phosphates having less hydrophobic alkyl chains showed higher stability of the colloids for two to three hours, whereas the colloids prepared with alkyl phosphates which are highly hydrophobic, flocculated immediately. The length of the alkyl chain influenced the morphology of the calcium phosphate particles. SEM measurements showed needle-like particles in the case of DDP. Other alkyl phosphates showed only flower-like aggregated microparticles. The XRD data showed the poor crystallinity of the particles, and the presence of alkyl phosphates on the precipitated calcium phosphate particles was confirmed by the IR measurement.

It was confirmed by elemental analysis that the content of alkyl phosphate in the precipitated particles were found to be in excess than used. It indicated that the alkyl phosphates adsorbed on the surface of calcium phosphate may have reacted and exchanged inorganic phosphates from the particles. As a result, the calcium salt of alkyl phosphates could be formed and precipitated with hydroxyapatite particles.

From the results it was concluded that the alkyl phosphates can have a high chemical affinity to bind with the calcium phosphate surface and form a hydrophobic layer on hydroxyapatite particles. Therefore, the particles aggregated in solution and precipitated.

4. Materials and methods

4.1. Experimental procedures

4.1.1 Used chemicals

Chemical name	Chemical company
5,10,15,20-tetrakis(4-hydroxyphenyl)porphine	Aldrich
1H-tetrazole (≈ 0.45 M in CH_3CN)	Fluka
<i>m</i> -chloroperbenzoic acid (Assay 70%)	Aldrich
Dodecasodium salt of phytic acid	Aldrich
L-tyrosine	Fluka
Phosphorus oxychloride	Riedel-de Haen
Orthophosphoric acid (85%)	Acros organics
Phosphorus pentoxide	Riedel-de Haen
Phosphorus trichloride	Fluka
N,N-diethylamine	Merck
Triethylamine	Fluka
Pyridine	Bernd Kraft GMBH
Hexamethyldisiloxane	Fluka
1-butanol	Merck
1-doceanol	Aldrich
1-tetradecanol	ABCR
1-octadecanol	ABCR
Hydroquinone	Riedel-de Haen
4,4'-dihydroxybiphenyl	Fluka
1-dodecyl bromide	Aldrich
CDCl_3	Aldrich
D_2O	Aldrich

The chemicals mentioned above were used without further purification. All the experiments were performed under nitrogen atmosphere in oven-dried glassware following the standard schlenk techniques. Solvents used as reaction media were distilled immediately before use. Benzene, diethylether, n-hexane and 1,4-dioxane were dried over sodium/benzophenone. N,N-

diethylformamide was dried over activated molecular sieves. Dichloromethane was dried over calcium hydride. Pyridine, N,N-diethylamine and triethylamine were dried over KOH. Ethanol and methanol were reagent grade solvents.

4.1.2. Preparation of N,N-diethylphosphoramidous dichloride

The compound was prepared according to the procedure.^[219] Diethylamine (73 g, 1 mmol) in dry diethyl ether (100 ml) was added drop wise to a vigorously stirred solution of PCl₃ (68.75 g, 0.5 mmol) in dry diethyl ether (250 ml). The reaction temperature was kept below 0 °C (liquid nitrogen/acetone). On completion of addition, the mixture was stirred for 3 hours at room temperature. The mixture was then filtered through G4 frit and washed with 100 ml of dry ether. Evaporation of the combined diethyl ether solutions under reduced pressure followed by distillation of the crude liquid residual under vacuum gave a clear liquid. The yield was 76.5 g (87.5 %).

³¹P-NMR (CDCl₃): δ = 170 ppm (s).

4.1.3. Preparation of di-tert-butyl-N,N-diethylphosphoramidite

The compound was prepared according to the procedure.^[219] A solution of tert-butanol (0.88 mmol) and triethylamine (0.88 mmol) in dry ether (160 ml) was added to N,N-diethylphosphoramidous dichloride (76.5 g, 0.44 mmol) in dry ether (100 ml). The reaction mixture was kept below 0 °C (liquid nitrogen/acetone). On completion of addition, the mixture was stirred at room temperature for 3 hours. A solution of 5 % aqueous solution of

NaHCO₃ (70 ml) was then added, the mixture transferred to a separating funnel, and the aqueous phase discarded. The ethereal phase was washed with 5 % aqueous solution of NaHCO₃ (2·60 ml), saturated aqueous solution of NaCl (60 ml), and dried over Na₂SO₄. Filtration and evaporation of the solvent under reduced pressure followed by distillation of the crude residual under vacuum gave a clear liquid. The yield was (60 %). The product was used for phosphorylation step without further purification.

³¹P-NMR (CDCl₃): δ = 134.4 ppm (s). Impurities: 8.4 ppm (s, 5.6 %); -2.48 ppm (s, 1.4 %). ¹H-NMR (CDCl₃): δ = 0.92 ppm (t, -CH₃, J = 7.16 Hz, 6H); 1.2 ppm (s, (-C(CH₃)₃), 18 H); 2.9 ppm (doublet of quartet, -CH₂, J = 7.16 Hz, 4H). ¹³C-NMR (CDCl₃): δ = 15.6 ppm (d, J = 5.1 Hz); 31.7 ppm (d, J = 8.7 Hz); 38.2 ppm (d, J = 21.8 Hz); 75.14 ppm (d, J = 10.9 Hz).

4.1.4. Synthesis of 5,10,15,20-tetrakis(4-phosphoxyphenyl)porphine (*p*-TPPP)

4.1.4.1. Phosphorylation of *p*-THPP

1H-Tetrazole in acetonitril (4.2 ml, 3.3134 g, 47.3 mmol) was added in one portion to a stirred solution of the *p*-THPP [5,10,15,20-tetrakis(4-hydroxyphenyl)porphine] (0.2007 g, 0.296 mmol) and di-tert-butyl-N,N-diethylphosphoramidite (1.1796 g, 1.3 ml, 4.73 mmol) in dry dimethylformamide (20 ml) and stirred for 16 hours at room temperature. The mixture was then cooled to -40 °C (acetone/liquid nitrogen), and a solution of MCPBA (70 % of m-chloroperbenzoic acid from ALDRICH) (2.3351 g, 9.47 mmol) in CH₂Cl₂ (30 ml) was rapidly added so that the reaction temperature was kept below 0 °C. After stirring for 1 hour at 0 °C, 10 % aqueous Na₂S₂O₅ (50 ml) was added and the mixture was stirred for

another 15 minutes. The product was extracted with CH_2Cl_2 (200 ml). The organic phase was washed with 10 % aqueous $\text{Na}_2\text{S}_2\text{O}_5$ (2·50 ml), 0.5 M aqueous NaOH (2·50ml), dried over Na_2SO_4 and filtered. The solution was concentrated to 5 ml under vacuum, mixed with 100 ml of n-hexane and cooled overnight to 4 °C. The precipitated brown residue was washed three times with n-hexane and dried under vacuum. The yield was 356 mg (83 %). ^{31}P -NMR (CDCl_3): $\delta = -14.58$ ppm (s). ^1H -NMR (CDCl_3): $\delta = -2.84$ ppm (br s, 2 H, NH) 1.69 ppm (s, 72 H, CH_3); 7.62 ppm (d, $J = 8.48$ Hz, 8 H, Ar); 8.15 ppm (d, $J = 8.48$ Hz, 8 H, Ar); 8.85 ppm (s, 8 H, pyrrole). ^{13}C -NMR (CDCl_3): $\delta = 30.16$ ppm (d, $J = 4.36$ Hz, CH_3); 84.15 ppm (d, $J = 7.27$ Hz, t-butyl C-O); 118.51 ppm (d, $J = 5.09$ Hz, Ar-ortho C); 119.49 ppm (pyrrole); 135.5 ppm (Ar-para C); 138.32 ppm (Ar-meta C); 151.64 ppm (d, $J = 7.27$ Hz, Ar-ipso C).

4.1.4.2. Deprotection

20 ml of concentrated HCl was added to 356 mg of the above compound in 80 ml of dry dioxane. The solution turned green. The mixture was stirred for three hours and removal of the solvent under vacuum gave a green solid which was dried in a desiccator. The yield was 253 mg (95%). The sodium salt of *p*-TPPP was prepared by adding 10 equivalents of sodium ethoxide dissolved in 150 ml dry ethanol. The resulting brown precipitate was stirred for 3 hours, filtered off under nitrogen atmosphere, washed several times with dry ethanol and dried in vacuum. The compound was highly hygroscopic. The hydration of the substance was clearly visible by the color change from brown to green. UV-visible measurement in water: λ_{max} at pH 10 ($\log \epsilon$) = 416 nm (5.57); λ_{max} at pH 5 ($\log \epsilon$) = 438 nm (5.57). IR (KBr)

cm⁻¹: 1638, 1603, 1504, 1467, 1400, 1385 (aromatic C=C, C=N ring stretch), 1240 (C-O stretch), 1172, 1107 (PO₄²⁻), 982 (C-O-P), 890, 804, 732 (C=C-H out of plane bend), 642, 575 (PO₄²⁻). ³¹P-NMR (D₂O): δ = 1.1 ppm (s). ¹H-NMR (D₂O): δ = 7.52 ppm (d, 8 H, *J* = 8.48 Hz, Ar); 8.04 ppm (d, 8 H, *J* = 8.48 Hz, Ar); 9.03 ppm (br s, 8 H, Pyr). ¹³C-NMR (D₂O): 119.6 ppm (d, *J* = 3.63 Hz, Ar-ortho C), 120.3 ppm, 135.6 ppm (Ar-para C), 136.8 ppm (Ar-meta C), 154.7 ppm (d, *J* = 5.81 Hz, Ar-ipso C). ESI-MS⁻ *m/z* = 248.5158 (M⁴⁺), C₄₄H₃₀N₄O₁₆P₄⁴⁺ would be 248.5157.

4.1.5. Preparation of *O*-phospho-L-tyrosine

The compound was prepared according to the procedure.^[242] In a 100 ml round bottom schlenk flask equipped with a magnetic stirrer, fresh phosphorus pentoxide (10 g, 70.4 mmol) and 85 % phosphorus acid in water (12 ml) are placed. L-tyrosine (3.22 g, 17.8 mmol) was added and mixed with the aid of a vibramix. The reaction mixture is heated and stirred at 80 °C for 40 hours. To the amber viscous liquid, water (30 ml) was added and heating was continued for 30 minutes. The reaction mixture was cooled to room temperature, diluted with n-butanol (650 ml) and kept stirring for 3 hours. The fine white precipitate was filtered washed successively with ice water (2·20 ml), ethanol (2·20 ml) and ether (4·20 ml). The yield was 2.42 g (50 %).

IR (KBr) cm⁻¹: 3310-3600 cm⁻¹ (broad band, O-H and N-H stretch), 3123, 3086, and 3024 (aromatic C-H stretch), 2976 and 2926 cm⁻¹ (aliphatic C-H stretch), 1732 cm⁻¹ (carboxylic C=O stretch), 1607, 1512, 1456, 1385, 1230, 1144, 1045, 953 (C=C, C-N, N-H, PO₄²⁻) 851 (C-H out of plane bend), 561, 571 (PO₄²⁻). ³¹P-NMR (D₂O): δ = -3.27 ppm (s). ¹H-NMR (D₂O): δ = 2.94 to

3.19 ppm (doublet of quartet, -CH₂-Ar; 2H); 4.05 to 4.09 ppm (doublet of doublet, chiral-CH, 1H); 6.98 to 7.12 ppm (doublet of doublet, Ar, 4H). ¹³C-NMR (D₂O): δ = 35.2 ppm (-CH₂-); 54.6 ppm (-CH-); 121.36 ppm (d, *o*-C); 130.07 ppm (*p*-C); 130.08 ppm (*m*-C); 151.9 ppm (d, *ipso*-C); 172.04 ppm (-C(O)-O). Elemental Analysis: calculated for (C₉H₁₂N₁O₆P₁): C, 41.39; H, 4.63; N, 5.36. Found: 41.05; H, 4.695; N, 5.27. ESI-MS⁺ *m/z* = 306.0103 (M⁺), C₉H₁₁N₁Na₂O₆P₁⁺ would be 306.0114.

4.1.6. Dodecyl phosphate (DDP)

The compound was prepared according to the procedure.^[243] In a dry, nitrogen purged flask, equipped with a reflux condenser, a magnetic stirrer, and a dropping funnel was placed 8.2 g (57.9 mmol) of diphosphorus pentoxide. Toluene (100 ml) and 18.81 g (24.6 ml, 115.8 mmol) of hexamethyldisiloxane were added. The mixture was refluxed, until it became clear (ca. 1h). After cooling, 21.58 g (25.9 ml, 115.8 mmol) of 1-dodecanol was added drop wise, and it was refluxed for 3 h. The solution was cooled and removal of solvent in *vacuo* left viscous oily residue. The residue was dissolved in 120 ml of ether. The ethereal solution was washed twice with 10 ml of water and, subsequently extracted three times with 20 ml of 5% sodium hydroxide solution. The combined alkaline extracts were acidified with 60 ml of 10% hydrochloric acid solution, and again extracted three times with 100 ml of ether. The ethereal solution was dried (Na₂SO₄), and evaporation of the ether gave 13.25 g of colorless crystalline product (43 % yield) in an almost pure state. The product was recrystallized in n-hexane.

m. p: 59.1 °C to 60.3 °C. ³¹P-NMR (CDCl₃): δ = 2.29 ppm (s). ¹H- NMR (CDCl₃): δ = 0.86 ppm (t, -CH₃); 1.24 ppm (s, -(CH₂)₉-); 1.65 ppm (quintet,

-CH₂-); 4.01 ppm (quartet, -CH₂-O-). Elemental analysis. Calculated for (C₁₂H₂₇O₄P₁): C, 54.12; H, 10.22. Found: C, 54.14; H, 10.44.

The sodium salt of dodecyl phosphoric acid was prepared by treating the free acid with two equivalents of sodium ethoxide in hot ethanol. The immediately formed white solid was allowed to stir for 3 h at room temperature. The solid was collected by filtration and vacuum dried under vacuum.

³¹P-NMR (D₂O): δ = 4.34 ppm (s). ¹H-NMR (D₂O): δ = 0.69 ppm (t, -CH₃); 1.11 ppm (s, -(CH₂)₇-); 1.39 ppm (quintet, -CH₂-); 3.56 ppm (quartet, -CH₂-O-). Elemental analysis: Calculated for (C₁₂H₂₅O₄P₁Na₂): C, 46.45; H, 8.12; Na, 14.82. Found: C, 46.75; H, 8.575; Na, 14.46.

4.1.7. Tetradecyl phosphate (TDP)

The preparation of TDP was carried out as described above for DDP. The yield was 44 %.

³¹P-NMR (CDCl₃): δ = 2.96 ppm (s). ¹H-NMR (CDCl₃): δ = 0.82 ppm (t, -CH₃); 1.27 ppm (s, -(CH₂)₉-); 1.67 ppm (quintet, -CH₂-); 4.02 ppm (quartet, -CH₂-O-); 8.7 ppm (s, -OH). Elemental analysis: Calculated for (C₁₄H₃₁O₄P₁): C, 57.12; H, 10.61. Found: C, 57.5; H, 10.93.

The sodium salt of tetradecyl phosphoric acid was prepared by treating the free acid with 2 equivalents of sodium ethoxide in hot ethanol. The immediately formed white solid was allowed to stir for 3 h at room temperature. The solid was collected by filtration and dried under vacuum.

³¹P NMR (CDCl₃): δ = 4.30 ppm (s). ¹H-NMR (CDCl₃): δ = 0.69 ppm (t, -CH₃); 1.11 ppm (s, -(CH₂)₇-); 1.40 ppm (quintet, -CH₂-); 3.56 ppm (quartet,

-CH₂-O-). Elemental analysis: Calculated for (C₁₄H₂₉O₄P₁Na₂): C, 49.70; H, 8.64; Na, 13.59. Found: C, 50.57; H, 8.95; Na, 13.7.

4.1.8. Octadecyl phosphate (ODP)

The preparation of ODP was carried out as described above for DDP. The yield was 35 %. ³¹P-NMR (CDCl₃/DMSO-d₆): δ = -0.5 ppm (s). ¹H-NMR (CDCl₃/DMSO-d₆): δ = 0.84 ppm (t, -CH₃); 1.22 ppm (s, -(CH₂)₉-); 1.55 ppm (quintet, -CH₂-); 3.80 ppm (quartet, -CH₂-O-). Elemental analysis: Calculated for (C₁₈H₃₉O₄P₁): C, 61.69; H, 11.2. Found: C, 61.57; H, 11.57.

The potassium salt of octadecyl phosphoric acid was prepared by treating the free acid with potassium ethoxide in hot ethanol. The immediately formed white solid was allowed to stir for 3 h at room temperature. The solid was collected by filtration and dried under vacuum. Elemental analysis: Calculated for (C₁₈H₃₉O₄P₁): C, 50.67; H, 8.74. Found: C, 50.043; H, 9.25.

4.1.9. *p*-dodecyloxyphenyl phosphate (DDOPhP)

4.1.9.1. *p*-dodecyloxyphenol

A mixture of hydroquinone (59.4 g, 0.54 mol), dodecylbromide (34.8923 g, 0.14 mol), K₂CO₃ (37.25 g, 0.27 mol) and cyclohexanone (150 ml) was refluxed for 24 h. The solvent was removed and the residue was redissolved in CH₂Cl₂ and aqueous HCl mixture. The acid layer was extracted several times with CH₂Cl₂ and the combined layer was washed two times with water. The organic layer was dried over Na₂SO₄ and the solvent was evaporated in rotary evaporator. Recrystallizing the product from ethanol at room temperature separated the mixture of the product.

$^1\text{H-NMR}$ (DMSO- d_6): $\delta = 0.88$ ppm (t, CH_3 , 3H); 1.25 to 1.5 ppm (18 H); 1.75 ppm (quintet, CH_2 , 2H); 3.89 ppm (t, $\alpha\text{-CH}_2$, 2H); 6.7 to 6.81 ppm (m, Ar, 4H). $^{13}\text{C-NMR}$ (DMSO- d_6): $\delta = 153.45$ ppm; 149.37 ppm; 116.08 ppm; 115.7 ppm; 68.82 ppm; 32.04 ppm; 29.77 ppm; 29.53 ppm; 29.49 ppm; 29.46 ppm; 26.15 ppm; 22.80 ppm; 14.23 ppm.

4.1.9.2. *p*-dodecyloxyphenyl phosphate

2 g of *p*-dodecyloxyphenol (7.18 mmol, 1 equivalent) was taken in 80 ml of Benzene. To the clear solution, 6.575 ml of POCl_3 (11.0139 g, 71.8 mol, 10 equivalents) was added. The clear solution was refluxed for 18 hours. The mixture was cooled to room temperature and removal of the solvent under *vacuo* left white residue. It was taken in 100 ml of ether and 20 ml of water was added to it under cold condition. The mixture was stirred overnight at room temperature. The ether layer was separated, washed with 10 ml of water and dried over Na_2SO_4 . The solvent was removed under vacuum. The product was recrystallized several times from hot *n*-hexane. The yield was very poor (10 %). The experiment was carried out in the presence of base, pyridine or triethylamine, improved the yield (30 %).

$^{31}\text{P-NMR}$ (DMSO- d_6): $\delta = -4.67$ ppm (s). $^1\text{H-NMR}$ (DMSO- d_6): $\delta = 0.85$ ppm (t, CH_3 , 3H); 1.24 – 1.37 ppm (18 H); 1.67 ppm (quintet, CH_2 , 2H); 3.89 ppm (t, $\alpha\text{-CH}_2$, 2H); 6.7 to 7.06 ppm (m, Ar, 4H). $^{13}\text{C-NMR}$ (DMSO- d_6): $\delta = 155.035$ ppm; 144.91 ppm (d); 121.01 ppm (d); 115.28 ppm, 67.1 ppm, 31.31 ppm, 29.03 ppm, 28.79 ppm, 28.73 ppm, 25.53 ppm, 22.11 ppm, 13.96 ppm. Elemental Analysis: Calculated for ($\text{C}_{18}\text{H}_{31}\text{O}_5\text{P}_1$): C, 60.32; H, 8.72. Found: C, 60.52; H, 9.015.

4.1.10. *p*-dodecyloxybiphenyl-*p'*-phosphate (DDOBPhP)

4.1.10.1. *p*-dodecyloxy-*p'*-hydroxybiphenyl

A schlenk flask equipped with a magnetic stirrer, 18.621 g of 4,4'-dihydroxybiphenyl (100 mmol), 1.3336 g of NaOH (33 mmol) and 8.077 g of 1-bromododecane (8 ml, 33 mmol) in 400 ml of absolute Ethanol was refluxed at 80 °C for 4 hours. The mixture was allowed to stand overnight at room temperature. The crystallized solid was filtered and washed with minimum amount of ethanol. The solid was dried overnight under vacuum. The yield was 6.44 g (55 %).

¹H-NMR (CDCl₃/DMSO-d₆): δ = 0.73 ppm (t, CH₃, 3H); 1.12 to 1.32 ppm (γ-CH₂ and (CH₂)₈, 18 H); 1.63 ppm (quintet, β-CH₂, 2H); 3.8 ppm (t, α-CH₂, 2H); 6.7 ppm (4peaks grouped, 3,3'-H of biphenyl, 4H); 7.24 ppm (4 peaks grouped, 2,2'-H of biphenyl, 4H); 8.89 ppm (br s, -OH, 1H). ¹³C-NMR (CDCl₃/DMSO-d₆): δ = 157.09 ppm (s, 4-C of biphenyl); 155.74 ppm (s, 4'-C of biphenyl); 132.4 ppm (s, 1-C of biphenyl); 130.8 ppm (s, 1'-C of biphenyl); 126.6 ppm (s, 2'-C of biphenyl); 126.4 ppm (s, 2-C of biphenyl); 114.9 ppm (s, 3'-C of biphenyl); 113.9 ppm (s, 3-C of biphenyl); 67.1 ppm (s, 1-C of alkyl chain); 30.9 ppm (10-C); 28.68 ppm, 28.66 ppm, 28.63 ppm, 28.44 ppm, 28.37 ppm (2,4,9-C); 25.13 ppm (3-C); 21.74 ppm (11-C); 13.35 ppm (12-C). Elemental analysis: Calculated for (C₂₄H₃₄O₂): C, 81.31; H, 9.67. Found: C, 81.63; H, 10.09.

4.1.10.2. *p*-dodecyloxybiphenyl-*p'*-phosphate

To the freshly prepared *p*-dodecyloxy-*p*-hydroxybiphenyl (5 g, 14.1 mmol) in dry benzene (80 ml), POCl₃ (141 mmol) was added and warmed the

solution to 50 °C. 1.6733 g of pyridine (141 mmol) was slowly added drop wise. The solution was refluxed for 3.5 hours. After cooling, the mixture was filtered and the solvent was evaporated under vacuum. The residue was treated with 25 ml of water and stirred overnight. To this 100 ml of dry ethanol was added and warmed to 100 °C. The milky white precipitate was immediately filtered and dried under vacuum. The yield was 22 %.

³¹P-NMR (DMSO-d₆): δ = -4.66 ppm (s). ¹H-NMR (DMSO-d₆): δ = 0.85 ppm (t, J = 6.97 Hz, CH₃, 3H); 1.36 ppm (γ -CH₂ and (CH₂)₈, 18 H); 1.71 ppm (quintet, J = 6.41 Hz, β -CH₂, 2H); 3.9 ppm (t, J = 6.41 Hz, α -CH₂, 2H); 6.95 ppm (d, J = 8.67 Hz, 4H); 7.20 ppm (d, J = 8.67 Hz, 2H); 7.51 ppm (dd, J = 6.78 Hz, 4H). ¹³C-NMR (DMSO-d₆): δ = 158.16 ppm; 150.55 ppm; 135.69 ppm; 131.77 ppm; 127.5 ppm; 127.2 ppm; 120.46 (d, J = 5.1 Hz); 114.83 ppm; 67.5 ppm; 31.31 ppm; 29.05 ppm, 29.02 ppm, 28.77 ppm, 28.68 ppm (m); 25.52 ppm; 22.11 ppm; 13.97 ppm. Elemental analysis: Calculated for (C₂₄H₃₅O₅P₁): C, 66.34; H, 8.12. Found: C, 66.56; H, 8.21.

4.1.11. Preparation of organic phosphate-functionalized calcium phosphate nanoparticles: General procedure

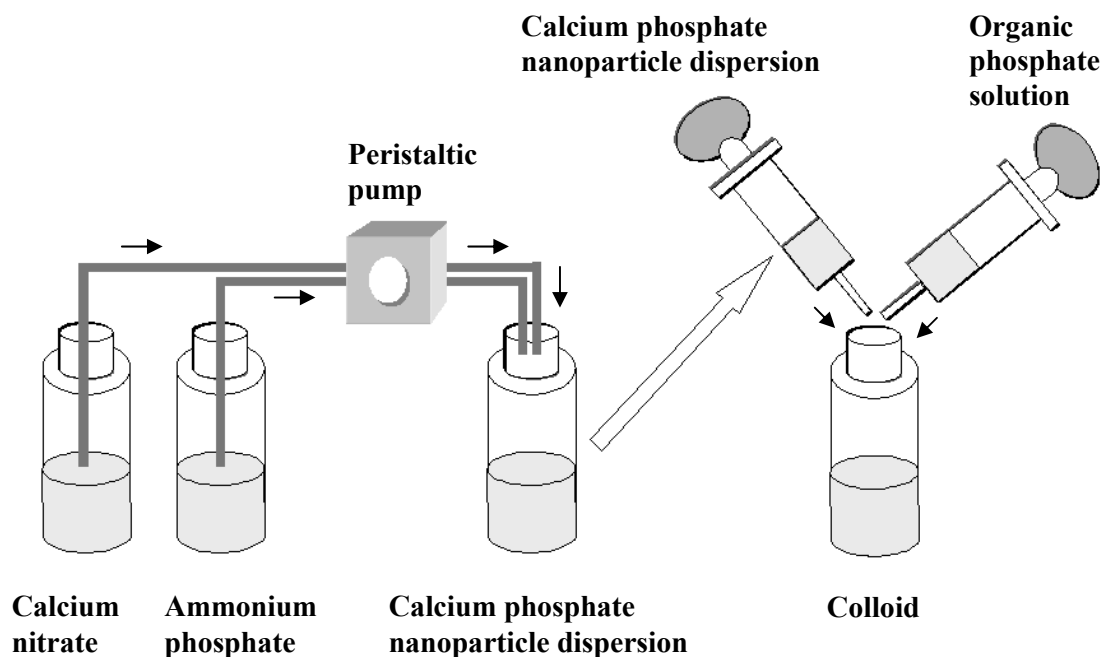


Figure 50: Schematic diagram of the preparation of functionalized calcium phosphate nanoparticles.

The calcium phosphate nanoparticles were prepared by pumping aqueous solutions of $\text{Ca}(\text{NO}_3)_2 \cdot 4 \text{H}_2\text{O}$ and $(\text{NH}_4)_2\text{HPO}_4$ into a stirred vessel (see Fig. 50). The concentration of calcium and phosphate solutions was used with the stoichiometric ratio ($\text{Ca}:\text{P} = 1.67:1$), corresponding to hydroxyapatite [$\text{Ca}_5(\text{PO}_4)_3(\text{OH})$]. The pH of the calcium and phosphate solutions was previously adjusted to 9-10 with 0.1 N aqueous NaOH. A few seconds after mixing, the nanoparticle dispersion was taken with a syringe. The colloids were prepared by rapidly mixing an aqueous solution of the organic phosphate and the dispersed calcium phosphate nanoparticles. The final pH of the colloid was between 7.5 and 8.5. The particles were studied either as

dispersion or after collecting the particles by ultracentrifugation at 371,000 g or by filtration (supra[®]-100 by PALL Life sciences). The centrifuged or filtered nanoparticles were washed with 100 ml of absolute ethanol and dried in air. Ultrapure water (Purelab ultra instrument from ELGA) was used for all preparations.

4.1.12. Cell culture experiments

In the cooperation with the University of Bochum, Chair of Molecular Neurochemistry, the cell culture studies were carried out. All cell culture work was carried out with sterile solutions. NIH 3T3 cells (fibroblasts) were used. The cells were seeded 24 h before the experiment in 24-well plates with 50,000 cells per well. 100 μ l of the calcium phosphate/p-TPPP colloid with a p-TPPP concentration of 7.5 μ M were mixed with 500 μ l cell culture medium (RPMI-1640 with 10 % FCS). The cell culture medium was removed and replaced with 500 μ l of the above described mixture. Before the microscopic analysis, the cells were washed twice with PBS to remove dispersed particles and dissolved porphyrin. Fluorescence microscopy was carried out with an IX51 microscope (Olympus, Hamburg, Germany) and a Leica TCF SP2 confocal laser scanning microscope.

An MTT-assay was performed as follows: The MTT stock solution, 3-(4,5-dimethylthiazol-2-yl)-2,5-diphenyltetrazolium bromide in PBS (5 mg ml⁻¹) was prepared and diluted to 1 mg ml⁻¹ in cell culture medium. The cells were seeded for 24 h before the incubation with calcium phosphate/p-TPPP-nanoparticles. After 7, 24 and 48 h incubation, respectively, the cell culture medium was replaced with 300 μ l of the MTT solution and the cells were incubated for 1 h at 37 °C under 5 % CO₂. Then the MTT solution was

removed and replaced with 300 μ l DMSO solution. The cells were incubated for 30 more minutes under the conditions described above and then a 70 μ l aliquot was taken for spectrophotometric analysis using a ELISA-Reader (SLT Labinstruments, Salzburg, Austria) operating at $\lambda = 560-600$ nm.

4.2. Instrumental techniques

4.2.1. Nuclear magnetic resonance (NMR)

Nuclear magnetic resonance spectroscopy is another form of absorption spectroscopy. It is concerned with the nuclear spin in the lowest energy state. A sample can absorb electromagnetic radiation in the radio frequency region at frequencies specially governed by the characteristics of the sample. The fundamental relationship in NMR is the Larmor equation.

$$\nu = \gamma \cdot B_0 / 2\pi$$

where

$$\gamma = 2\pi\mu / \hbar I$$

This equation correlates the applied radio frequency (ν) with the magnetic field strength (B_0). The magnetogyric ratio (γ) is the proportionality constant between the magnetic moment (μ) and the spin number (I). Generally the resonance frequencies are expressed relative to a standard compound. Tetramethylsilane (TMS) is the standard for both ^1H and ^{13}C NMR. The difference in the absorption position of a particular proton from the absorption position of a reference proton is called the chemical shift of this particular proton.

$$\text{Chemical Shift in ppm } (\delta) = \frac{\text{Chemical shift from Reference in Hz}}{\text{Spectrometer Frequency in Hz}} \cdot 10^6$$

The chemical shifts of the NMR signals were determined in parts per million (ppm) and are referenced to residual solvent peaks (^1H - and ^{13}C NMR). The samples for ^{31}P -NMR were referenced externally with 85 % H_3PO_4 .

^1H -, ^{13}C -, and ^{31}P -NMR measurements were carried out with a Bruker DPX 300 MHz NMR spectrometer operating at 300 MHz, 75.5 MHz, and 121.5 MHz respectively. Standard NMR tubes with a diameter of 5 mm were used. About 10 to 15 mg of a sample were dissolved in 0.5 to 0.6 ml of the deuterated solvent.

4.2.2 Dynamic light scattering (DLS)

Dynamic light scattering is one of the methods used to determine the size of particles. The experiment's theory is based essentially on two assumptions. The first assumption is that the particles are in Brownian motion. The second one is that the particles observed in the experiment are spherical with a diameter that is small compared to the molecular dimensions.

Shining a monochromatic light beam onto a solution with spherical particles in Brownian motion causes a Doppler shift when the light hits the moving particle, changing the wavelength of the incoming light. This change is related to the size of the particle. It is possible to compute the sphere size distribution and give a description of the particle's motion in the medium, measuring the diffusion coefficient of the particle:

$$D_T = k_B T / 6 \pi \eta R_h$$

where D_T is the translation diffusion coefficient, k_B is the Boltzmann's constant, T is the temperature in Kelvin degrees, η is the viscosity of the solvent and R_h is the hydrodynamic radius. Since from the light scattering it is possible to obtain information about the positions of the particles, from the formulas above the radius of the particles can be computed.

Dynamic light scattering determinations were performed with a Zetasizer (NanoZS from Malvern instruments).

4.2.3 Zeta potential measurements (ZP)

The zeta potential is the electrical potential that exists at the Stern plane of a particle, which is at some small distance from its surface. The zeta potential is derived from measuring the mobility distribution of a dispersion of charged particles as they are subjected to an electric field. The particle mobility is defined as the velocity of a particle per electric field unit and is measured by applying an electric field to the dispersion of particles and measuring their average velocity. There are two approximations (by Hückel and by Smoluchowski) to obtain the zeta potential from the measured particle mobility. The approximation by Hückel applies to particles smaller than 10 nm. Because our particles were larger the model of Smoluchowski was used.

$$Be = (\varepsilon \zeta f_b / \eta) (\omega r^2 \rho / \eta)$$

Be: electrophoretic mobility, ε : dielectric constant, ζ : zeta potential, η : viscosity, ω : frequency of the electrical field, r : radius of the particle, ρ : density of the dispersion, f_b : correction factor.

The measurements for the computation of the zeta potential were carried out with a Malvern Zetasizer Nano ZS.

4.2.4 Infrared spectroscopy (IR)

Infrared spectroscopy (IR Spectroscopy) is a type of absorption spectroscopy that uses the infrared part of the electromagnetic spectrum (wavelength 760 nm up to 500 μ m). Infrared radiation does not trigger electronic excitation in

substances but vibrational and/or rotational excitation. To be infrared active, a molecule must possess a dipole moment or must generate a dipole moment by vibration. The main modes of vibration are valence bond vibration, in which the atom vibrates along a bond axis, and deformation vibration, which occurs in molecules (bending/rocking vibrations - in the plane of the bonds or twisting/wagging vibrations - out of the plane of the bands). The energy in infrared spectra is usually given in wave numbers. The use of wave numbers offers the advantage of being directly proportional to the frequency of the absorbed radiation and thus the energy absorbed. Infrared spectroscopy deals with the interaction of infrared light with matter. The energy of an infrared photon can be calculated using the Planck energy relation

$$\Delta E = h c \bar{\nu}$$

with E the absorbed energy in J, $h = 6.626 \cdot 10^{-34}$ J s Planck's constant, $c = 3 \cdot 10^{10}$ cm s⁻¹ the speed of light, and $\bar{\nu}$ the wave number in cm⁻¹.

The extent of absorption of infrared photons depends mainly on the mass of the vibrating atoms. Detailed information about the infrared absorptions observed for various functional groups can be found in the literature.

All the samples examined were mixed with an about 200 fold excess of potassium bromide and pressed into pellets at 10 tons for 15 minutes. Measurements were carried out with a Bruker Vertex 70 FT-IR spectrometer (resolution 2 cm⁻¹, averaging of 20 scans)

4.2.5 X-ray diffractometry (XRD)

Crystals are ordered, three-dimensional arrangements of atoms with characteristic periodicities. As the spacing between atoms is of the same order as X-ray wavelengths (1-3 Å), crystals can diffract the radiation when the diffracted beams are inphase. The Bragg equation is given as

$$n \cdot \lambda = 2 \cdot d_{hkl} \cdot \sin(\theta)$$

For a given wavelength (λ), diffraction can only occur at a certain angle (θ) for a given d-spacing between the lattice planes hkl in Å. Here n is an integer value.

X-rays can be used to measure the distance between successive atomic planes and positions of atoms or ions within a crystal, allowing for the determination of crystal structure, whereas powder XRD can be used to fingerprint minerals without any prior knowledge of crystal structure or symmetry.

X-ray powder diffraction was measured in the instrument: STOE IP-PSD diffractometer or Siemens D500 diffractometer. The samples were measured with Cu $K\alpha_1$ -radiation ($\lambda = 1.54056 \text{ \AA}$), with 50 kV and 30 mA.

4.2.6 Scanning electron microscopy (SEM)

Classical microscopes are limited in resolution to the wavelength of visible light (400-750 nm). The scanning electron microscope (SEM) is a type of electron microscope capable of producing high-resolution images of a sample surface. With scanning electron microscopes, much smaller objects can be observed because high energy electrons are used for image creation.

When an electron beam interacts with a solid, various types of elastic and inelastic processes occur, including electron scattering and excitation. The inelastic scattering of secondary electrons is detected here. The secondary electron current reaching the detector is recorded and the microscope image consists of a plot of this current against probe position on the surface. The contrast in micrograph arises from variations in the surface topography. Consequently, the scanning electron microscopy provides a direct image of the topographical nature of the surface from all the excited secondary electrons.

The samples must be sputtered with a thin film of gold-palladium [80:20], so that the samples must be electrically conducting. This thin metal coating does not affect the surface features of the sample. This type of coating is essential for insulators. Sputtering exposes the samples to seven minutes of vacuum and an electric field.

For the SEM observation, a FEI ESEM Quanta 400 FEG microscope coupled with energy-dispersive X-ray spectroscopy (SEM-EDX) was used. The analysis of elements present in the sample was detected by EDX with a the S-UTW-Si(Li) detector.

4.2.7. UV-vis spectroscopy

UV-vis spectroscopy refers to electronic transitions occurring in the region of the electromagnetic spectrum (200-800 nm) accessible to standard UV-vis spectrometers. When sample molecules are exposed to light having an energy that matches a possible electronic transition within the molecule, some of the light energy will be absorbed as the electron is promoted to a higher energy orbital. An optical spectrometer records the wavelengths at

which absorption occurs, together with the degree of absorption at each wavelength. The resulting spectrum is presented as a graph of absorbance (A) versus wavelength. Beer-Lambert's Law is given as

$$A = \epsilon \cdot c \cdot l$$

where ϵ is the absorption coefficient ($\text{dm}^3 \text{mol}^{-1} \text{cm}^{-1}$) of the absorbing medium, c is the concentration (mol dm^{-3}) of the sample and l is the path length (cm) through the sample. According to Beer-Lambert's law, absorption is directly proportional to concentration and the path length. The unknown concentrations of the sample can be measured by plotting the absorption (A) versus known concentration (c) of the standard samples. This results in a linear plot, obeying the Beer-Lambert's law.

The spectral lines are normally broad due to the collision of the molecules in the liquid phase. This is often referred as collision broadening.

It is most commonly used to refer the shifts in absorption bands and their intensity changes as follows:

Bathochromic shift or red shift: a shift of λ_{max} to longer wavelengths.

Hypsochromic shift or blue shift: a shift of λ_{max} to shorter wavelengths.

Hyperchromic shift: an increase in the intensity of an absorption band, usually with reference to its molar extinction coefficient ϵ_{max} .

Hypochromic shift: a decrease in the intensity of an absorption band with reference to ϵ_{max} .

Varian Cary WinUV spectrophotometer was used and the samples were loaded in 1 cm quartz cuvettes. A blank sample was measured first by placing the empty cuvette by which the instrument has been zeroed by displaying an absorbance value of 0.0000. The absorbance value may vary

slightly (about ± 0.0005). This may be due to noise. After this measurement, the solvent (normally water) was measured as background. The samples were measured further using the same cuvette.

4.2.8. Fluorescence spectroscopy

Fluorescence occurs when a molecule absorbs photons from the UV-vis light spectrum (200-900 nm), causing transition to a high-energy electronic singlet state and then emits photons as it returns to its initial state, in less than 10^{-9} sec. The absorbed photon must be equivalent to the energy difference between the ground state and the higher energy state. This energy is termed the excitation energy and the corresponding wavelength is called the excitation wavelength. The emission energy from the excited molecule to the ground state through heat and/or emission of energy quanta such as photons is also equivalent to the difference between the two discrete energy levels. This is referred to as emission energy and the corresponding wavelength is called emission wavelength. Some energy within the molecule is lost through heat or vibration so that the emitted energy is less than the excitation energy; therefore, the emission wavelength is always longer than the excitation wavelength. The difference between the excitation and emission wavelengths is called the Stokes shift.

Emission and excitation spectra were measured at room temperature using a J&M spectrofluorometer (Analytische Mess- und Regeltechnik FL3095-500) equipped with a diode array polychromator and a 75 W Xenon lamp. The emission spectra were corrected for the detector sensitivity and the excitation spectra for the intensity of the exciting light.

4.2.9. Electron spray ionization mass spectrometry

Bruker BioTOF III electron spray ionization-mass spectrometry equipped with an electron spray ionisation gun was employed to measure the molecular weight of the sample. Ultrapure water was used to prepare the samples and the concentration of the samples was up to 10 μM .

The samples were measured in the Institute of Organic Chemistry, University of Duisburg-Essen.

5. Summary

The principal goals of this thesis were to functionalize calcium phosphate nanoparticles with organic phosphates and to stabilize the nanoparticles as stable colloid. The intention of this project was approached successfully with some organic phosphates. The results are summarized here.

The calcium phosphate nanoparticles were prepared by a continuous precipitation method and immediately stabilized as colloid by rapidly adding an aqueous solution of organic phosphate. A variety of organic phosphates (porphyrin, phytic acid, phosphoamino acid and surfactants) was used to functionalize the calcium phosphate surface. The conditions were optimized to prepare stable monodisperse colloids.

Organic phosphate showed a high chemical affinity to bind to the calcium phosphate surface which was confirmed by the zeta potential values (-20 mV...-35 mV). The particle size, morphology, and porosity were determined by the surface-adsorbed organic phosphates. For example,

- (a) *p*-TPPP-functionalized particles – aggregation of primary calcium phosphate particles (*ca.* 20-30 nm) into *ca.* 250 nm solid spherical particles.
- (b) Phytic acid-functionalized particles – solid spherical particles.
- (c) TyrP-functionalized particles – aggregation of primary calcium phosphate particles (*ca.* 20-30 nm) into *ca.* 250 nm hollow spherical particles
- (d) Alkyl phosphate-functionalized particles – needle- or flower-like microparticles.

The number of phosphate groups present in organic phosphates and their concentration played a critical role in determining the nature of particle precipitation. For example, the *p*-TPPP molecule has four phosphate groups.

It functionalized the calcium phosphate surface and stabilized the particles in solution only when the *p*-TPPP to calcium concentration ratio was 1:100. If an excess amount of *p*-TPPP was used (*p*-TPPP:Ca²⁺=1:30), only the calcium salt of *p*-TPPP was obtained.

p-TPPP-functionalized calcium phosphate nanoparticles were prepared and used in cell culture studies to check its viability. In collaboration with the Chair of Molecular Neurochemistry at the University of Bochum, the cell culture experiments were carried out. The *p*-TPPP-functionalized calcium particles were taken up by the NIH 3T3 fibroblast cell and no adverse effect was observed. This showed a good prospect that the nanoparticles can be used as fluorescing agents without any adverse effects in the cells.

A new and simple method to prepare calcium phytate nanoparticles was described where calcium phosphate nanoparticles were used as nuclei. This method works only in a narrow concentration range of phytic acid. The size of the calcium phytate nanoparticles can be adjusted by varying the calcium to phytate ratio. As the colloids of calcium phytate are stable and biocompatible, they may be used in biomedical studies (e.g. liver and spleen scintigraphy) without any other stabilizing agents.

The one-step synthesis of hollow particles was described in our study which is easy, simple and more convenient. The hollow spherical particles are formed by the direct self-assembly of the primary calcium phosphate nanoparticles in the presence of an excess amount of *O*-phospho-L-tyrosine. It was found from SEM measurements that the hollow morphology was not stable under mechanical agitation and thermal conditions. The simple procedure for the preparation of hollow calcium phosphate nanoparticles makes it advantageous over template-assisted method. These hollow particles may be used as drug delivery vehicles.

The alkyl phosphate-functionalized calcium phosphate colloids showed less stability. SEM measurements showed aggregated microparticles. The content of the alkyl phosphate in the precipitated particles was (about 10-30 wt%) estimated by elemental analysis. This indicated that the alkyl phosphates on the surface of hydroxyapatite underwent an ion exchange reaction with inorganic phosphate ions. As a result, the surface of the hydroxyapatite particles covered with the hydrophobic calcium salt of alkyl phosphate was found as precipitate.

6. Reference

- [1] S. Mann, *Biomineralization*, Oxford University Press, Oxford, **2001**.
- [2] S. V. Dorozhkin, M. Epple, *Angew. Chem. Int. Ed.* **2002**, *41*, 3130.
- [3] M. Vallet-Regi, *Dalton Trans.* **2006**, 5211.
- [4] M. Epple, E. Baeuerlein, in *Handbook of Biomineralisation, Vol. 3*, Wiley-VCH, Weinheim, **2007**.
- [5] C. Rey, C. Combes, C. Drouet, H. Sfihi, A. Barroug, *Mater. Sci. Eng. C* **2007**, *27*, 198.
- [6] H. Lowenstam, S. Weiner, *On Biomineralization*, Oxford University Press, New York, **1989**.
- [7] M. Epple, E. Baeuerlein, *Biomineralisation: Medical and Clinical Aspects*, Wiley-VCH, Weinheim, **2007**.
- [8] V. Sokolova, M. Epple, *Angew. Chem. Int. Ed.* **2008**, *47*, 1382.
- [9] A. Doat, M. Fanjul, F. Pelle, E. Hollande, A. Lebugle, *Biomaterials* **2003**, *24*, 3365.
- [10] A. Doat, F. Pelle, N. Gardant, A. Lebugle, *J. Solid State Chem.* **2004**, *177*, 1179.
- [11] W. Wang, D. Shi, J. Lian, Y. Guo, G. Liu, L. Wang, R. C. Ewing, *Appl. Phys. Lett.* **2006**, *89*, 183106.
- [12] J. Y. Chane-Ching, A. Lebugle, I. Rousselot, A. Pourpoint, F. Pellé, *J. Mater. Chem.* **2007**, *17*, 2904.
- [13] S. P. Mondejar, A. Kovtun, M. Epple, *J. Mater. Chem.* **2007**, *17*, 4153.
- [14] B. Palazzo, M. Iafisco, M. Laforgia, N. Margiotta, G. Natile, C. L. Bianchi, D. Walsh, S. Mann, N. Roveri, *Adv. Funct. Mater.* **2007**, *17*, 2180.
- [15] E. Boanini, M. Gazzano, K. Rubini, A. Bigi, *Adv. Mater.* **2007**, *19*, 2499.
- [16] A. Maitra, *Expert Rev. Mol. Diagn.* **2005**, *5*, 893.
- [17] Y. Kakizawa, S. Furukawa, A. Ishii, K. Kataoka, *J. Controlled Release* **2006**, *111*, 368.
- [18] V. V. Sokolova, I. Radtke, R. Heumann, M. Epple, *Biomaterials* **2006**, *27*, 3147.
- [19] D. Olton, J. Li, M. E. Wilson, T. Rogers, J. Close, L. Huang, N. P. Kumta, C. Sfeir, *Biomaterials* **2007**, *28*, 1267.
- [20] V. Sokolova, A. Kovtun, O. Prymak, W. Meyer-Zaika, E. A. Kubareva, E. A. Romanova, T. S. Oretskaya, R. Heumann, M. Epple, *J. Mater. Chem.* **2007**, *17*, 721.
- [21] V. Sokolova, A. Kovtun, R. Heumann, M. Epple, *J. Biol. Inorg. Chem.* **2007**, *12*, 174.
- [22] V. Sokolova, O. Prymak, W. Meyer-Zaika, H. Cölfen, H. Rehage, A. Shukla, M. Epple, *Mat.-wiss. u. Werkstofftech.* **2006**, *37*, 441.
- [23] S. Mann, J. P. Hannington, R. J. P. Williams, *Nature* **1986**, *324*, 565.
- [24] J. H. Collier, P. B. Messersmith, *Annu. Rev. Mat. Res.* **2001**, *31*, 237.
- [25] L. N. Y. Wu, B. R. Genge, R. E. Wuthier, *J. Biol. Chem.* **2008**, *283*, 3827.
- [26] G. A. Ozin, N. Varaksa, N. Coombs, J. E. Davies, D. D. Perovic, M. Ziliox, *J. Mater. Chem.* **1997**, *7*, 1601.
- [27] S. Mann, J. Webb, J. P. Williams, *Biomineralisation - Chemical and Biochemical Perspectives*, VCH Verlagsgesellschaft mbH, Weinheim, **1989**.

- [28] S. Weiner, P. M. Dove, *Rev. Mineral. Geochem.* **2003**, *54*, 1.
- [29] F. C. Meldrum, *Int. Mater. Rev.* **2003**, *48*, 187.
- [30] J. B. Thompson, G. T. Palocz, J. H. Kindt, M. Michenfelder, B. L. Smith, G. Stucky, D. E. Daniel E. Morse, P. K. Hansma, *Biophys. J.* **2000**, *79*, 3307.
- [31] R. Z. Wang, L. Addadi, S. Weiner, *Philos. Trans. Roy. Soc. B* **1997**, *352*, 469.
- [32] S. H. Yu, H. Cölfen, M. Antonietti, *J. Phys. Chem. B* **2003**, *107*, 7396.
- [33] G. Falini, S. Albeck, S. Weiner, L. Addadi, *Science* **1996**, *271*, 67.
- [34] D. B. DeOliveira, R. A. Laursen, *J. Am. Chem. Soc.* **1997**, *119*, 10627.
- [35] M. Neumann, M. Epple, *Eur. J. Inorg. Chem.* **2007**, 1953.
- [36] Y. Kojima, A. Kawanobe, T. Yasue, Y. Arai, *J. Ceram. Soc. Jpn. Int. Edn.* **1994**, *102*, 1131.
- [37] J. Aizenberg, G. Lambert, S. Weiner, L. Addadi, *J. Am. Chem. Soc.* **2002**, *124*, 32.
- [38] H. Setoguchi, M. Okazaaki, S. Suga, in *Origin, evolution, and modern aspects of biomineralization in plants and animals* (Ed.: R. E. Crick), Plenum Press, New York, **1989**, pp. 409.
- [39] M. G. Taylor, K. Simkiss, G. N. Greaves, M. Okazaki, S. Mann, *Proc. R. Soc. Lond. B* **1993**, *252*, 75.
- [40] J. Aizenberg, G. Lambert, L. Addadi, S. Weiner, *Adv. Mater.* **1996**, *8*, 222.
- [41] S. Weiner, W. Traub, *FEBS Lett.* **1986**, *206*, 262.
- [42] R. Z. Legeros, *Calcium phosphates in oral biology and medicine*, Karger, Basel, **1991**.
- [43] W. Suchanek, M. Yoshimura, *J. Mater. Res.* **1998**, *13*, 94.
- [44] L. L. Hench, *J. Am. Ceram. Soc.* **1998**, *81*, 1705.
- [45] E. D. Eanes, I. H. Gillessen, A. S. Posner, *Nature* **1965**, *208*, 365.
- [46] W. E. Brown, J. P. Smith, J. R. Lehr, A. W. Frazier, *Nature* **1962**, *196*, 1050
- [47] O. Suzuki, S. Kamakura, T. Katagiri, *J. Biomed Mater. Res. Appl Biomater.* **2006**, 201.
- [48] Y. A. Vinnikov, M. Z. Aronove, T. A. Kharkeevich, T. P. Tsurulis, E. A. Lavrova, Y. V. Natochin, *Z. Mikrosk. Anat. Forsch.* **1981**, *95*, 127.
- [49] F. Bosselmann, M. Epple, *Met. Ions Life Sci.* **2008**, *4*, 207.
- [50] D. Chapman, *J. Mar. Biol. Assoc. UK*, **1985**, *65*, 617.
- [51] D. B. Spangenberg, C. W. Beck, *Trans. Am. Microsc. Soc.* **1968**, *87*, 329.
- [52] D. Pollmanns, M. Hündgen, *Zool. Jb. Anat.* **1981**, *105*, 508.
- [53] S. Ueno, C. Imai, A. Mitsutani, *J. Plankton Res.* **1995**, *17*, 1381.
- [54] S. Ueno, C. Imai, A. Mitsutani, *Proc. 6th Int. Conf. Coelenterate Biology* **1997**, 491.
- [55] H. Tiemann, I. Sötje, A. Becker, G. Jarms, M. Epple, *Zool. Anz.* **2006**, *245*, 13.
- [56] H. Tiemann, I. Sötje, G. Jarms, C. Paulmann, M. Epple, B. Hasse, *J. Chem. Soc. Dalton Trans.* **2002**, 1266.
- [57] A. Becker, I. Sötje, C. Paulmann, F. Beckmann, T. Donath, R. Boese, O. Prymak, H. Tiemann, M. Epple, *Dalton Trans.* **2005**, 1545.
- [58] F. Boßelmann, M. Epple, I. Sötje, H. Tiemann, in *Biomineralisation: The Biology of Biominerals* (Ed.: E. Baeuerlein), Wiley-VCH, **2007**.
- [59] V. R. Franceschi, H. T. Horner, *Bot. Rev.* **1980**, *46*, 361.

- [60] H. J. Arnott, in *Biological Mineralization and Demineralization*, Three systems of biomineralization in plants with comments on the associated organic matrix ed. (Ed.: G. H. Nancollas), Springer Verlag, Berlin, **1982**.
- [61] H. J. Arnott, P. G. E. Pautard, in *Biological Calcification*, Calcification in plants ed. (Ed.: H. Schraer), Appleton-Century-Crofts, New York, **1970**.
- [62] A. Frey-Wyssling, *Am. J. Bot.* **1981**, *68*, 130.
- [63] S. R. Khan, R. L. Hackett, *J. Urol.* **1993**, *150*, 239.
- [64] W. H. Boyce, F. K. Garvey, *J. Urol.* **1956**, *76*, 213.
- [65] M. Khullar, S. K. Sharma, S. K. Singh, P. Bajwa, F. A. Sheikh, M. Sharma, *Urol. Res.* **2004**, *32*, 190.
- [66] N. Ciftcioglu, M. Bjorklund, K. Kuorikoski, K. Bergstrom, E. O. Kajander, *Kidney Int.* **1999**, *56*, 1893.
- [67] E. O. Kajander, M. Bjorklund, N. Ciftcioglu, *Proc. SPIE.-Int. Soc. Opt. Eng.* **1998**, *3441*, 86.
- [68] N. Ciftcioglu, M. Bjorklund, E. O. Kajander, *Proc. SPIE.-Int. Soc. Opt. Eng.* **1998**, *3441*, 105.
- [69] E. G. Cuerpo, E. O. Kajander, N. Ciftcioglu, F. L. Castellano, C. Correa, J. Gonzalez, F. Mampaso, F. Liano, E. G. de Gabiola, A. E. Barrilero, *Arch. Esp. Urol.* **2000**, *53*, 291.
- [70] K. K. Akerman, J. T. Kuikka, N. Ciftcioglu, J. Parkkinen, K. A. Bergstrom, I. Kuronen, E. O. Kajander, *Proc. SPIE.-Int. Soc. Opt. Eng.* **1997**, *3111*, 436.
- [71] F. A. Shiekh, M. Khullar, S. K. Singh, *Urol. Res.* **2006**, *34*, 53.
- [72] C. Kwak, H. K. Kim, E. C. Kim, M. S. Choi, H. H. Kim, *Eur. Urol.* **2003**, *44*, 475.
- [73] R. Kumar, M. Mukherjee, M. Bhandari, A. Kumar, H. Sidhu, R. D. Mittal, *Eur. Urol.* **2002**, *41*, 318.
- [74] K. Cromack, P. Sollins, R. L. Todd, R. Fogel, A. W. Todd, W. M. Fender, M. E. Crosley, D. A. Crosley, *Ecol. Bull. Stockholm* **1977**, *25*, 246.
- [75] G. M. Gadd, *Adv. Microb. Physiol.* **1999**, *41*, 47.
- [76] O. Braissant, E. P. Verrecchia, M. Arago, *Naturwissenschaften* **2002**, *89*, 366.
- [77] G. Cailleau, O. Braissant, E. P. Verrecchia, *Naturwissenschaften* **2004**, *91*, 191.
- [78] H. A. Lowenstam, D. McConnell, **1968**, *162*, 1496.
- [79] R. Cattaneo-Vietti, S. Angellini, L. Gaggero, G. Lucchetti, *J. Moll. Stud.* **1995**, *61*, 331.
- [80] S. Mann, *Nature* **1988**, *132*, 119.
- [81] H. D. Jiang, X. Y. Liu, G. Zhang, Y. Li, *J. Biol. Chem.* **2005**, *280*, 42061.
- [82] H. Cölfen, S. Mann, *Angew. Chem., Int. Ed.* **2003**, *42*, 2350.
- [83] J. Rieger, E. Hädicke, I. U. Rau, D. Boeckh, *Tenside Surfactants Deterg.* **1997**, *34*, 430.
- [84] O. Söhnle, J. W. Mullin, *J. Cryst. Growth* **1982**, *60*, 239.
- [85] W. Ostwald, *Z. Phys. Chem.* **1879**, *22*, 289.
- [86] C. A. Orme, J. L. Giocondi, in *Model Systems for Formation and Dissolution of Calcium Phosphate Minerals. In: Handbook of Biomineralization: Biomimetic and Bioinspired Chemistry* (Eds.: E. Baeuerlein, P. Behrens), Wiley-VCH, Weinheim, **2007**.
- [87] S. Takagi, H. Liao, L. C. Chow, *Caries Res.* **2000**, *34*, 281.

- [88] F. Grases, M. Ramis, A. Costa-Bauza, *Urol. Res.* **2000**, *28*, 136.
- [89] Y. Kakizawa, K. Miyata, S. Furukawa, K. Kataoka, *Adv. Mater.* **2004**, *16*, 699.
- [90] Y. Kakizawa, K. Kataoka, *Langmuir* **2002**, *18*, 4539.
- [91] M.-Y. Ma, Y.-J. Zhu, L. Li, S.-W. Cao, *J. Mater. Chem.* **2008**, *18*, 2722.
- [92] Z. Zhong, Y. Yin, B. Gates, Y. Xia, *Adv. Mater.* **2000**, *12*, 206.
- [93] S. W. Kim, M. Kim, W. Y. Lee, T. Hyeon, *J. Am. Chem. Soc.* **2002**, *124*, 7642.
- [94] W. Tjandra, P. Ravi, J. Yao, K. C. Tam, *Nanotechnology* **2006**, *17*, 5988.
- [95] D. G. Shchukin, G. B. Sukhorukov, H. Möhwald, *Angew. Chem. Int. Ed.* **2003**, *115*, 4609.
- [96] F. Caruso, *Chem. Eur. J.* **2000**, *6*, 413.
- [97] F. Caruso, *Adv. Mater.* **2001**, *13*, 11.
- [98] F. Caruso, R. A. Caruso, H. Möhwald, *Science* **1998**, *282*, 1111.
- [99] F. Caruso, R. A. Caruso, H. Möhwald, *Chem. Mater.* **1999**, *11*, 3309.
- [100] Q. Wang, W. Huang, D. Wang, *J. Wuhan University of Technology-Mater. Sci. Ed.* **2007**, *22*, 174.
- [101] Q. Wang, W. Huang, D. Wang, B. W. Darvell, D. E. Day, M. N. Rahaman, *J. Mater. Sci: Mater. Med.* **2006**, *17*, 641.
- [102] J. Gao, B. Zhang, X. Zhang, B. Xu, *Angew. Chem. Int. Ed.* **2006**, *45*, 1220.
- [103] H. P. Liang, H. M. Zhang, J. S. Hu, Y. G. Guo, L. J. Wan, C. L. Bai, *Angew. Chem. Int. Ed.* **2004**, *43*, 1540.
- [104] P. A. Wingert, H. Mizukami, A. E. Ostafin, *Nanotechnology* **2007**, *18*, 295707.
- [105] D. Walsh, L. Arcelli, V. Swinerd, J. Fletcher, S. Mann, *Chem. Mater.* **2007**, *19*, 503.
- [106] H. T. Schmidt, B. L. Gray, P. A. Wingert, A. E. Ostafin, *Chem. Mater.* **2004** *16*, 4942.
- [107] C. E. Fowler, M. Li, S. Mann, H. C. Margolis, *J. Mater. Chem.* **2005**, *15*, 3317.
- [108] Q. Shen, H. Wei, L. Wang, Y. Zhou, Y. Zhao, Z. Zhang, D. Wang, G. Xu, D. Xu, *J. Phys. Chem. B* **2005**, *109*, 18342.
- [109] L. Qi, J. Li, J. Ma, *Adv. Mater.* **2002**, *14*, 300.
- [110] D. Walsh, B. Lebeau, S. Mann, *Adv. Mater.* **1999**, *11*, 324.
- [111] C. I. Zoldesi, A. Imhof, *Adv. Mater.* **2005**, *17*, 924.
- [112] H. T. Schmidt, A. E. Ostafin, *Adv. Mater.* **2002**, *14*, 532.
- [113] Y. Cai, H. Pan, X. Xu, Q. Hu, L. Li, R. Tang, *Chem. Mater.* **2007**, *19*, 3081.
- [114] Q. Peng, Y. Dong, Y. Li, *Angew. Chem. Int. Ed.* **2003**, *42*, 3027.
- [115] J. Yu, H. Guo, S. A. Davis, S. Mann, *Adv. Funct. Mater.* **2006**, *16*, 2035.
- [116] B. Liu, H. C. Zeng, *J. Am. Chem. Soc.* **2004**, *126*, 8124.
- [117] H. G. Yang, H. C. Zeng, *Angew. Chem. Int. Ed.* **2004**, *43*, 5930
- [118] W. Ostwald, *Z. Phys. Chem.* **1897**, *22*, 289.
- [119] W. Ostwald, *Z. phys. Chem.* **1900**, *34*, 495.
- [120] A. D. Smigelskas, E. O. Kirkendall, *Trans. AIME* **1947**, *171*, 130.
- [121] E. O. Kirkendall, L. Thomassen, C. Upthegrove, *Trans. AIME* **1939**, *133*, 186.
- [122] E. O. Kirkendall, *Trans. AIME* **1942**, *147*, 104.
- [123] C. P. Collier, T. Vossmeier, J. R. Heath, *Annu. Rev. Phys. Chem.* **1998**, *49*, 371.
- [124] C. Pacholski, A. Kornowski, H. Weller, *Angew. Chem. Int. Ed.* **2002**, *41*, 1188.
- [125] H. C. Zeng, *J. Mater. Chem.* **2006**, *16*, 649.

- [126] Y. Yin, R. M. Rioux, C. K. Erdonmez, S. Hughes, G. A. Somorjai, A. P. Alivisatos, *Science* **2004**, *304*, 711.
- [127] Y. Yin, C. Erdonmez, S. Aloni, A. P. Alivisatos, *J. Am. Chem. Soc.* **2006**, *128*, 12671.
- [128] Y. Yin, C. K. Erdonmez, A. Cobot, S. Hughes, A. P. Alivisatos, *Adv. Funct. Mater.* **2006**, *16*, 1389.
- [129] D. F. Evans, H. Wennerström, *The Colloidal Domain*, Wiley-VCH, New York, **1999**.
- [130] M. Subirade, A. Lebugle, *Ann. Chim. Fr.* **1991**, *16*, 41.
- [131] M. Subirade, A. Lebugle, *Ann. Chim. Fr.* **1993**, *18*, 183.
- [132] A. Lebugle, M. Subirade, V. Delpech, *Hydroxyapatite and Related Materials*, CRC, London, **1994**.
- [133] F. Hoppe-Seyler, *Z. Physiol. Chem.* **1877-1878**, *1*, 121.
- [134] J. L. Soret, *Compt. Rend.* **1883**, *97*, 1267.
- [135] C. J. Weiss, *J. Mol. Spectrosc.* **1972**, *44*, 37.
- [136] E. D. Sternberg, D. Dolphin, C. Brückner, *Tetrahedron* **1998**, *54*, 4151.
- [137] K. M. Smith, D. A. Goff, R. J. Abraham, *J. Org. Magn. Reson.* **1984**, *22*, 779.
- [138] G. W. Kenner, S. W. McCombie, K. M. Smith, *J. Chem. Soc. Perkin Trans 1* **1973**, *21*, 2517.
- [139] M. O. Senge, K. M. Smith, *Photochem. Photobiol.* **1991**, *54*, 841.
- [140] K. M. Smith, J. F. Unsworth, *Tetrahedron* **1975**, *31*, 367.
- [141] R. J. Abraham, C. J. Medforth, K. M. Smith, D. A. Goff, D. J. Simpson, *J. Am. Chem. Soc.* **1987**, *109*, 4786.
- [142] R. J. Abraham, A. E. Rowan, K. E. Mansfield, K. M. Smith, *J. Chem. Soc. Perkin Trans. 2* **1991**, *4*, 515.
- [143] R. J. Abraham, G. E. Hawkes, X. H. Baith, *Tetrahedron Lett.* **1974**, *16*, 1483
- [144] C. B. Storm, Y. Teklu, *J. Am. Chem. Soc.* **1972**, *94*, 1745.
- [145] C. B. Storm, Y. Teklu, E. A. Sokoloski, *Ann. N. Y. Acad. Sci.* **1973**, *206*, 631.
- [146] R. Bonnet, *Chem. Soc. Rev.* **1995**, 19.
- [147] D. J. Granville, B. M. McManuss, D. W. C. Hunt, *Histol. Histopathol.* **2001**, *16*, 309.
- [148] E. D. Sternberg, D. Dolphin, C. Brückner, *Tetrahedron* **1998**, *54*, 4151.
- [149] F. Mitzel, S. FitzGerald, A. Beeby, R. Faust, *Chem. Eur. J.* **2003**, *9*, 1233.
- [150] K. Lang, J. Mosinger, D. M. Wagnerova, *Coord. Chem. Rev.* **2004**, *248*, 321.
- [151] R. F. Donnelly, P. A. McCarron, M. M. Tunney, *Microbiol. Res.* **2008**, *163*, 1.
- [152] V. Kral, J. Kralova, K. R., T. Briza, P. Martasek, *Physiol. Res.* **2006**, *55*, S3.
- [153] R. B. Boyle, D. Dolphin, *Photochem. Photobiol.* **1996**, *64* 469.
- [154] E. L. Clennan, *Tetrahedron* **2000**, *56*, 9151.
- [155] G. Jori, in: *Proceedings of the Ciba Foundation Symposium on Photosensitizing Compounds: Their Chemistry, Biology and Clinical Use* **1989**, *146*, Wiley, Chichester, 78.
- [156] K. Lang, J. Mosinger, D. M. Wagnerová, *Coord. Chem. Rev.* **2004**, *248*, 321.
- [157] F. Hoppe-Seyler, *Med. Chem. Untersuchungen.* **1871**, Eberhard-Karls-Universität, Berlin.
- [158] H. Scherer, *Ann. Chem. Pharm.* **1841**, *40*, 1.
- [159] F. Meyer-Betz, *Dtsch. Arch. Klin. Med. Chem. Untersuchungen.* **1913**, *112*, 476.

- [160] R. L. Lipson, E. J. Baldes, A. M. Olsen, *J. Natl. Cancer Inst.* **1961**, 26, 1.
- [161] R. Benesch, R. E. Benesch, C. I. Yu, *Proc. Natl. Acad. Sci.* **1968**, 59, 526.
- [162] A. Arnone, *Nature* **1972**, 237, 146.
- [163] M. F. Perutz, *Nature* **1970**, 228, 726.
- [164] A. Riggs, in *Biochemical Regulatory Mechanisms in Eukaryotic Cells* (Eds.: E. Kun, S. Grisolia), Wiley-Interscience, New York, **1972**.
- [165] F. Grases, A. Llobera, *Anal. Lett.* **1996**, 29, 1193.
- [166] F. Grases, A. Costa-Bauza, M. J. G., *Br. J. Urol.* **1994**, 74, 298.
- [167] F. Grases, L. Garcia-Ferragut, A. Costa-Bauza, M. J. G., *Nephron* **1996**, 73, 561.
- [168] F. Grases, L. Garcia-Ferragut, A. Costa-Bauza, *Nephron* **1998**, 78, 296.
- [169] G. E. Blank, J. Pletcher, M. Sax, *Acta. Cryst.* **1975**, B31, 2584.
- [170] L. R. Isbrandt, P. R. Oertel, *J. Am. Chem. Soc.* **1980**, 102, 3144.
- [171] L. G. Barrientos, P. P. N. Murthy, *Carbohydr. Res.* **1996**, 296, 39.
- [172] J. Emsley, S. Niazi, *Phosphorus and Sulfur* **1981**, 10, 401.
- [173] C. Brigando, J. C. Mossoyan, F. Favier, D. Benlian, *J. Chem. Soc. Dalton Trans.* **1995**, 575.
- [174] Z. He, C. W. Honeycutt, T. Zhang, P. J. Pellechia, W. A. Caliebe, *Soil Sci. Soc. Am. J.* **2007**, 71, 940.
- [175] A. Bebot-Brigaud, C. Dange, N. Fauconnier, C. Gerard, *J. Inorg. Biochem.* **1999**, 75, 71.
- [176] C. J. Martin, W. J. Evans, *J. Inorg. Biochem.* **1986**, 27, 17.
- [177] V. Raboy, *Phytochemistry* **2003**, 64, 1033.
- [178] I. Vucenik, A. M. Shamsuddin, *J. Nutr.* **2003**, 133, 3778S.
- [179] B. F. Harland, E. R. Morris, *Nutrition Res.* **1995**, 15, 733.
- [180] F. J. McClure, *J. Dent. Res.* **1963**, 42, 693.
- [181] F. J. McClure, *Science* **1964**, 144, 1337.
- [182] G. N. Jenkins, in *Advances in Oral Biology*, Vol. 2 (Ed.: P. H. Staples), Academic Press, New York, **1966**, pp. 67.
- [183] H. Nordbö, G. Rölla, *J. Dent. Res.* **1972**, 51, 800.
- [184] A. J. Cozzon, *Ann. Rev. Microbiol.* **1988**, 42, 97.
- [185] J. B. Stock, A. J. Ninfa, A. M. Stock, *Microbiol. Rev.* **1989**, 450.
- [186] C. Chang, R. C. Stewart, *Plant Physiol.* **1998**, 117, 723.
- [187] D. Barford, A. K. Das, M. P. Egloff, *Annu. Rev. Biophys. Biomol. Struct.* **1998**, 27, 133.
- [188] S. Mishra, A. W. Hamburger, *Cancer Res* **1993**, 53, 557.
- [189] B. M. Sefton, T. Hunter, K. Beemon, W. Eckhart, *Cell* **1980**, 20, 807.
- [190] S. Mishra, A. W. Hamburger, *Carcinogenesis* **1993**, 14, 269.
- [191] Z. Zhang, *J. Biol. Chem.* **1995**, 270, 16052.
- [192] S. Mishra, A. W. Hamburger, *Cancer Lett.* **1996**, 102, 65.
- [193] R. Goobes, G. Goobes, W. J. Shaw, G. P. Drobny, C. T. Campbell, P. S. Stayton, *Biochemistry* **2007**, 46, 4725.
- [194] E. C. Moreno, K. Varughese, D. I. Hay, *Calcif. Tissue Int.* **1979**, 28, 7.
- [195] J. M. Gibson, V. Raghunathan, J. M. Popham, P. S. Stayton, G. P. Drobny, *J. Am. Chem. Soc.* **2005**, 127, 9350.
- [196] D. I. Hay, E. C. Moreno, D. H. Schlesinger, *Inorg. Persp. Biol. Med.* **1979**, 2, 271.

- [197] K. Makrodimitris, D. L. Masica, E. T. Kim, J. J. Gray, *J. Am. Chem. Soc.* **2007**, *129*, 13713.
- [198] C. R. Eric, *Protein Pept. Lett.* **1999**, *6*, 295.
- [199] D. A. Pampena, K. A. Robertosn, O. Litvinova, G. Lajoie, H. A. Goldberg, G. K. Hunter, *Biochem. J.* **2004**, *378*, 1083.
- [200] E. Salih, S. Ashkar, H. Y. Zhou, L. Gerstenfeld, M. J. Glimcher, *Connect. Tissue Res.* **1996**, *35*, 207.
- [201] M. Lasa, P. L. Chang, C. W. Prince, L. A. Pinna, *Biochem. Biophys. Res. Commun.* **1997**, *240*, 602.
- [202] S. Ashkar, D. B. Teplow, M. J. Glimeher, R. A. Saavedra, *Biochem. Biophys. Res. Commun.* **1993**, *191*, 126.
- [203] P. J. Neame, W. T. Butler, *Connect. Tissue Res.* **1996**, *35*, 145.
- [204] W. G. Stetler-Stevenson, A. Veis, *Biochemistry* **1983**, *22*, 4326.
- [205] G. He, A. Ramachandran, T. Dahl, S. George, D. Schultz, D. Cookson, A. Veis, A. George, *J. Biol. Chem.* **2005**, *280*, 33109.
- [206] C. Tanford, *The Hydrophobic Effect: Formation of Micelles and Biological Membranes*, Wiley-Interscience, New York, **1973**.
- [207] E. A. G. Aniansson, S. N. Wall, M. Almgren, H. Hoffmann, I. Kielmann, W. Ulbricht, R. Zana, J. Lang, C. Tondre, *J. Phys. Chem.* **1976**, *80*, 905.
- [208] E. Y. Sheu, S. H. Chen, *J. Phys. Chem.* **1988**, *92*, 4466.
- [209] N. M. van Os, J. R. Haak, L. A. M. Rupert, *Physico-Chemical Properties of Selected Anionic, Cationic and Non-ionic Surfactants*, Elsevier, Amsterdam, **1993**.
- [210] E. Gorter, F. J. Grendel, *J. Exp. Med.* **1925**, *41*, 439.
- [211] A. D. Bangham, R. W. Horne, *J. Mol. Biol.* **1964**, *8*, 660.
- [212] D. D. Lasic, *Liposomes: from Physics to Applications*, Elsevier, Amsterdam, **1993**.
- [213] T. Tahara, I. Satake, R. Matuura, *Bull. Chem. Soc. Jpn.* **1969**, *42*, 1201.
- [214] P. Walde, M. Wessicken, U. Rädler, N. Berclaz, K. Conde-Frieboes, P. L. Luisi, *J. Phys. Chem. B* **1997**, *101*, 7390.
- [215] J. Arakawa, B. A. Pethica, *J. Colloid Interface Sci.* **1980**, *75*, 441.
- [216] L. D. Schuler, P. Walde, P. L. Luisi, W. F. van Gunsteren, *Eur. Biophys. J.* **2001**, *30*, 330.
- [217] Y. Han, S. Li, X. Wang, Y. Wang, *Nanoscience* **2006**, *11*, 102.
- [218] T. Kawakami, S. Igarashi, *Analyst* **1995**, *120*, 539.
- [219] J. W. Perich, R. B. Johns, *Synthesis* **1988**, 142.
- [220] L. J. McBride, M. J. Caruthers, *Tetrahedron Lett.* **1983**, *24*, 245.
- [221] T. Welzel, I. Radtke, W. Meyer-Zaika, R. Heumann, M. Epple, *J. Mater. Chem.* **2004**, *14*, 2213.
- [222] T. Kawakami, S. Igarashi, *Analytical Lett.* **1994**, *27*, 2083.
- [223] Y. N. Konan, J. Chevallier, R. Gurny, E. Allemann, *Photochem. Photobiol.* **2003**, *77*, 638.
- [224] B. Pegaz, E. Debefve, J. P. Ballini, Y. N. Konan-Kouakou, H. van den Bergh, *J. Photochem. Photobiol. B-Biology* **2006**, *85*, 216.
- [225] S. Sortino, A. Mazzaglia, L. M. Scolaro, F. M. Merlo, V. Valveri, M. T. Sciortino, *Biomaterials* **2006**, *27*, 4256.

- [226] R. Greiner, U. Konietzny, K. D. Jany, *J. Ernährungsmed.* **2006**, 8, 18.
- [227] A. Wise, *Bull. Environm. Contam. Toxicol.* **1981**, 27, 630.
- [228] A. Wise, *Bull. Environm. Contam. Toxicol.* **1982**, 29, 550.
- [229] H. Higashi, S. Natsugoe, Y. Uenosono, K. Ehi, T. Arigami, Y. Nakabeppu, M. Nakajo, T. Aikou, *Journal of Surgical Research* **2004**, 121, 1.
- [230] J. Campbell, J. C. Bellen, R. J. Baker, D. J. Cook, *J. Nucl. Med.* **1981**, 22, Pages: 157.
- [231] S. K. Imam, M. Killingsworth, *World J. Nucl. Med.* **2005**, 4, 179.
- [232] M. A. A. Al-Janabi, *J. Labelled Compounds and Radiopharmaceuticals* **1989**, 27, 1137.
- [233] T. Welzel, W. Meyer-Zaika, M. Epple, *Chem. Commun.* **2004**, 1204.
- [234] Z. He, C. W. Honeycutt, T. Zhang, P. M. Bertsch, *J. Environ. Qual.* **2006**, 35, 1319.
- [235] B. G. Santoni, G. E. Pluhar, T. Motta, D. L. Wheeler, *Bio-medical Materials and engineering* **2007**, 17, 277.
- [236] T. Sugama, B. Lipford, *J. Mater. Sci.* **1997**, 32, 3523.
- [237] R. X. Sun, Y. P. Lu, M. S. Li, *Surface Engineering* **2003**, 19, 392.
- [238] Y. Musha, M. Abe, T. Umeda, K. Itatani, *Phosphorus Research Bulletin* **2006**, 20, 149.
- [239] H. T. Schmidt, M. Kroczyński, J. Maddox, Y. Chen, R. Josephs, A. E. Ostafin, *J. Microencapsulation* **2006**, 23, 769.
- [240] A. Bigi, E. Boanini, D. Walsh, S. Mann, *Angew. Chem.* **2002**, 114, 2267.
- [241] A. Bigi, B. Bracci, S. Panzavolta, M. Iliescu, M. Plouet-Richard, J. Werckmann, D. Cam, *Cryst. Growth & Design* **2004**, 4, 141.
- [242] P. F. Alewood, R. B. Johns, R. M. Valerio, *Synthesis* **1983**, 1, 30.
- [243] Y. Okamoto, *Bull. Chem. Soc. Jpn.* **1985**, 58, 3393.

7. Appendix

7.1. List of Abbreviations

CDCl ₃	Deuterated chloroform
D ₂ O	Deuterated water
DDP	Dodecyl phosphate
DDOPhP	<i>p</i> -dodecyloxyphenyl phosphate
DDOBPhP	<i>p</i> -dodecyloxybiphenyl- <i>p</i> '-phosphate
DLS	Dynamic light scattering
DMSO	Dimethylsulphoxide
DNA	Deoxyribonucleic acid
EDX	Energy dispersive X-ray analysis
ESI-MS	Electron spray ionisation mass spectrometer
IR	Infrared
MCPBA	<i>meta</i> -chloro perbenzoic acid
MTT	Methyl thiazole tetrazolium bromide
NIH 3T3	National Institutes of Health - 3-day transfer, inoculum 3 · 10 ⁵ cells
NMR	Nuclear magnetic resonance
ODP	Octadecyl phosphate
PDI	Polydispersity index
PDT	Photodynamic therapy
siRNA	small interfering Ribonucleic acid
SEM	Scanning electron microscopy
TDP	Tetradecyl phosphate
<i>p</i> -THPP	5,10,15,20-tetrakis(4-hydroxyphenyl)porphine
<i>p</i> -TPPP	5,10,15,20-tetrakis(4-phosphonooxyphenyl)porphine
TyrP	<i>O</i> -phospho-L-tyrosine
UV-vis	Ultraviolet-Visible
XRD	X-ray (powder) diffractometry

7.2. Publications

K. Ganesan, M. Epple, "Calcium phosphate nanoparticles: Colloidally stabilized and made fluorescing by a phosphate-functionalized porphyrin", **Journal of Materials Chemistry (Accepted)**

K. Ganesan, M. Epple, " Colloidal calcium phytate prepared from calcium phosphate nanoparticles", **New Journal of Chemistry (Accepted)**

7.3. Presentations and posters

13. Heiligenstädter Kolloquium "Technische Systeme für Biotechnologie und Umwelt", Heiligenstadt, 25.-27.09.2006, K. Ganesan, M. Epple, "Die Rolle von Alkylphosphaten bei der Funktionalisierung von Calciumphosphat-Nanopartikeln" (**poster**)

International Symposium "Bio-inspired synthesis and materials – from organic templates to functional nanoscale structures", Ringberg, 11.-14.10.2006, K. Ganesan, M. Epple, "The role of alkyl phosphates in functionalizing calcium phosphate nanoparticles" (**poster**)

10th International Conference on Advanced Materials, IUMRS-ICAM 2007, Bangalore (Indien), 08.-13.10.2007, K. Ganesan, M. Epple, "Functionalization of calcium phosphate nanoparticles with biologically important alkyl phosphates" (**poster**)

Current Topics in Medical Technology, Münster, 30.11.2007, K. Ganesan, M. Epple, "Functionalization of calcium phosphate nanoparticles with porphyrin" (**poster**)

World Biomaterials Congress, Amsterdam, 28.05.-01.06.2008, M. Jayabalan, K. Ganesan, M. Epple, "Studies on biomechanical and interfacial stability of poly(propylene fumarate) micro-hydroxyapatite composite" (**poster**)

7.4. Curriculum vitae

Personal Details

Name : Kathirvel Ganesan
Date of Birth : 29.07.1980
Place of Birth : Tiruchirappalli, Tamil Nadu, India
Nationality : Indian
Marital Status : Single

Education

July 1997- April 2000 : Study of Bachelor of Science in Chemistry at Bishop Heber College (first class with distinction; Tenth rank in University; Third rank in Bishop Heber College).

July 2000- April 2002 : Study of Master of Science in Chemistry (first class). Work on Master Thesis under the guidance of Professor Dr. K. Panchanatheeswaran at the Bharathidasan University. Project title: “*Phosphine and Phosphite Interactions with $(C_6H_5CH_2)_2SnCl_2$ and $(C_6H_5CH_2)_3SnCl$: Synthesis, Spectral and Structural Studies*”.

01.09.2002 – 30.04.2003 : Work as a Project Assistant under the guidance of Assistant Professor Dr. Balaji R. Jagirdar, Department of Inorganic and Physical Chemistry, Indian Institute of Science, Bangalore, India.

02.06.2003 - 31.12.2004 : Work as a Scientific Assistant under the guidance of Professor Dr. Matthias Driess, Department of Inorganic Chemistry, Ruhr University of Bochum, Bochum, Germany.

01.01.2005 - 30.05.2008 : Work as a Ph.D. Student under the guidance of Professor Dr. Matthias Epple, Institute for Inorganic Chemistry, University of Duisburg-Essen, Essen, Germany.

7.5. Acknowledgement

It is my pleasure to express my heart-felt gratitude and indebtedness to my guide Prof. Dr. Matthias Epple, Institute of Inorganic Chemistry, University of Duisburg-Essen, for his invaluable guidance. His constant encouragement, timely help and enlightening discussions provided me the zeal for the successful completion of the Ph.D work.

I would like to thank Dr. Wolfgang Mayer-Zaika, Mrs. Ursula Giebel, Mrs. Barbara Nota, Mrs. Kerstin Brauner, Mrs. Veronika Hiltenkamp, Mrs. Sabine Bollmann, and Mrs. Carola Fischer for spending their invaluable timing in countless occasions for their technical help, encouragement and moral support.

I owe a lot to my colleagues for their discussions and cooperation to solve intellectual problems and moral support. I acknowledge the help and cooperation extended to me by each member of the Faculty of the Chemistry, University of Duisburg-Essen, Essen.

I would like to thank Prof. Dr. Rolf Heumann, Mr. Sebastian Neumann and Ms. Anna Kovtun for their assistance with cell experiments.

It is my duty to acknowledge the services and help rendered by my teachers, who really shaped me to this extent.

No word will be adequate to express my love to my parents, brother and my friends and for their wishes were the driving force for the successful completion of my Ph.D.

7.6. Erklärung

Hiermit versichere ich, dass ich die vorliegende Arbeit mit dem Titel

„Functionalization of Calcium Phosphate Nanoparticles with Organic Phosphate“

selbst verfasst und keine außer den angegebenen Hilfsmitteln und Quellen benutzt habe und dass die Arbeit in dieser oder ähnlicher Form noch bei keiner anderen Universität eingereicht wurde.

Essen, im April 2008

Kathirvel Ganesan.